Modulated electron beam produced by a thermionic cathode electron gun for particle accelerator applications

Georgia Adam (B.Sc., M.Sc)

Atoms, Beams and Plasmas Group

Department of Physics and SUPA

University of Strathclyde

A thesis presented in the fulfilment of the requirements for the degree of

Doctor of Philosophy

December 2021

Declaration

This thesis is the result of the author's original research. It has been composed by the author and has not been previously submitted for examination which has led to the award of a degree. The copyright of this thesis belongs to the author under the terms of the United Kingdom Copyright Acts as qualified by University of Strathclyde Regulation 3.50. Due acknowledgement must always be made of the use of any material contained in, or derived from, this thesis.

Signed: Georgia Adam

Date: 21/02/2022

Contents

Declaration ii

Abstract vii

Acknowledgments ix

Publications x

List of Figures xi

1 Introduction 1

1.1 LINACs and their applications 3

1.2 Medical LINACs and FELs 5

1.2.1 The system of medical LINAC 7

1.2.2 FELs 15

1.3 The injector system of LINAC 21

1.3.1 Different types of the electron gun 21

1.4 Objectives of the PhD study 25

2 Theory of Electron Guns 30

2.1 Production of electrons and emission mechanisms 30

2.1.1 Fermi-Dirac distribution law 30

2.1.2 Work function and conditions of electron emission 33

2.1.3 Thermionic emission 33

2.1.4 Space Charge Limited Emission and Child Langmuir law 37

2.1.5 Photoemission 38

2.1.6 Photocathodes 40

2.1.7 Schottky effect and field emission 40

2.1.8 Field emission cathodes 44

2.1.9 Domains of emission 45

2.2 Cathode Designs and Applications 50

2.2.1 Pierce Type Gun – Design and Principle 50

2.2.2 Parallel Plane Geometry 51

2.2.3 Converging Beams 53

2.2.4 Conclusion Pierce gun 55

2.3 Electron beam physics 58

2.3.1 Phase and trace space description of an electron beam 58

2.3.2 Emittance of an electron beam and beam brightness 60

Summary 62

3 A Theoretical Model of a Modulated Electron Gun 63

3.1 Initial electron beam parameters for the LINAC 64

3.2 Modulation of an electron gun 65

3.3 Configuration of an electron gun with RF gating 66

3.4 Capacitively-loaded coaxial cavity for the RF electron gun 67

3.5 Breakdown Physics 70

3.5.1 Modified Poynting Vector 72

3.6 Operation of the RF electron gun 78

3.7 Validity of the Child Langmuir law for high RF voltage 81

3.8 Control voltage and emitted current 82

3.9 The theoretical model of bunch length and bunch charge 85

Summary 88

4 Design and Simulation of an Electron Gun in 2D 89

4.1 Pierce electron gun 90
4.2 Modelling of a Pierce electron gun 93
4.2.1 Vaughan synthesis, input and output parameters 94
4.2.2 Emittance 97
4.3 Modelling using TRAK 100
4.3.1 Finite Element Method 100
4.3.2 Simulation using TRAK (E-static electron gun) 103
4.3.3 Optimisation of the electron gun from the initial geometry 105
Summary 113

5 Particle-in-Cell Simulations of the RF Gun 114

5.1 Particle-in-Cell (PIC) Method 114
5.2 Finite-Difference Time-Domain (FDTD) 117
5.2.1 Maxwell's equations 117
5.2.2 Boundary conditions ..... **Error! Bookmark not defined.**
5.2.3 Finite-Difference Time-Domain (FDTD) Technique 118
5.3 Modelling using MAGIC (RF gated gun) 121
5.4 Effect of different combinations of RF and bias voltage on the emitted current 125
5.5 Discrepancies between the theoretical model and simulation 126
5.5.1 Reasons for bunch widening 128
5.6 Transverse emittance of the RF gun 129
5.7 Relationship between bunch length and bunch charge at 1.5 GHz and 3.0 GHz RF frequency 131
Summary 133

6 3D Simulation of RF gated Gun using CST PS Studio 134

6.1 Beam dynamics comparison between 2D and 3D simulations 136
6.1.1 Static electron gun 136
6.2 CST modelling of the RF electron gun 140
6.3 RF electron gun 143
6.4 Effect of different designs of grid on the performance of the RF gun 151

155

6.5 Modulation of the RF-gated grid at higher harmonics of the fundamental frequency. 156
Summary 161

7 Conclusions 162

7.1 Summary 162
7.2 Comparison of 2D MAGIC and 3D PIC simulations of the RF gated e-gun 165
7.3 Conclusion 166
7.4 Future work 167

References 170

Abstract

Electron injectors used in radiation sources such as Free-electron lasers (FELs) and medical linear accelerators (LINACs) can generate high peak current and low emittance electron beams. There are different types of electron injectors depending on their cathode. These are thermionic cathodes, photocathodes, and field emission cathodes. Each one of them has its own advantages and disadvantages. In this thesis, considering the advantages of a long lifetime, large current density and being cost-effective, a thermionic cathode gridded electron gun for a particle accelerator was designed and modelled. Both theoretical work and numerical simulations were carried out to explore the relationship between important parameters like the bunch charge and the bunch length of the modulated beam. Two 2D simulation packages, the DC electron trajectory solver TRAK and Particle-In-Cell code MAGIC were utilised initially to optimise the Pierce-type electron gun and to simulate the RF field applied to the grid. Similar to existing guns the electron energy, pulse duration and charge of the electron beam bunch were predicted but the significant deviation from existing guns was the pulse length as the function of the bunch charge. The beam dynamics simulations showed that a minimum pulse length of 106 ps could be achieved with a bunch charge of 33 pC when the driving RF frequency was 1.5 GHz. Simulations at a higher RF frequency did not significantly reduce the micro-pulse length and the normalised emittance was measured to be 5.6 mm·mrad obtained from the particle-in-cell simulations. The results obtained with 2D simulation packages were compared with 3D simulations using CST Particle Studio with similar values for the pulse length at a value of 102 ps for 35 pC bunch charge observed. Different designs of grids, the

spider web grid and the pepper pot grid were simulated and their performance was examined and compared. The comparison resulted in similar values for the peak current and the bunch charge. Furthermore, other techniques for reduction of the bunch length like higher harmonics of the fundamental frequency, specifically the idealised case of a square wave, using CST Particle Studio are presented.

Overall, the notable advance in science lies in obtaining the bunch length as the function of the bunch charge which enabled the calculation of the emittance as a function of time by post-processing the output of the numerical simulations. This is vital information to be passed to the designers of the S-band (3GHz) LINAC as it enables the performance of the LINAC in terms of capture of electrons to be predicted.

Acknowledgments

It is my pleasure to acknowledge the contributions of those who participated in this project from the start to the end. First and foremost, I wish to thank my two supervisors Prof. Adrian Cross and Dr Liang Zhang for introducing me to the magnificent field of RF and accelerator physics and for all the guidance and instruction. Especially Liang Zhang as without his expertise, his modelling and recommendations this project would have been impossible to be completed. Really can't thank him enough. Scientific advice from Boris Militsyn of ASTeC, STFC, Daresbury UK on medical linacs is greatly appreciated.

Furthermore, I would like to thank the STFC for providing the industrial case (ASHE) studentship and to thank the STFC project "A modular, integrated electron gun and RF cavity for radiotherapy treatment systems in developing countries" for supporting this work. The support and interaction with the industrial partner TMD Technologies

Ltd is gratefully acknowledged as it allowed to take a different look at the project from an industry perspective.

On a more personal note, I wish to thank my parents for their support and understanding for all of these years of education letting me follow my dreams and most importantly always being proud of my achievements. Although in Greece, they always made me feel that they were near me.

Finally, a massive thank you to my partner Dr David Speirs and his family for always being there for me and making me feel like I am home. I don't have the words to express my gratitude for the amount of support and encouragement I have received from him and for putting up ‘sometimes’ with my impatience! Always grateful!

Publications

[1] Zhang L, Adam G, Militsyn B, He W, Cross AW. Electron Injector Based on Thermionic RF-Modulated Electron Gun for Particle Accelerator Applications. IEEE Transactions on Electron Devices. 2020;67(1):347-53.

[2] G.Adam, L. Zhang, A. W. Cross and B.Militsyn, “Beam dynamic analysis of RF modulated electron beam produced by gridded thermionic guns”, Proceedings of the 12th International Particle Accelerator Conference (IPAC), August 2021.

List of Figures

Figure 1-1. Schematic of a modern S band medical LINAC [27]..... 7
Figure 1-2. Cross-sectional views of the two types of electron guns used in medical LINACS diode (left), triode (right) [28, 29]. 8
Figure 1-3. Cross-section of a magnetron. 9
Figure 1-4. Schematic of a two-cavity klystron [33]. 10
Figure 1-5. A schematic of a travelling wave structure (left) and a standing wave structure (right) [34]. 11
Figure 1-6. The three systems of electron beam bending [34]. 12
Figure 1-7. Global Radiotherapy market revenue for 2014-2022 [121]. 14
Figure 1-8. A low gain FEL with G-the electron gun, A-accelerator, U-undulator and M-mirror [51]. 16
Figure 1-9. A high gain FEL with superconducting electron accelerator modules. 1-electron gun with laser-driven photocathode, 2-Superconducting modules of electron accelerator, 3-electron beam compressor (chicane), 4-electron beam collimator, 5-undulator sections, 6-bending magnet, 7-electron beam absorber, X-ray radiation output [51]. 17
Figure 1-10. List of the main parameters of short-wavelength FEL facilities in order of their coming online, and includes two facilities which are under construction and will be online in the next five years. The colour coding relates to the RF technology –

superconducting (SC) or normal conducting (NC). The first facility to offer short-wavelength FEL light to users was the pioneering FLASH in 2005, recently upgraded to FLASH-II by including gap tunable undulators. FLASH was originally constructed as an SC linac test facility and the technological advances it produced were critical to the design and success of the European XFEL. The first hard X-ray facility was LCLS-I, which started operations in 2009, and has since been joined by facilities in Japan, the EU, Switzerland and South Korea. 20
Figure 1-11. Thermionic electron gun showing the cathode and the heater mechanism for the electron extraction (photograph courtesy of TMD Ltd). 22
Figure 1-12. A cesiated tungsten photocathode [123]..... 23
Figure 1-13. A Schottky emitter, a type of a field emission electron gun at different length scales [124]..... 24
Figure 1-14. Thesis outline where each stage describes the process followed for designing the electron gun. 28
Figure 2-1 (a) Density of states, (b) Fermi-Dirac probability factor, and (c) Electron energy distribution function versus electron energy [132]. 32
Figure 2-2. Fermi-Dirac distribution at different temperatures $T_3 > T_2 > T_1$ [126]. 32
Figure 2-3. Condition for thermionic emission to take place, $E \geq Ef + Ew$..... 34
Figure 2-4. Three-step model for photoemission. Initially photons are absorbed and photoelectrons are excited moving towards the surface. These photoelectrons experience inelastic scattering which leads to the creation of secondary electrons. Finally, these photoelectrons escape to vacuum. 39
Figure 2-5. Effect of the external field on the potential energy results in the increase of the emission current demonstrating Schottky effect. Near the cathode surface the electric field, E_{field} reduces the barrier electrons need to overcome in order to be emitted so more electrons are emitted. 41
Figure 2-6. Diagram of work function potential at surface of material under application of a very strong electric field (~10^9 Vm-1). 42
Figure 2-7. Distortion of the potential barrier shown for both the Schottky effect and Field Emission. The energy profile for the Field Emission is like that for the Schottky effect. However the width of the potential barrier is narrower which increases the

probability of an electron tunnelling through which leads to an increase in the emission current density [128]. 44
Figure 2-8. Mechanisms dominating current flow through a thermionic diode [132]. 46
Figure 2-9. Schematic of a typical Pierce type electron gun [133]. 50
Figure 2-10. Schematic of equipotential profiles in a diode without electrons (dashed lines) and with electrons (solid lines) [133]. 51
Figure 2-11. Geometry of planar Pierce gun showing calculated equipotential lines within in both the beam and vacuum regions [133]. 52
Figure 2-12. Schematic of a electron emission and beam focussing in a high perveance electron gun [133]. 55
Figure 2-13. Example of a pepperpot type control grid widely used for a Pierce electron gun. (photograph courtesy of TMD Technologies Ltd). 57
Figure 2-14. Graphic representation of phase space. The particles in the beam can be viewed as an ensemble in phase-space (distribution) evolving in time including the constraint of Liouville's theorem. The lattice ellipse can be filled with particles evolving in time [130]. 59
Figure 3-1. Two different configurations of the RF gun, (a) without DC pre-acceleration, (b) with DC pre-acceleration. 67
Figure 3-2. The schematic of the coaxial input cavity. 67
Figure 3-3. Variation of resonant frequency with the cavity length. 70
Figure 3-4. A schematic diagram of the power flow near a protrusion on the surface of an accelerating structure which would lead structure to breakdown. 73
Figure 3-5. The Kilpatrick formula for conservatively calculating the breakdown potential for a given operating frequency. 75
Figure 3-6. Electric field between the cathode and the grid for 0.16mm cathode-grid spacing..... 76
Figure 3-7. CST model of the electron gun geometry (top), collected current at the anode for different values of cathode-grid spacing (bottom). 77
Figure 3-8. Time dependence of the grid voltage and the electron current. 82
Figure 3-9. Relationship between bunch charge and bunch length for 1.5GHz (top) and 3GHz (bottom) operating frequency. 87

Figure 4-1. Overview of a Pierce gun including the three regions of interest [104]. 94
Figure 4-2. Schematic representation including the input and output parameters of a Pierce electron gun [105]. 95
Figure 4-3. Effect of the emitter radius on the emittance (top) and the effect of the cathode voltage on the emittance (bottom). 99
Figure 4-4. Block diagram of FEM computations. 101
Figure 4-5. Definition of terms in a triangular formed mesh. 102
Figure 4-6. Regions of the electron gun using the feature Mesh (top) and Estat for the electric field distribution (bottom). 104
Figure 4-7. Schematics representation of the NJK2221A gridded thermionic cathode, dimensions are expressed in mm..... 106
Figure 4-8. Resultant values for the total emitted current and beam waist radius for different cathode radiuses. 107
Figure 4-9. Resultant values for the total emitted current and beam waist radius for different gap distances between cathode/anode. 108
Figure 4-10. Resultant values for the total emitted current and beam waist radius for different focusing electrode angles. 108
Figure 4-11. The simulated electric field as a function of gap distance..... 109
Figure 4-12. Values of current for different cathode temperatures. 110
Figure 4-13. Optimised geometry to achieve the desired values for the beam parameters. 111
Figure 4-14. TRAK simulation used for calculating for the emittance at the exit of the anode. 112
Figure 5-1. Particle In Cell simulation cycle..... 115
Figure 5-2. The Nearest Grid Point (NGP) scheme. 117
Figure 5-3. Standard Cartesian Yee cell used for FDTD technique(top) and the leapfrog method where the position and the velocity is calculated between two consecutive forward and backward time value (bottom). 119
Figure 5-4.Running time and collected current at the anode against the number of mesh cells showing convergence at 120,000 mesh cells..... 123
Figure 5-5. Geometry of the RF electron gun using MAGIC. 124

Figure 5-6. Different time frames showing the evolution of the beam bunching at the different regions. 125
Figure 5-7. Relationship between the grid voltage and the emitted current. 126
Figure 5-8. The emitted current from the cathode and the collected current at the entrance of the accelerator cavity. 127
Figure 5-9. The emittance of the electron at the exit of the anode 130
Figure 5-10. The relationship between the bunch length and bunch charge at different grid voltages with RF frequency of 1.5 GHz (top) and 3.0 GHz (bottom). 132
Figure 6-1. Gun iteration algorithm including space charge. 135
Figure 6-2. Schematic diagram of the 3D geometry of the static electron gun using Particle CST Studio. 136
Figure 6-3. Collected currents for different cathode voltages and comparison between the results obtained with TRAK 2D and CST 3D. 137
Figure 6-4. Collected currents for different gap distances between the cathode and the anode. 138
Figure 6-5. Electric field variation for different cathode-anode distances. 139
Figure 6-6. Collected currents for different cathode radiuses. 140
Figure 6-7. Illustration of the primary and dual grid cells used in the FIT [115]. .. 142
Figure 6-8. Allocation of voltages along edges and fluxes through surfaces in the FIT. 142
Figure 6-9. Electron gun with the coaxial cavity using 3D CST Particle Studio. ... 144
Figure 6-10. Emitted current from cathode and collected current at anode as a function of time for many pulses. 145
Figure 6-11. Emitted current from cathode and collected current at anode as a function of time for one pulse. 145
Figure 6-12. Collected currents for different V_{dc} voltages and V_{rf}=15V. 146
Figure 6-13. Collected current (A), bunch length and bunch charge for different values of bias voltage and V_{rf}=15V (top to bottom). 147
Figure 6-14. Collected current for different Vrf voltages and Vdc = 50V. 148
Figure 6-15. Collected current (A), bunch length and bunch charge for different values of Vrf and Vdc = 50V (top to bottom). 150

Figure 6-16. Three types of grid including a)transparent lossy material b)spider web grid and c) pepperpot grid (top to bottom). 152
Figure 6-17 Current pulse at the exit of the anode for the the three types of grids. 153
Figure 6-18. Collected current at the exit of the anode, bunch length and bunch charge for different values of V_{rf} and V_{dc}=50V. 154
Figure 6-19. Collected current at the exit of the anode, bunch length and bunch charge for different values of V_{dc} and V_{rf}=25V. 155
Figure 6-20. Addition of higher harmonics to form a square wave. 157
Figure 6-21. Excitation signal of 1.5GHz and square excitation signal. 158
Figure 6-22. Collected currents for 1.5GHz sinusoidal excitation signal (red) and for a square excitation signal (green). 159
Figure 6-23. User input excitation signals for the different time duration. 160
Figure 6-24. Bunch length and bunch charge values for different signal widths.... 160

Chapter 1

1 Introduction

Radiofrequency (RF) electron guns are basic components of linear accelerators (LINACs) which have a variety of applications in scientific research and industry. The development of high-current, low emittance and short-duration beam pulses has been necessary for the operation of coherent radiation sources like Free Electron Lasers (FELs) and the acceleration of electron bunches onto metal targets for the generation of X-ray radiation for radiotherapy treatment of cancers.

There are different types of electron guns depending on their emission process from the cathode and their operation. These are thermionic cathodes, photocathodes and field emission cathodes. Thermionic cathodes are very robust due to their long lifetimes which can reach up to 100,000 hours, however the energy spread and the long

pulses at the exit of the LINAC are not ideal for certain applications. This problem is resolved by photocathodes which can achieve high current densities and very short pulses although photocathodes require a high power laser and ultra-high vacuum to operate. Lastly, field emission cathodes are able to generate very high current densities but are fragile and prone to damage due to vaporisation of the cathode tip.

Another differentiation between electron guns lies in their operation which categorises them into two types, the diode type and the triode type. In a normal diode type electron gun, high voltage is applied between the cathode and the anode to create a continuous wave (CW) electron beam or long pulse (>100ns) duration electron beams. This type of gun limits the repetition rate to kHz or MHz at most due to the time it takes to switch on and off the high voltage power supply to the cathode. Triode electron guns incorporate a grid or modulated anode which is placed in front of the cathode controlling the current by switching on and off the beam. In the triode type, the current is controlled with a much smaller voltage achieving a much higher repetition rate.

Designing an RF electron gun for a source like a medical LINAC or an FEL occurs through different stages. The first stage involves theoretical and simulation work where parameters like current density, beam size, emittance, bunch charge and bunch length are taken into account. Different simulation packages, both 2D and 3D are used to calculate and find the optimum/feasible parameters and the relationship between them while investigating fundamental concepts.

In this thesis, an electron gun was designed and studied through a theoretical model and Particle-In-Cell (PIC) simulations in both 2D and 3D. The electron gun was based on a gridded thermionic cathode with a Pierce type configuration geometry which was

initially optimised using the 2D TRAK solver. This optimised geometry was transferred in MAGIC, the PIC simulation code, and based on the specifications of the LINAC the minimum achievable pulse length was established. Furthermore, the relationship between the bunch charge and bunch length was explored and the reason for certain discrepancies between the theoretical model and the simulation work were justified. The 2D simulations were verified with 3D simulations using CST Particle Studio and two different types of grid, spider web and pepperpot design, were used to investigate the effect on the current, bunch length and bunch charge. Moreover, different techniques on potentially reducing the bunch length, like the injection of higher harmonics was investigated.

1.1 LINACs and their applications

A LINAC is used to accelerate particles at almost the speed of light by injecting these particles in oscillating fields. The size of a LINAC varies depending on the required final kinetic energy of the particles. For example, the size of a LINAC for the production of X-rays is about 0.5-1.5m long however when serving as an injector for a synchrotron is about 10m long and the size of it can extend to thousands of meters for nuclear particle investigation.

The major parts of a LINAC are the electron gun, the buncher and the LINAC itself [1]. The electron gun is the source of the electrons and the electrons are emitted from a cathode which has a negative electrical charge. In front of the cathode, depending on the type of the electron gun, a grid can be found. The purpose of the grid is to allow the beam to switch on and off at high repetition rates. After the electrons have made it through the grid they arrive at the anode which has a hole in it through which the

electrons propagate to the accelerating cavity often refered to as the buncher. The purpose of the buncher is to accelerate the electrons and form them into bunches by receiving microwave radiation from an RF power generation system. The LINAC is an extension of the buncher where the electrons are getting accelerating and formed into tighter bunches reaching very close to the speed of light by the time they exit the LINAC.

The application of LINACs can be divided into four different fields. These include medical, industrial, military and research applications [2-4]. Some of these applications are for cancer treatment like medical LINACs [5-7], radioisotope production for Positron Emission Tomography (PET) [8-10], X-ray radiography [11, 12], neutron activation analysis [13-16], Free Electron Lasers (FELs) [17-23] and other techniques [24]. Research and development of new linear accelerators is continuing work as the demand for more advanced LINACs is expected to increase in the next decade. In this thesis, the focus has been on medical LINACs and FELs.

1.2 Medical LINACs and FELs

Both medical LINACs and FELs use an electron injector for the production of the electrons, however the final energy at the exit of the LINAC is much higher in the FELs. Medical electron linear accelerators (LINACs) are commonly used to produce MeV electron beams for radiation therapy. For medical LINACs there are three major linear accelerator vendors. These are Elekta, Siemens, and Varian. Specifications of each are given in Table 1-1. On the other side, the energies produced in FELs are tens of GeVs. For energy comparison, examples of energies for the X-ray FELs around the world are given in Table 1-2.

Accelerator items	**Siemens (Artiste model)**	**Varian (Truebeam model)**	**Elekta (Synergy model)**
Pulse repetition freq.	200-400Hz	180-360Hz	200-400Hz
RF power source	Klystron	Klystron	Magnetron
Acc. waveguide type	Standing wave	Standing wave	Travelling wave
Max RF power level	5-10 MW	7-12 MW	2.5-5 MW
Magnet type	270 bending magnet	270 bending magnet	90 Slalom bending
Available energies	4-23 MeV	4-23 MeV	4-25MeV

Table 1-1. Characteristics of the components of different commercial LINACS [25].

	European X-ray FEL	**Light Coherent Light Source**	**Light Coherent Light Source II**	**Light Coherent Light Source II**	**SPRing-8 Compact FEL**	**Swiss FEL**	**Pohang Accelerator Laboratory X-ray FEL**
Location	Germany	USA	USA	USA	Japan	Switzerland	South Korea
Accelerator technology	Super-conducting	Normal	Normal	Super-conducting	Normal	Normal	Normal
Maximum electron energies	17.5GeV	14.3 GeV	15 GeV	5 GeV	8.5 GeV	5.8 GeV	10 GeV
Length of facility	3.4km	3km	3km	3km	0.75km	0.74km	1.1km
Peak brilliance	$5x10^{33}$	$2x10^{33}$	$2x10^{33}$	$1x10^{32}$	$1x10^{33}$	$1x10^{33}$	$1.3x10^{33}$

Table 1-2. Comparison of the different X-ray FELs [26].

1.2.1 The system of medical LINAC

A schematic of a medical LINAC is shown in Figure 1-1. This schematic provides a general layout of a medical LINAC's components. The main components of a medical LINAC are the Injection System, the RF Power Generation System, the Accelerating Waveguide and the Beam Transport System. All four components are explained in more detail in the following sections.

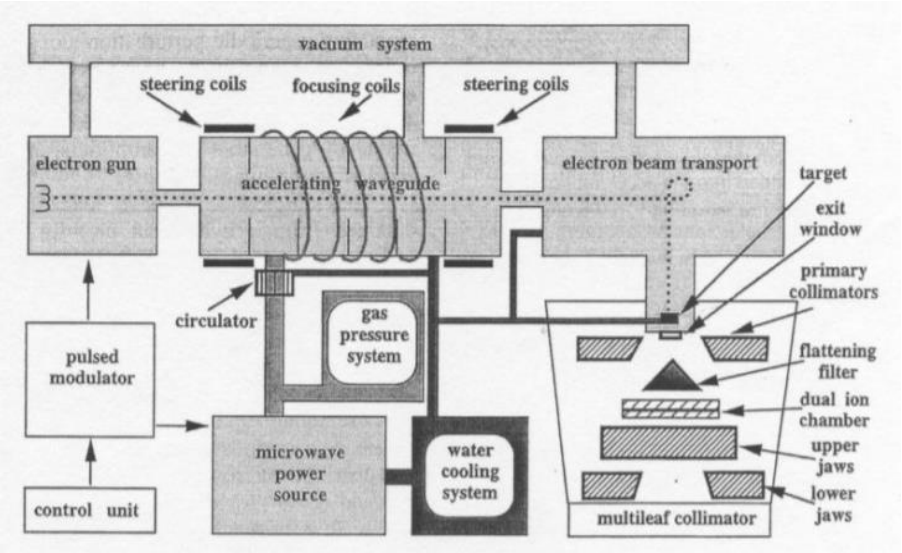

Figure 1-1. Schematic of a modern S band medical LINAC [27].

1.2.1.1 Injection System

The electron injection system for the LINAC is more commonly known as the electron gun. The electron gun is the provider of the electrons which form the beam. The electron gun contains a heated filament, a cathode and a cathode mount with heat shields, a heater, a grounded anode and a grid to control the current emitted from the cathode. The design of the two different types of electron guns is shown in Figure 1-2.

The process involves electrons being emitted from the cathode, formed into a beam by a focusing electrode and accelerated towards the anode through which they enter the accelerating waveguide. The electrostatic field needed to accelerate the electrons is supplied from the pulse modulator delivered to the cathode of the electron gun. The grid of the triode gun is normally held negative with respect to the cathode to cut off the current to the anode.

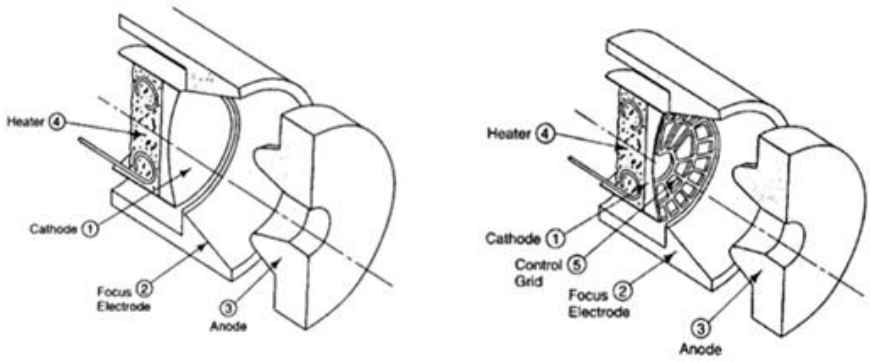

Figure 1-2. Cross-sectional views of the two types of electron guns used in medical LINACS diode (left), triode (right) [28, 29].

1.2.1.2 RF power generation system

The RF power generation system is responsible for producing microwave radiation for the acceleration of the electrons in the accelerating waveguide. This system consists of two major components, the pulsed modulator and the RF power source.

The function of the modulator is to provide high voltage pulses to the microwave transmitter [30]. The high voltage/current and short duration pulses required by the RF power source and the injection system are produced by a pulsed modulator.

The RF power source is either a magnetron or a klystron. Both power sources utilise thermionic emission and use acceleration and deceleration in vacuum for the production of high power RF fields.

A magnetron is a microwave power oscillator that belongs to the family of electron tubes called crossed field devices [31]. In these devices the magnetic and the electric field are produced in perpendicular directions so they cross with each other. The magnetron consists of an anode, a cathode and resonant cavities where oscillating magnetic and electric fields are produced [32]. Electrons are produced by thermionic emission and an electrostatic field is applied to push them towards the anode. An axial magnetic field is applied perpendicular to the radial motion of these charges causing them to move in a circle. The cavity exhibits a resonance which is equivalent to a resonant parallel circuit. When the electrons reach a point where there is an excess negative charge they are pushed back around the cavity where they are transferring energy to the oscillation at the natural resonant frequency of the cavity. This particular oscillation leads to the production of electromagnetic waves which is the output of the magnetron.

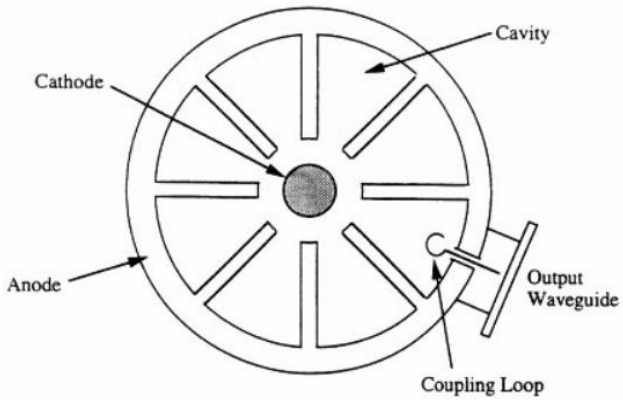

Figure 1-3. Cross-section of a magnetron.

Klystrons belong to the class of devices called linear beam tubes. A schematic of a klystron is shown in Figure 1-4. The basic components of this beam tube are the input cavity, the electron beam and the output cavity. These cavities are electromagnetic cavities whose resonant frequencies are equal to the operational frequency of the amplifier. Once the electron beam is formed, it passes through the input cavity experiencing the electric field of the cavity in the gap region which modulates the veloctu of the electrons before entering the drift tube sections and then the output cavity which induces electromagnetic fields which decelerates the modulate electron beam with the conservastion of energy resulting in an increase in amplitude of the electromagnetic wave. The input cavity plays an important role with some of electrons getting accelerated and some of them decelerated depending on the phase of the gap electric field. This velocity modulation permits bunching of the electrons while they are propagating in the drift tube section. The combined energy of the bunched electrons is transferred at the output cavity where an amplified version of the input signal is induced.

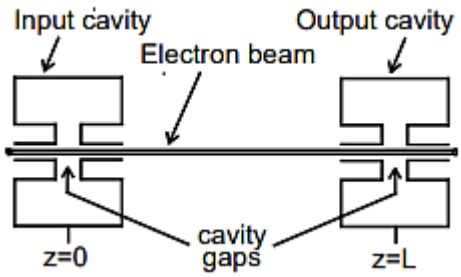

Figure 1-4. Schematic of a two-cavity klystron [33].

1.2.1.3 Accelerating wave structures

There are two types of accelerating wave structures that have been developed for the acceleration of electrons. The travelling wave structure and the standing wave structure are shown in Figure 1-5.

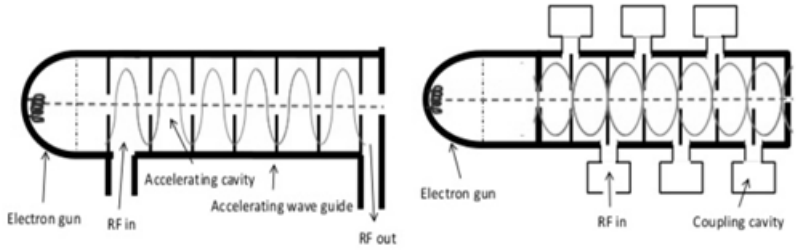

Figure 1-5. A schematic of a travelling wave structure (left) and a standing wave structure (right) [34].

In the travelling wave structure, the microwaves enter the wave structure through the RF input port of the device and the microwaves travel towards the high energy end of the structure. The microwaves will either exit the wave structure and be fed back or they will be absorbed. The design of the standing wave structure differs from the travelling wave structure by having each end of the guide terminated by a conducting disk. In this way the microwave power gets reflected resulting in the formation of standing waves from which it derives its name.

1.2.1.4 Electron beam transport

In medium and high energy LINACs an electron transport system is necessary for guiding the beam to the X ray target. The system consists of different bending magnets and evacuated drift tubes. Three different systems have been developed. These are the 90-degree bending, 270-degree bending and 112.5-degree bending as shown in Figure 1-6. In addition to the magnets, steering and focusing coils are used to propagate the beam to target.

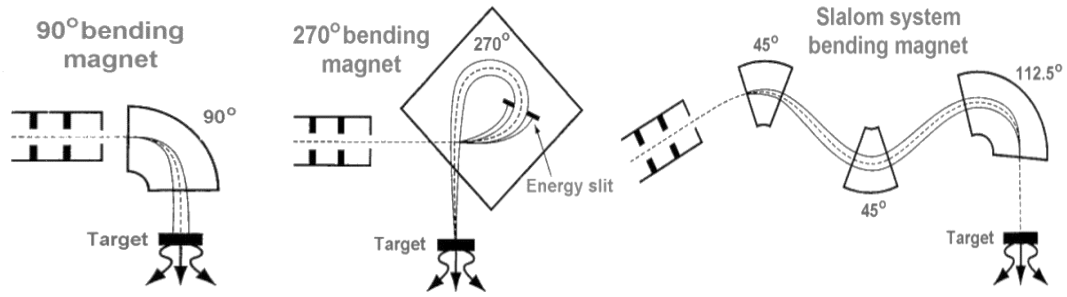

Figure 1-6. The three systems of electron beam bending [34].

1.2.1.5 The demands of the medical LINACs

Research on cancer treatment shows that about 57% of the cancer cases worldwide occur in low and middle-income countries (LMIC) [35]. Radiotherapy is one of the main forms of modern cancer treatment which combined with chemotherapy has a very high success rate [36]. The precision in planning and treatment has advanced majorly in the last two decades. Traditional two-dimensional radiotherapy has been replaced by three-dimensional conformal radiotherapy [37-39], intensity-modulated radiotherapy [40, 41] and image-guided radiotherapy [42-45]. All these radiotherapy treatments are delivered by medical LINACs which are specifically designed to deliver the required energy.

LINACs are expensive medical devices that require continuous expensive maintenance. This becomes a major issue especially for the low and medium-income countries resulting in more than 50% of patients requiring radiotherapy not having access to treatment. The situation is even more dramatic in the low-income countries where the proportion is higher than 90% [35]. Current plans involve the construction of medical LINACs in low-income countries in order to create radiotherapy communities that could be the base for future expansion. The market demand and revenue on medical LINACs globally are shown in Figure 1-7 showing a constant increase every year. This increase implies a bigger demand for more efficient, robust and most importantly reliable electron guns which is the main investigation of this thesis.

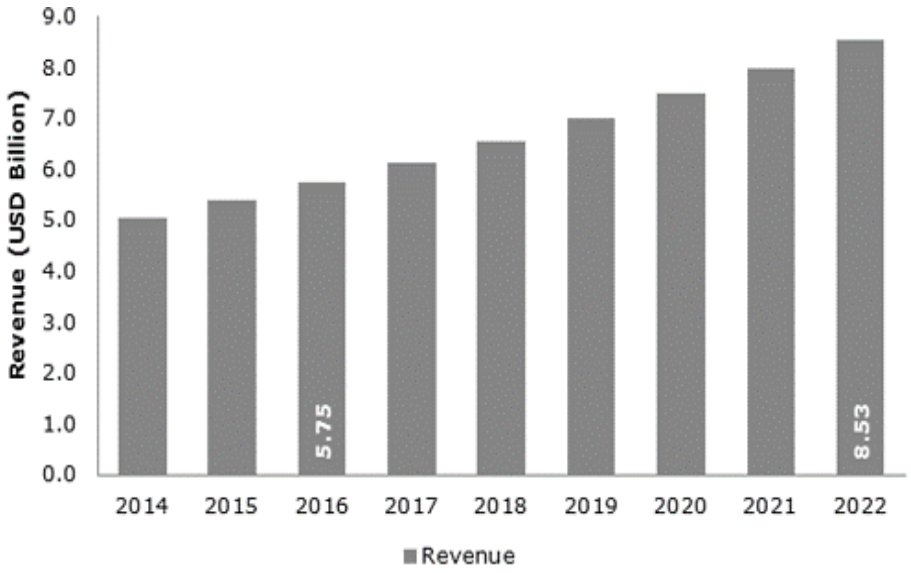

Figure 1-7. Global Radiotherapy market revenue for 2014-2022 [121].

1.2.2 FELs

1.2.2.1 System of the FEL

Classic optical lasers generate beams that are restricted to photon energies determined by discrete quantum states in an atomic gain medium resulting in defined wavelengths [46]. Contrary, the Free-electron lasers (FELs) use a relativistic electron beam from an accelerator as a lasing medium and are capable of operation over the entire electromagnetic spectrum ranging from the microwave to the ultraviolet region. The average power which could be achieved varies from several kilowatts for long pulse duration FELs, up to peak powers of gigawatts for short duration output pulses. Furthermore, FELs are capable of producing extremely bright, ultra-short pulses of femtoseconds (fs) of light which find the application in different fields of physics, chemistry, biology and medicine.

The radiation of the FEL is produced when an electron beam passes through a periodic structure of alternating magnetic field formed in the part called undulator as shown in Figure 1-8. The wavelength of the emitted radiation is given by equation 1-1 [47]

$$\lambda_r = \frac{\lambda_u}{2\gamma^2}\left(1 + \frac{K^2}{2}\right) \qquad (1\text{-}1)$$

where λ_u is the undulator period, γ is the relativistic factor, and K is the undulator strength parameter defined as

$$K = \frac{eB_0\lambda_u}{2\pi mc} \qquad (1\text{-}2)$$

where B_0 is the undulator's magnetic field strength, m is electron mass, and e is the electron charge, and c is the speed of light. It can be seen that the wavelength is strongly dependent on the undulator magnetic period and the strength of the magnetic

field in the undulator. All FELs consist of an electron accelerator and an undulator as the major parts but there are two main different types. The one known as low-gain FEL [48] where the generated light beam is accumulated through the constant interaction of the electromagnetic energy trapped in an optical cavity with electron bunches within the cavity. This type of FEL has a lower wavelength limit of operation due to cavity construction limitations. The other type of FEL is a high-gain FEL [49, 50] for which there is no need for a cavity to operate as all the emission energy is deposited in a single pass through a long undulator with a single electron bunch. The two types of free electron lasers are shown in Figure 1-8 and Figure 1-9.

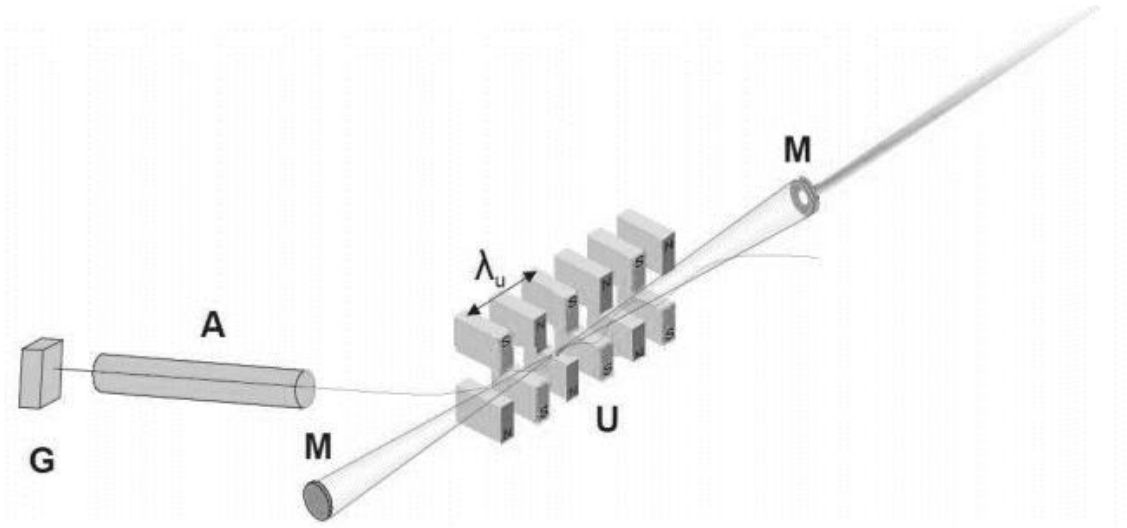

Figure 1-8. A low gain FEL with G-the electron gun, A-accelerator, U-undulator and M-mirror [51].

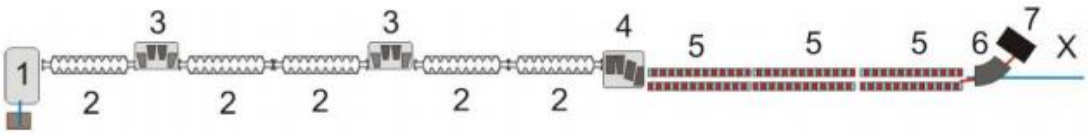

Figure 1-9. A high gain FEL with superconducting electron accelerator modules. 1-electron gun with laser-driven photocathode, 2-Superconducting modules of electron accelerator, 3-electron beam compressor (chicane), 4-electron beam collimator, 5-undulator sections, 6-bending magnet, 7-electron beam absorber, X-ray radiation output [51].

1.2.2.2 Applications of FELs with some examples

The FELs have some unique properties which are very different from radiation produced by other sources like synchrotron sources. These properties involve the pulse length, the peak brightness, and spatial coherence [52]. The pulse length is in the range of tens of femtoseconds, which is shorter than the atomic vibration periods in molecules and almost three orders of magnitude higher than the X-ray pulses from a synchrotron allowing ultrafast science to be developed. Another property is the peak brightness which is 10^9 times greater than a synchrotron source allowing the collection of data in a very short length of time enabling an image of the sample to be taken before radiation damages the sample. Some examples of key science challenges are given below.

The development of novel catalysts and the design of new drugs are examples that require high time and spatial resolution. Understanding the intermediate steps of a chemical reaction, bond making and bond breaking can lead to the design of new drugs by mimicking transition states of biological catalytic processes. This could potentially open up new synthetic capabilities in organic and inorganic chemistry [23].

Another example where spatial resolution and time are necessary is for understanding the dynamics of structural changes in membrane and soluble proteins. This is feasible by capturing the structural dynamics of biological systems in real-time, allowing correlation between the reaction chemistry and protein structural changes. [53].

Warm Dense Matter (WDM) [54] is of central importance in fusion science and laser plasma science. The very high intensities acquired by a tightly focused FEL beam provide the capability to isochorically heat the material to a very high and uniform temperature. Once the Warm Dense Material is created, it expands and cools very rapidly, so it can only be studied with an extremely rapid experiment. The pulses of 10s of fs from an FEL make this possible. Furthermore, they can also be used to study the structural dynamics of the solid-to-plasma phase transition. Another technique which takes advantage of the extremely high intensity of FEL when the beam is tightly focused is called diffraction before destruction [55]. With this technique, it is possible to allow a sample to be probed before it gets damaged due to X-ray radiation. This is possible because the pulse duration is much shorter so it allows more X-rays to propagate through the sample before it is damaged. This technique is critical for biological applications as these samples have a radiation-sensitive biological nature.

Some more examples of FELs for each field and wavelength are given in Table 1-3, with our focus on Infrared (IR) FELs for which thermionic electron guns are used. The increased necessity of research using FELs is shown in Table 1-4.

Condensed Matter	Surface Science	IR
	-Catalysis	IR
	-Adsorption	IR
	-Selective excitation of surface layer or adsorbed molecule	IR
	Semiconductors	IR
	-High Tc SC bandgap	IR
	-Carrier dynamics	IR
	-Electron gas dynamics at metal-insulator junction	IR
	Superconductors	IR
	Magnetic properties	IR
Chemistry	Molecular vibrational excitation	IR
	Reaction dynamics	IR
	Photochemistry	IR
	Molecular cluster, Van der Waals-molecule	IR
	Electronic excitations	UV
	Raman Spectroscopy	UV
	Crossed Photon-Molecular Beams	UV
Biology	Microscopy, Holography, Cellular Dynamics	1-3 nm
	DNA sequencing	0.1-1 nm
Medicine	Surgery	3 μm
	Phototherapy-Selective absorption in pigmented elements	0.7-1 μm

Table 1-3. Examples of FEL applications [56].

Facility (Year of First Operation)	Max Photon Energy (keV)	Beam Energy (GeV)	Pulses/ s	Bunch Charge (nC)	Facility Length (km)	RF Technology
FLASH, Hamburg (2005)	0.3	1.2	27000	1	0.32	SC
LCLS-I, Stanford (2009)	11	13.6	120	0.25	1.7	NC
SACLA, Harima (2011)	15	8.5	60	0.2	0.8	NC
FERMI, Trieste (2011)	0.3	1.5	50	0.5	0.5	NC
European XFEL, Hamburg (2017)	25	17.5	27000	1	3.4	SC
SwissFEL, Viligen (2017)	12	5.8	100	0.2	0.7	NC
PAL XFEL, Pohang (2017)	12	10	60	0.2	1	NC
LCLS-II, Stanford (2021)	5	4	10^6	0.1	4	SC
	25	15	120	0.125	4	NC
HE UPGRADE	12	8	10^6	0.1	4	SC
SHINE, Shanghai (2025)	25	8	10^6	0.1	3.1	SC

Figure 1-10. List of the main parameters of short-wavelength FEL facilities in order of their coming online, and includes two facilities which are under construction and will be online in the next five years. The colour coding relates to the RF technology – superconducting (SC) or normal conducting (NC). The first facility to offer short-wavelength FEL light to users was the pioneering FLASH in 2005, recently upgraded to FLASH-II by including gap tunable undulators. FLASH was originally constructed as an SC linac test facility and the technological advances it produced were critical to the design and success of the European XFEL. The first hard X-ray facility was LCLS-I, which started operations in 2009, and has since been joined by facilities in Japan, the EU, Switzerland and South Korea [134].

1.3 The injector system of LINAC

The electron gun is a basic component of all LINACs. Electron emission takes place through different emission mechanisms, thermionic emission, photoemission and field emission. For all types of electron guns, the specification of the beam is focused on parameters like the beam current, beam emittance, emission current density and some other more specific parameters like bunch charge, bunch length and repetition rate. Examples of the different types of electron guns in literature are presented in the next section.

1.3.1 Different types of the electron gun

1.3.1.1 Thermionic guns

Research on thermionic electron guns used has been conducted by various groups [57-62] [63-66]. Most of them involve a Pierce type diode [57, 63] or triode electron gun [58, 60-62, 66, 67] which is optimised to specific values of beam current, electric field, beam size and any other parameters that are relevant to the specific beam dynamics required. Optimisation is carried out initially with the help of codes like, EGUN[57], TRAK[66], MAGIC[66], CST Particle Studio [68], TURBOWAVE [60], PARMELA [57, 60], MICHELLE [67], and Opera [62]. Typical values found in the literature for the current density, bunch length and bunch charge achieved with this type of electron gun was found to be 10-100A/cm^2, ~200ps and 6-100pC equivalently.

Other techniques like the addition of higher harmonics have been implemented in order to generate shorter duration pulses with a repetition rate equal to the frequency of the RF LINAC [60]. Implementing this technique showed that a 96ps bunch length with a 1nC bunch charge was achieved which is both a shorter and higher current pulse.

Another field of investigation has been focussed on the different materials for cathodes [69]. The main materials are single crystals of hexaboride (Ca, La, Ce, Pr, Gd, Ba) for which emission properties like the stopping range which corresponds to the distance penetrated by the electrons inside the cathode before they lose all of their energy and come to rest, the heat deposited by backbombardment and the current densities were taken into account. Out of all single crystals, CeB_6 was the most promising material because of its excellent emission properties, like high and uniform emission density, and high resistance to contamination [59, 64].

Figure 1-10. Thermionic electron gun showing the cathode and the heater mechanism for the electron extraction (photograph courtesy of TMD Ltd).

1.3.1.2 Photoemission guns

The electron emission of photocathode guns is controlled by a short-pulse laser system. The advantage of the photocathodes is large current density and shorter pulses as the injected time of the laser can be adjusted such that electrons are not emitted when the RF phase is not suitable for electron acceleration. Work with this kind of cathode has been carried out by different groups [70-75]. Typical values for bunch length for comparison reasons are in the range of femtoseconds (fs) compared to picoseconds (ps) for the thermionic cathodes. Higher current densities could also be achieved with this type of electron gun. However, the disadvantage of the photocathode is that the system needs ultra-high vacuum (~10^{-9} Torr) and a high power drive laser.

The performance of a photocathode RF gun depends greatly on the properties of cathode material and the quantum efficiency (QE), which is defined as a ratio of the emitted electrons to the absorbed incident photons. Durable cathodes tend to have relatively low quantum-efficiency, while high-quantum-efficiency cathode materials are invariably very sensitive to vacuum conditions.

Figure 1-11. A cesiated tungsten photocathode [123].

1.3.1.3 Field Emission guns

Field Emission (FE) occurs when the electric field pulls and accelerates the electrons away from the emitting surface. A metallic nano-emitter will emit electrons when a negative potential is applied. It can produce a focused spot having a radius smaller than 50 Angstrom and provide about 1000 times more intensity than a hot filament system. The increase in intensity is made possible by using a field emission electron source operating at a pressure of 10^{-9} Torr [76, 77]. Using this approach, much higher current densities have been measured compared to those from a hot filament tip reaching up to 928A/cm^2 [76-80]. However, field emission cathodes can suffer from some well-known practical difficulties like their requirement of ultrahigh vacuum conditions and current instabilities something that will cause limitation for use in FELs and most importantly in medical LINACs.

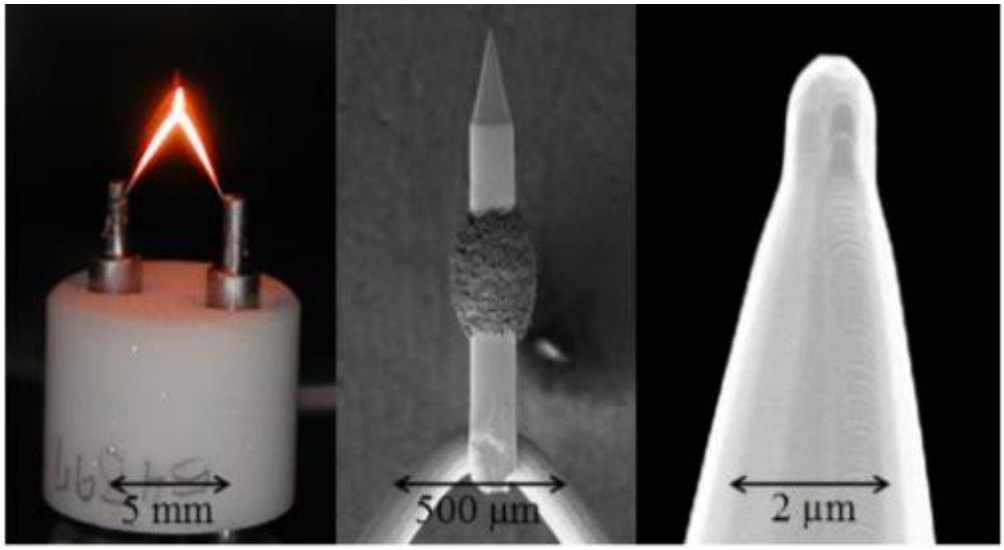

Figure 1-12. A Schottky emitter, a type of a field emission electron gun at different length scales [124].

1.4 Objectives of the PhD study

With the increasing demand for LINACs for applications like Medical LINACs and FELs, more efficient, long-lived and cost effective electron guns need to be designed. The main objective of this PhD project is to study the modulation of an electron beam produced by a thermionic cathode to significantly improve the portion of the electron beam that has the correct phase to be accelerated in various particle accelerator applications. Overall, the main motivation of this study was the design of a robust electron gun with long lifetime which is able to deliver a beam with low emittance and low energy spread at the entrance of the LINAC. Furthermore, to be able to provide higher capture efficiency of the injected beam into the LINAC compared to existing electron guns and finally develop tools which allow for accurate beam simulations. For the design of the electron gun certain specifications of the LINAC were given by our collaborator Dr. Boris Militsyn of ASTeC, Daresbury laboratory. The initial electron beam parameters of the proposed LINAC are listed in Table 1-4. Particular attention needs to be paid to the bunch length value which needs to be as short as possible and in this case <200ps. This value comes from the current literature where the minimum achievable bunch length obtained without magnetic compression corresponds to values between 100 and 200 ps. The bunch length is a crucial parameter as it determines how many of the electrons get captured in each of the RF acceleration buckets of the linac without getting lost to the acceleration process.

Pulse modulation using a triode type of cathode can significantly increase the capture efficiency of the injected electrons by being able to match the RF acceleration buckets. A thermionic cathode is very robust however the longer pulses mean not all electrons are being able to fill the acceleration RF buckets. These electrons will either collide

with the cavity's structure wall or back-bombard which is the transient heating of the cathode surface due to electrons emitted late in the RF cycle causing thermal issues which results to the shortening of the cathode's lifetime. To investigate how this can be overcome, a theoretical model along with the design and simulation of a Pierce electron gun using different simulation packages was carried out. Both 2D and 3D simulation packages were used firstly for the optimisation process of the geometry of the electron gun and secondly for the investigation of its performance. A schematic of the thesis outline is shown in Figure 1-14. Out of this investigation questions studied include: what is the minimum pulse that can be achieved with the available driving RF frequency?; does the theoretical model agree with the simulation work?; what are the reasons for any discrepancies that may arise?; how are different parameters like bunch charge and bunch length related?; what is the emittance for the minimum pulse length achieved and how do different designs of the grid affect the current, bunch length/charge? To answer these questions 2D simulations were carried out using TRAK and MAGIC for the static and the RF gun respectively. Using TRAK, the optimisation of the static gun was carried out and the optimised geometry was transferred in MAGIC where the RF modulation took place and its performance was examined. Furthermore, 3D modelling using CST Particle Studio was used to compare with the above findings along with investigation of two different designs, spider web and pepper pot grid on the performance of the electron gun. Implementation of higher-order harmonics of the driving RF frequency as another technique of potentially shortening the pulse length was also investigated.

Overall, a gridded thermionic cathode electron gun has many advantages including a compact demountable configuration, long lifetime, no requirement for a drive laser

and taking into account the resulted values of bunch length, bunch charge and emittance we came into conclusion that this gun design is perfectly suitable for infrared FELs and Medical LINACs.

Beam energy (MeV)	6
LINAC Acceleration frequency (GHz)	3
Repetition rate (Hz)	300
RF pulse length (μs)	7.5
RF gated frequency (GHz)	1.5
Bunch charge *Q* (pc)	33.3
Bunch length τ (ps)	< 200ps
Peak current (A)	Q/τ
Pre-acceleration voltage (kV)	25
Beam radius (mm)	<2.5

Table 1-4. Specifications of the LINAC courtesy of Dr. Boris Militsyn of ASTeC, Daresbury laboratory.

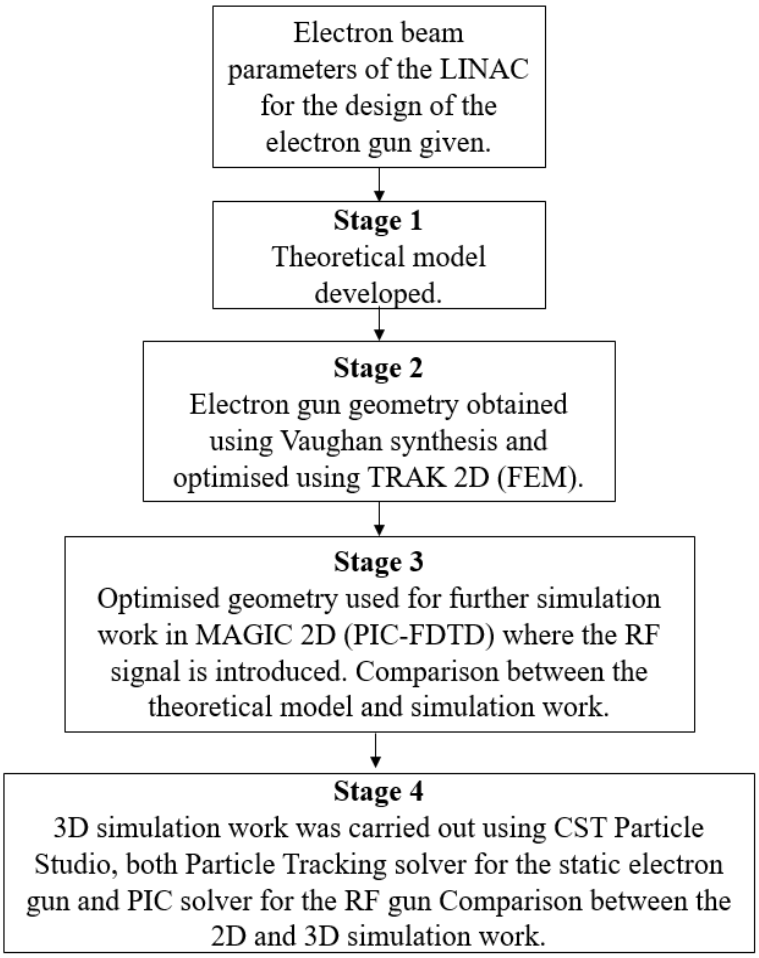

Figure 1-13. Thesis outline where each stage describes the process followed for designing the electron gun.

Summary

The aim of this chapter was to provide an introduction to the project along with the objective of this PhD study, the applications of this type of electron gun for different applications like Medical LINACs and Free Electron Lasers (FELs) and the existence of different types of electron guns depending on the type of the electron emission used.

Chapter 2

2 Theory of Electron Guns

Electron guns have different emission mechanisms depending on the type of their cathode. These are thermionic emission, photoemission and field emission. These mechanisms are described in more detail in this chapter. Furthermore, the design of a Pierce electron gun for overcoming the electron repulsion forces and the concept of emittance and brightness is explained.

2.1 Production of electrons and emission mechanisms

2.1.1 Fermi-Dirac distribution law

Metals contain mobile electrons that can conduct electric current. Most electrons in metals are tightly bound to atoms and only the free electrons, the valence electrons are able to conduct current. These valence electrons obey Fermi-Dirac quantum statistics.

The number of electrons (dN) occupying the energy states between E and $E+dE$ is

$$dN = D(E)f(E)dE \quad (2\text{-}1)$$

Where *D(E)* is the density of states function equation

$$D(E) = \frac{4\pi(2m_0)^{3/2}}{h^3}\sqrt{E} \quad (2\text{-}2)$$

And f(E) is the Fermi-Dirac distribution function.

$$f(E) = \frac{1}{1+e^{(E-E_F)/k_BT}} \quad (2\text{-}3)$$

Where,

N(E) and F(E) are the density of states and Fermi-Dirac distribution functions, respectively

h = Planck's constant

m_e = Electron mass

k_B = Boltzmann's Constant

T = Temperature

E = Energy

E_F = Fermi Energy

At 0 K the electrons occupy the lower energy states. The highest energy state amongst them is the Fermi level. No electron would be found in energy states above the Fermi level. However, as the temperature increases, the electrons gain energy, rising from energy levels just below E_F to levels above E_F. This result can be expressed schematically as shown in Figure 2-1 [81].

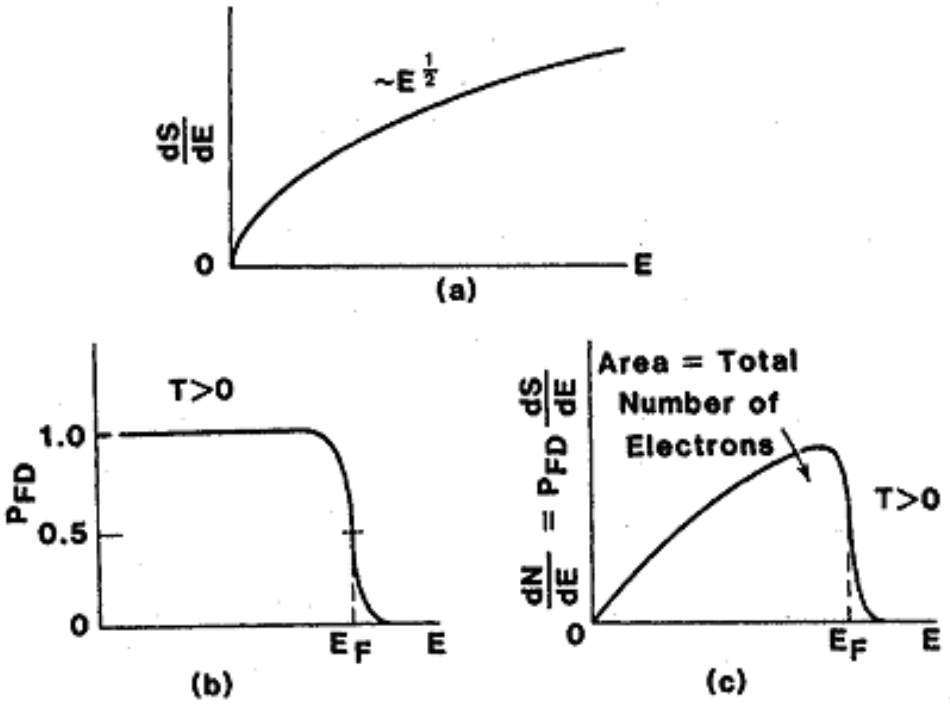

Figure 2-1 (a) Density of states, (b) Fermi-Dirac probability factor, and (c) Electron energy distribution function versus electron energy [132].

.The population of electrons in the high energy 'tail' of the distribution is strongly dependant on temperature, where an increase in temperature increases the population in the 'tail'. Only electrons in this region have sufficient energy to overcome the work function and escape from the emitter. This is the basis for thermionic emission.

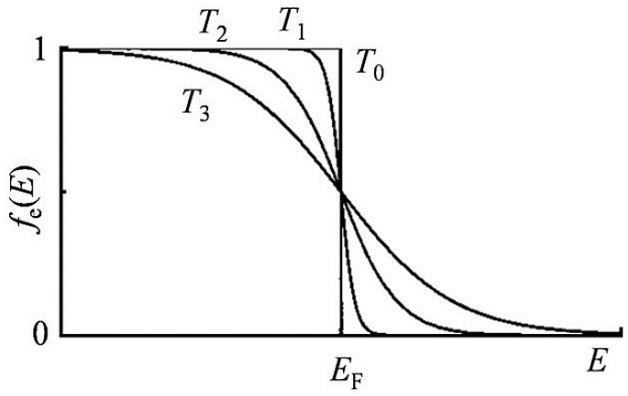

Figure 2-2. Fermi-Dirac distribution at different temperatures $T_3 > T_2 > T_1$ [126].

2.1.2 Work function and conditions of electron emission

The escape of electrons from a metal surface is determined by the relative magnitude of the energy and momentum of the electrons. An electron must possess energy greater than work function energy $e\Phi$ where Φ is the work function corresponding to the minimum amount of energy for the electron to leave the metal surface. Increasing the electron's energy so electrons have higher energy to escape the surface can occur by the following methods:-

1) Increasing the temperature T of the metal (thermionic emission).
2) Supplying the electrons energy E by external radiation (photoemission).
3) Reducing the effective work function Φ of the metal with the application of an applied electric field (Schottky effect).
4) A combination of 1), 2) and 3)

Another way to extract electrons from a metal surface is by field emission. When a very strong external electric field is applied, the width of the potential barrier is reduced so that electrons can tunnel through the barrier and escape even though they don't have sufficient energy to overcome the barrier. Each one of these emission mechanisms is examined in the next sections.

2.1.3 Thermionic emission

One way to make electrons escape the metal is by increasing the temperature of the metal. By increasing the temperature, the electrons gain kinetic energy so they have enough energy to overcome the work function potential barrier of the metal to escape into vacuum. This is demonstrated in Figure 2-3. Electron emission resulting from the heating of a surface is referred to thermionic emission [81].

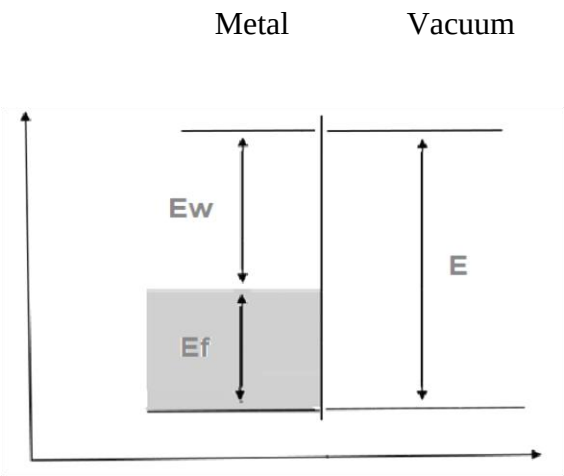

Figure 2-3. Condition for thermionic emission to take place, $E \geq E_f + E_w$.

Electrons are emitted when the temperature is raised such that the component of their energy in a direction perpendicular to the cathode surface is $E_f + E_w$ or greater. This gives rise to a critical momentum required for an electron to overcome the material work function.

$$\frac{P_{xc}^2}{2m} = \frac{1}{2}mu_x^2 = E_0 + e\phi \qquad (2\text{-}4)$$

If the number of electrons per unit volume, n_e, having momentum $P_x > P_{xc}$ can be found then the emission current density, J, can is given by:

$$J = p\,u_x = e\ n_e u_x \qquad (2\text{-}5)$$

Using this method the current density can be calculated and is given by

$$J_{RD} = A_0 T^2 \exp^{\left[-\frac{e\varphi}{k_B T}\right]} (\mathrm{A/m^2}) \qquad (2\text{-}6)$$

which is known as the Richardson-Dushman equation for thermionic emission where A_0 is a constant having the value 1.2 x 10^6 Am^{-2} K^{-2} and T is the cathode temperature in Kelvin (K) and k_B is the Boltzman's constant, 8.617 x 10^{-5} eV.K.

J_{RD} = Richardson Dushman thermionic emission current density

$A_0 = (4\pi m e k_B^2/h^3) = 1.2 \times 10^6$ Am^{-2} $°K^{-2}$

φ = surface potential ($e\varphi$ = work function energy).

The most significant aspect of equation 2-6 is the exponential variation of the current density with work function (ϕ) and temperature (T). The T^2 term is, by comparison, negligible. Experimentally, the value of A_0 is found to be significantly lower than predicted (about a quarter to a half the value). This is because the work function was assumed to be independent of temperature, when in reality it normally varies approximately linearly.

The Richardson-Dushman can be rewritten in an attempt to account for this variation:

$$J = J_{RD} \exp^{[-\frac{e\alpha\varphi}{k_B T}]} (A/m^2) \qquad (2\text{-}7)$$

It is assumed that the work function is constant across the entire surface of the emitter. If this is not the case then the vast majority of the emission will be from the lower work function region, reducing the effective area of the cathode.

From the Richardson–Dushman equation it is clear that to obtain high values of emission, the work function must be low and the temperature must be high. Materials with low work function tend to have a low melting temperature. Barium has a low work function but has a moderate melting temperature. Therefore, barium is

commonly used in thermionic cathodes often in the form of barium oxide. However, modern cathodes operate at temperatures around 1000 ^{o}C leading to Barium evaporation. Once the barium is evaporated the cathode can no longer produce the required electron emission current density. But by having a reservoir of barium in the porous tungsten the barium is continually replenished allowing cathode lifetimes of 100,000 hours to be achieved, depending on the temperature of operation. The higher the temperature of operation, the shorter the lifetime of the cathode. Work functions of different materials and their melting points are given in Table 2-1.

Material	**φ (eV)**	**Melting point (K)**
Caesium	1.81	301
Barium	2.48	1000
Cerium	2.90	1072
Lanthanum	2.36	1193
Molybdenum	4.3	2895
Nickel	5.0	1725
Thorium	3.4	2118
Tungsten	4.52	3655

Table 2-1. Work function and melting points for various typical materials used in vacuum devices [82].

2.1.4 Space Charge Limited Emission and Child Langmuir law

Most cathodes operate at a temperature high enough to begin life in the space-charge-limited (SCL) emission region. During operation and in a region near an emitting cathode where many electrons are present, there is a reduction in the resultant electric field. However, in absence of electrons, the potential increases linearly with the distance across the gap between the cathode and the anode. In such a system there is an equilibrium condition at which point, should the potential start to become positive, more electrons flow to depress it and should the potential become negative, fewer electrons flow raising the potential. When the electric field at the cathode surface is forced to zero by the electron cloud near the cathode surface the emission is said to be space charged limited [83].

Emission in space charge has numerous benefits. For example, the cathode temperature and surface condition do not affect the emission and so the temperature across the cathode needs no longer be uniform to obtain uniform emission. The relation between voltage and current in a space charge limited diode is given by the Child-Langmuir law

$$J = \frac{4}{9}\varepsilon_0\sqrt{2\eta}\frac{V^{3/2}}{x^2} \qquad (2\text{-}8)$$

Where J is the current density (I=JA, with A being the area of the cathode), ε_0 is the dielectric constant of free space, η is the electron charge to mass ratio, x is the distance from the cathode to the anode and V is the potential at x.

For a parallel-plane diode

$$I = PV^{3/2} \qquad (2\text{-}9)$$

$$P = \left[\frac{4}{9}\right]\left[\frac{A\varepsilon_0(2\eta)^{1/2}}{d^2}\right]$$

Where the assumption $A >> d^2$ has been made, and

I = Space charge limited (S.C.L.) emission current

P = Perveance of the diode (A/V)

V = Gap Potential Difference (V)

d = Electrode spacing (mm)

A = Electrode area (mm^2)

η = Electron charge to mass ratio (kg/C)

P is known as the diode perveance, the value of which describes how significant the space charge effect is on the beam's motion. I is the emitted current and V is the potential between the cathode and the anode. Importantly, perveance is a function only of diode geometry. The perveance may also be readily evaluated for co-axial and cylindrical geometries. For more complex geometries it may be possible to evaluate the perveance numerically. Whilst the perveance varies from one geometry to the next, all geometries obey the equation $I=PV^{3/2}$.

2.1.5 Photoemission

Photons having energy greater than or equal to the cathode work function can cause electron escape from the metal's surface. Based on the quantum theory of photoemission, a three-step model for photoemission was developed. According to it, the photoemission process can be divided into 3 steps:

1. Optical absorption and photoexcitation of an electron in a solid.
2. Transport of the electron through the solid to the surface.
3. The escape of the electrons through the solid surface into vacuum.

This three-step process is shown in Figure 2-4 [84].

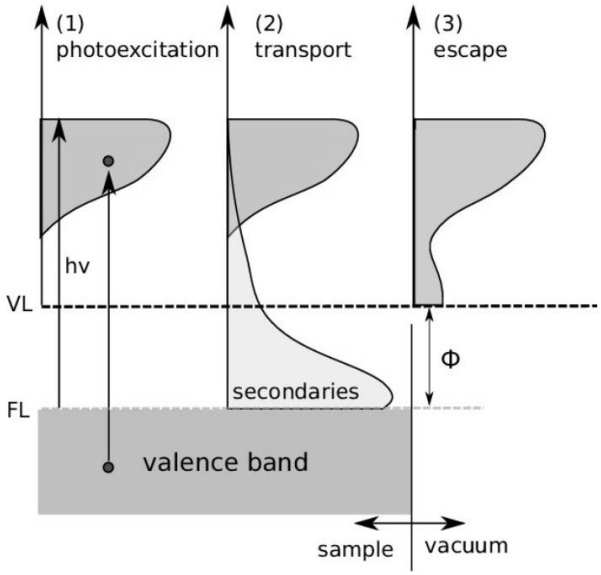

Figure 2-4. Three-step model for photoemission. Initially photons are absorbed and photoelectrons are excited moving towards the surface. These photoelectrons experience inelastic scattering which leads to the creation of secondary electrons. Finally, these photoelectrons escape to vacuum.

2.1.6 Photocathodes

For typical work functions from 3 to 5 eV the required wavelength, λ range from 250 to 410 nm. However only after coherent laser sources evolved were the UV photons fluxes high enough to be interesting for photocathode applications.

Given a laser that supplies sufficient energetic photons, the total current available from a photocathode is given by

$$J = P_{\text{laser}}\, x\, (\lambda_{\text{laser}}/hc)\, x\, QE \qquad (2\text{-}10)$$

Where QE is the quantum efficiency for photoelectron creation and escape which is usually dependent on λ_{laser}.

Photocathodes can be divided into two classes based on quantum efficiency. These are the low QE which are characterised by having reduced vacuum requirements and are relatively easy to use and the high QE ones. High QE photocathodes usually require a good vacuum and have a more sophisticated fabrication procedure.

2.1.7 Schottky effect and field emission

Another way for electrons to escape and increase emission is when an electric field is applied to an emitting surface. The reason for this observation is due to the effect the applied field has on the energy barrier of the emitter causing more electrons to overcome it and escape as shown in Figure 2-5 [85]. By applying an electric field to an emitting surface, the surface potential is depressed, and the energy barrier that an electron must overcome to escape from the emitter is reduced. This is known as the Schottky effect.

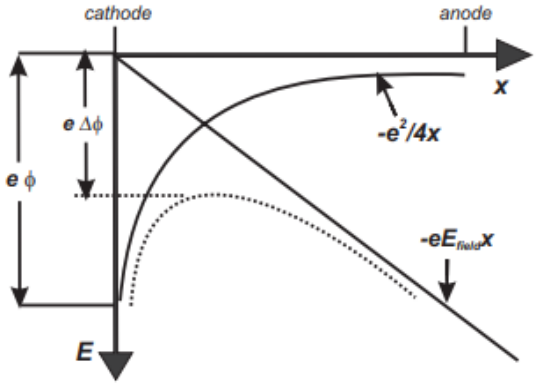

Figure 2-5. Effect of the external field on the potential energy results in the increase of the emission current demonstrating Schottky effect. Near the cathode surface the electric field, E_{field} reduces the barrier electrons need to overcome in order to be emitted so more electrons are emitted.

In effect, the work function is reduced by eΔφ and can be included in the Richardson Dushman equation accordingly. Equation 2-11 highlights the required modification.

$$J = A_0 T^2 e^{\left[-e\frac{(\varphi-\Delta\varphi)}{k_B T}\right]} = J_{RD} e^{\left[e\frac{\Delta\varphi}{k_B T}\right]} \qquad (2\text{-}11)$$

Where, J is the emission current density and

$\Delta\varphi = \left(\frac{eE}{4\pi\varepsilon_0}\right)^{1/2}$, where E is the strength of the Electric field and ε_0 is the permittivity of free space.

The Richardson Dushman current density J_{RD} is sometimes reffered to as the 'zero field' current density, and is a useful parameter for comparing the performance of different cathodes.

Now as the electric field applied to the surface of a cathode is increased to 10^9-10^{10} V/m, it is found that electron emission increases very rapidly, in violation of the behaviour predicted from the Schottky effect. Furthermore, the increase in emission is

almost independent of cathode temperature. In this case, quantum tunnelling takes place leading to field emission.

In field emission, the large E-field results in distortion of the shape of the potential barrier between the cathode surface and vacuum. The electron energy profile is like that for the Schottky effect except that the applied field is much larger. The barrier becomes thinner and lower thus some electrons can quantum mechanically tunnel through as shown in Figure 2-6 [86].

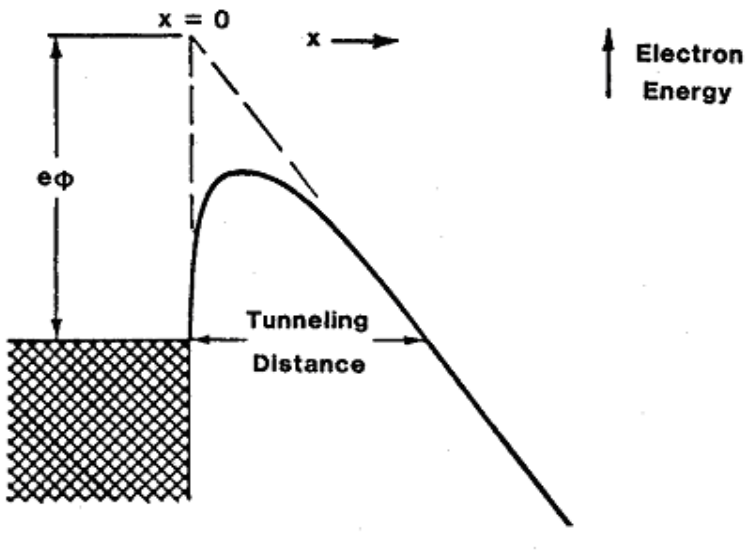

Figure 2-6. Diagram of work function potential at surface of material under application of a very strong electric field (~10^9 Vm-1).

This narrowing of the potential barrier at high field levels allows for the possibility of electron tunnelling. Due to the quantum mechanical nature of the electron, electrons in the bulk of the cathode with energy insufficient to 'ride over' the barrier, may in fact, with a certain quantum probability (dependant on the barrier dimensions, which in turn are solely a feature of material and electric field strength), pass through the barrier. The tunnelling current is only observable when it becomes a significant

fraction of the total emission current density, but then it increases exponentially with electric field strength to become the dominant emission mechanism.

Fowler and Nordheim [127] calculated the tunnel probability through the barrier and derived the following relationship between the current density J and the electric field E, for a perfect metal with a Fermi-Dirac electron density at 0 K:

$$J = \frac{A.E^2}{\Phi} \exp\left(-B\frac{\Phi^{3/2}}{E}\right) \qquad (2\text{-}12)$$

where $A = 1.54{\cdot}10^{-6}\ \mathrm{A/V^2}$ and $B = 6.83{\cdot}10^{9}\ V/m$

E = Electric field in $\mathrm{Vm^{-1}}$

J = Current Density in $\mathrm{Am^{-2}}$

Φ = Work function in electron volts

A and B are largely independent of electric field in the range considered.

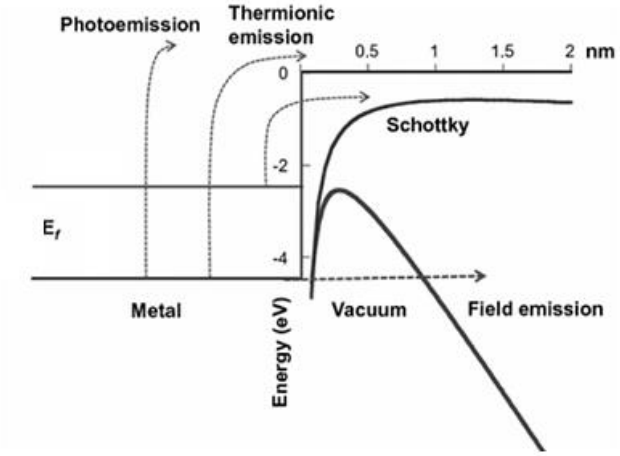

Figure 2-7. Distortion of the potential barrier shown for both the Schottky effect and Field Emission. The energy profile for the Field Emission is like that for the Schottky effect. However the width of the potential barrier is narrower which increases the probability of an electron tunnelling through which leads to an increase in the emission current density [128].

2.1.8 Field emission cathodes

Field emission cathodes promise extremely high current densities with no external source, instant-on (no heater warm-up) and have the potential for achieving extremely high-frequency emission modulation.

Field emission modifies the shape of the barrier both by lowering it due to the Schottky effect and by thinning it due to the applied field so that electrons may quantum mechanically tunnel through the barrier from the metal into the vacuum. Thus an electron at the Fermi level E_F has a finite probability of tunnelling through the modified barrier.

As with other cathode types, a field emitter cathode can be damaged by ion bombardment. Energetic ion impacts can damage the low Φ surface, thereby leading to non-uniform emission. Stable field emission current requires stable emitter geometry. Thus long-lived field emission devices generally require clean ultrahigh

vacuum environments to minimise the presence of gases that could lead to such damaging ion back bombardment of the cathode.

2.1.8.1 Field emission arrays

In this type of cathode, an array of microscopic silicon or metal spikes (nanometres in diameter) is separated from an anode grid with an insulator. The anode is situated in very close proximity to these spikes and as such, when a voltage is applied across the anode cathode gap, the electric field enhancement at the tips becomes large enough for the extraction of electrons via electric field emission. This type of cathode can be pulsed very quickly and is therefore good for applications requiring high duty cycles. However, these cathodes are very expensive to fabricate and are easily damaged. In particular, they are susceptible to damage through ion bombardment which has proved difficult to avoid over a reasonable operation lifetime.

2.1.9 Domains of emission

The mechanism by which electron emission is constrained is dependant on the accelerating electric field due to the applied anode voltage, and the cathode temperature. Figure 2-8 illustrates the mechanisms dominating current flow in a thermionic diode, with variation in anode voltage. At low voltages, the cathode can supply sufficient current to satisfy the Child-Langmuir law and operate in the space charge limited regime. As the potential difference between the anode and cathode is increased there is a transition region where some parts of the cathode surface are unable to supply the required current and enter the temperature limited regime, while other parts maintain operation in the space charge limited regime. This can be seen in Figure 2-8 as the knee in the curve between space charge dominated and temperature

dominated emission. Once the potential difference is high enough, the diode is fully temperature limited and the current increases slowly with an increase in applied voltage. As the potential difference is increased to very high voltages (~10^9 Vm^{-1}), the electric field at the cathode surface reaches a high enough level that the tunnelling of electrons from the surface makes a significant contribution to the total current. Here, the cathode is now operating in the field emission regime. Particular care must be taken in the manufacture of the beam forming electrodes as microprotrusions from the surface of the material can cause field enhancement of several orders of magnitude, thrusting these areas into the field emission regime at much lower voltages than expected and causing degradation of the electron beam.

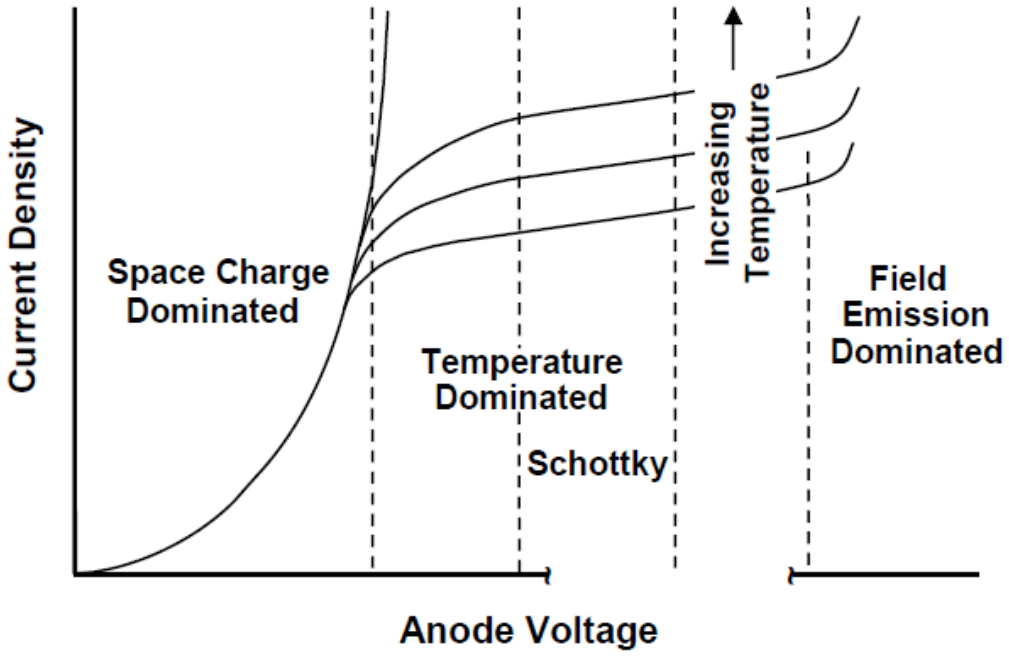

Figure 2-8. Mechanisms dominating current flow through a thermionic diode [132].

2.1.9.1 Oxide cathodes

The first thermionic cathodes were made from pure tungsten but because of the high work function there was a need for high operating temperature too. However, a tungsten cathode was robust with a high current emission and wasn't prone to poisoning. For some applications, a small percentage of thorium was mixed with the tungsten. Thorium diffuses to the surface of the tungsten, reducing the work function therefore permitting the use of lower operating temperature.

A mixture of barium, strontium and calcium carbonates is commonly used for a specific kind of cathode which is so-called oxide cathodes. These are applied to a metal base (usually nickel) and then activated in vacuum. Activation consists of heating and reducing carbonates to oxides.

The manufacturing process of an oxide cathode involves either painting or spraying of a Barium-Strontium-Calcium carbonate emission layer onto a nickel cathode base [87]. These carbonate powders are mixed with nitrocellulose binder which eventually is burned off converting to oxides. However, once converted these oxides can be easily poisoned by the presence of water vapour, oxygen, CO_2, so the cathode must be kept under good vacuum conditions. Oxide cathodes have low work function Φ between 1.2 and 1.8 eV.

2.1.9.2 Dispenser cathodes

A dispenser cathode is more robust against poisoning however it has a higher work function Φ of about 1.8 to 2 e V. These dispenser cathodes are capable of electron current densities of 2-4 A/cm^2 with a lifetime of 100,000 h. Dispenser cathodes are

divided into 2 classifications: reservoir and impregnated. Both types are discussed below.

For the reservoir type of cathode, barium is stored in a reservoir. As the cathode is heated barium migrates from the reservoir through the tungsten and up to the cathode's surface where it helps maintain low Φ. Some of the difficulties associated with this cathode are the slow rate at which barium is supplied and the possibility of blocking the tungsten pores with by-products thereby restricting or cutting the barium supply. Significant improvements have been made by modifying the barium compounds increasing the control over porosity and adding thin top coatings such as osmium or osmium/ruthenium.

In another kind of dispenser cathode, the Ba compounds are impregnated throughout the porous tungsten matrix with no underlying reservoir. For these types of cathodes, the lifetime is limited by the finite amount of impregnated materials, the application of thin overcoating and also the addition of enhancing metals such as osmium, ruthenium, iridium or rhenium to the porous tungsten matrix [88]. In more detail, the emissive mix is impregnated into the porous tungsten cathode pellet. The most common mix consists of five parts BaO, three parts CaO and two parts Al_2O_3 and is frequently referred to simply as 5:3:2 [89]. The whole process involves the cathode being heated to the operating temperature so barium is released from the interior of the tungsten matrix by reactions of the emissive mix with the tungsten. The freed barium then migrates to the surface of the emitter creating some so-called "islands". The sizes of these "islands" depend on the temperature and age of the cathode. As the temperature is increased, the rate at which barium migrates to the surface increases as well the size of the islands. As the cathode ages and the pores in the cathode surface

are depleted, the rate of migration of barium to the surface decreases, and so the islands become smaller. In those portions of the emitter surface covered by barium, the barium atoms interact with and reduce the work function of the surface. In those regions not covered by Barium the work function is that of the base-emitter material. Because of the large differences between the work functions of the areas covered by barium and those not covered by barium, some portions of the cathode operate in space-charge limited condition and others operate in the temperature-limited condition.

2.1.9.3 Scandate cathodes

A new cathode with work function similar to an oxide cathode but with the ease of use of a dispenser cathode was created when scandium oxide (Sc_2O_3) was added to the barium compounds of a dispenser cathode. It was found that the work function was decreased and the current density increased [90].

2.2 Cathode Designs and Applications

An electron gun is used to form electrons emitted from the cathode into a beam. The requirements put on electron beams varies greatly depending on the type of application in which the electron beam will be utilised. The two basic problems which must be overcome are the divergence of the electron beam due to self fields, and the fact that the current density required for most applications is far higher than the emission density of the cathode. In this section the two main types of electron gun are presented.

2.2.1 Pierce Type Gun – Design and Principle

The two basic problems of beam divergence due to self fields and the requirement of current densities higher than can be provided by the emission current density of the cathode, can be tackled in two ways. The first of these involves purely a consideration of the geometry of the gun with respect to the repulsion forces in the beam. The second solution utilises the focussing effects of the electrostatic fields in the diode. A typical Pierce type gun is shown in Figure 2-9.

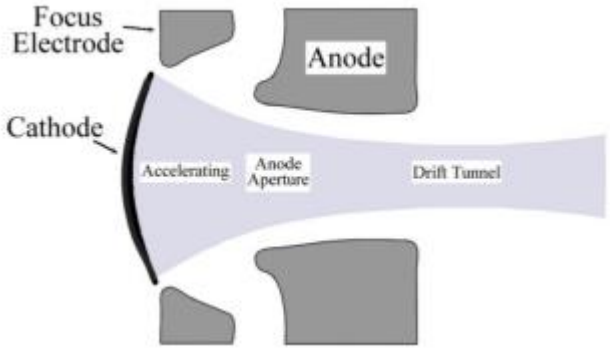

Figure 2-9. Schematic of a typical Pierce type electron gun [133].

The Pierce type gun uses so called Pierce focussing electrodes to create smooth, spherical equipotential profiles in the region of the cathode in order to produce a

uniform laminar electron beam. The use of the Pierce focussing electrodes can be simply explained through consideration of a parallel plane diode, and subsequently these ideas can be extended to a spherical diode and to the Pierce type electron gun geometry illustrated in Figure 2-9 above.

2.2.2 Parallel Plane Geometry

Consider firstly an electron leaving the cathode, taking into account space charge forces in the beam. The electron will follow trajectories as shown in Figure 2-10.

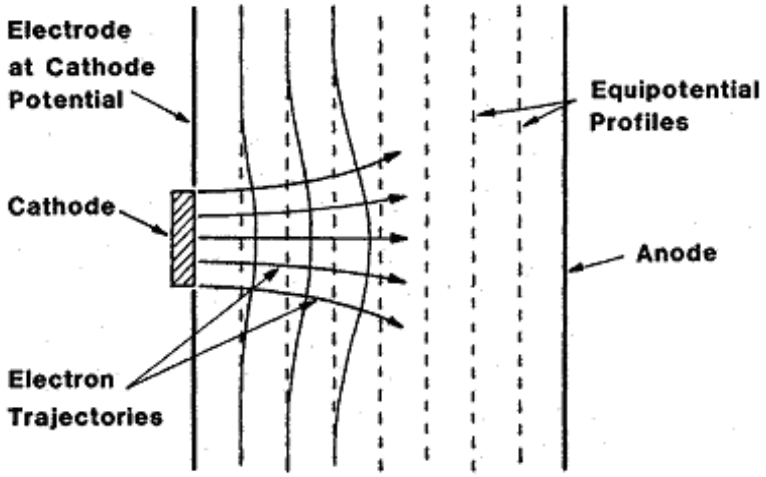

Figure 2-10. Schematic of equipotential profiles in a diode without electrons (dashed lines) and with electrons (solid lines) [133].

To begin, the equipotential profiles in the diode containing no electrons are parallel and equally spaced, denoted by the dashed lines in Figure 2-10. In the presence of electrons, these equipotential profiles are deflected as indicated by the solid lines. Electrons tend to move perpendicular to the equipotential profiles and so the electron trajectories diverge as they move away from the cathode. This is simply describing the electron repulsion forces due to self fields in terms of the equipotential profiles.

To stop the divergence of the beam, a set of electrodes must be constructed to account for the deformation of the equipotential profiles in the presence of electrons. The geometry of such electrodes is shown in Figure 2-11 and was the result of the analytic derivation of Pierce, which gives a self consistent solution for a space charge dominated cathode.

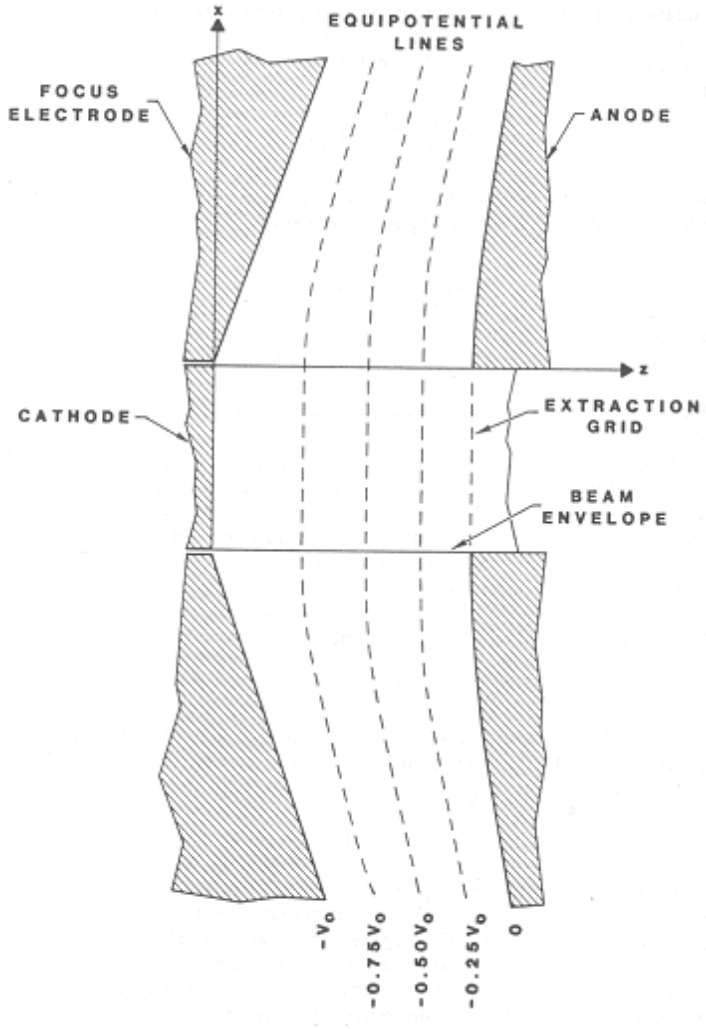

Figure 2-11. Geometry of planar Pierce gun showing calculated equipotential lines within in both the beam and vacuum regions [133].

Pierce's analysis showed that by expressing the electrostatic potential in terms of trigonometric functions, a result could be derived which states the source electrodes

orientation must obey Equation 2-13, and the anode orientation must obey Equation 2-14.

$$4\theta/3 = \pi/2 \tag{2-13}$$

$$(\rho/d)^{4/3}\cos(4\theta/3) = 1 \tag{2-14}$$

Where,

θ = Angle of the electrode with respect to the beam edge

ρ = Length of the electrode

d = Electrode seperation

The most important component is the electrode adjacent to the cathode, described by Equation 2-13, which corresponds to an electrode at an angle of 67.5˚ with respect to the electron beam edge. This surface is known as a Pierce electrode, and generates focussing forces to balance the defocusing self fields of the beam. Although this treatment holds only for this special case, it gives valuable insights into the design of more complex guns.

2.2.3 Converging Beams

To obtain an electron beam current density greater than the emission current density of the cathode, a converging beam is required. To analyse converging beams it is convenient to take the starting point as a spherical diode, the perveance of which is analytically calculable. A conical segment of the spherical diode can now be considered, giving the desired convergent flow, although space charge forces will cause the beam to diverge, as in the parallel plane diode. This can be dealt with in the same manner as detailed above, and an electrode angled at 67.5 degrees to the beam

edge has the desired effect on the equipotential profiles. However, to remove electrons from the diode, it is necessary to cut a hole in the anode, which distorts the equipotential profiles.

At this point it is important to consider the perveance of the diode. Cutting a hole in the anode distorts the equipotential profiles such that there is a reduction in the electric field at the centre of the cathode and a defocusing effect towards the anode. The impact of this effect is dependant on the perveance of the diode as follows.

The effect of the aperture is found to be small if,

$$2r_a << d \qquad (2\text{-}15)$$

Where,

r_a = Aperture radius

d = Cathode to anode spacing

In this case the motion of the electrons is close to that predicted by Pierce. If the opposite is true, then the gun geometry must be modified to obtain a uniform current density. Application of this result to a perveance consideration, it can be shown that the effect of the aperture is small when the perveance satisfies equation 2-16,

$$P << \left(\frac{\pi \varepsilon_0}{9}\right)\left(\frac{2e}{m_e}\right)^{1/2} = 0.6\mu perv \qquad (2\text{-}16)$$

Where all symbols are as previously defined.

Electron gun design can now be classified into low perveance (≤0.1μperv), moderate perveance (0.1-1μperv), and high perveance (>1μperv), with the problems encountered increasing in difficulty as perveance increases. In a low perveance gun, the beam convergence angle is small and the Pierce electrodes suffice. In medium perveance

guns, the field distortions are concentrated in the vicinity of the anode and converging flow can be analysed analytically starting from the perveance of a spherical beam. In a high perveance gun, the electric field is distorted throughout the diode and the addition of classic Pierce electrodes is not enough to completely smooth out the equipotential profiles across the entire cathode. This requires a more complex modification of the focus electrode. Due to the difficulty in creating smooth equipotential profiles at the cathode, the electric field in the centre of the cathode can become depressed, with the result that the current is predominantly drawn from an outer annulus of the cathode as shown in Figure 2-12. For this reason, high perveance guns often use annular emitting regions.

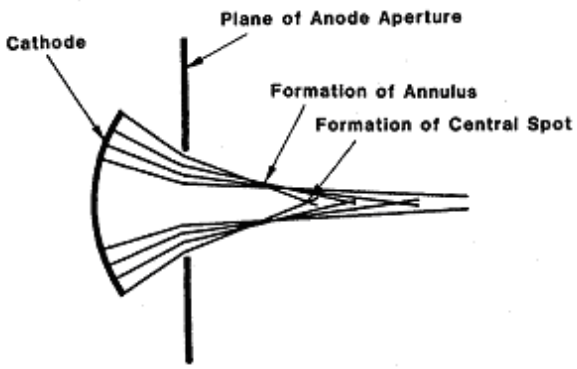

Figure 2-12. Schematic of a electron emission and beam focussing in a high perveance electron gun [133].

2.2.4 Conclusion Pierce gun

This, in the main, is the electron gun of choice for linear beam devices. This technology is very well established and as such, high quality electron beams with very low velocity spread can be formed using the typical Pierce geometry. The geometry is designed such that the electron beams formed have minimal velocity components in directions other than the axial direction. Furthermore, for better control of the beam current grid elements are used.

2.2.5 Electron emission from the grids

The basic concept is to form the grid so that its shape is identical to that of an equipotential contour near the cathode surface. Then, if the grid is at the potential of that contour and intercepts negligible current, electron flow will undisturbed. To interrupt the current flow, the grid voltage is switched negative with respect to the cathode.

A grid must be thin enough to allow the flow of the electrons however at the same time has to be thick to withstand shock and vibration and to be robust against thermal expansion. Most grids are made from tungsten or molybdenum. Materials such as pyrolytic graphite a unique form of graphite have been sued as grids as the material can handle high operating temperatures whilst retaining its shape. The material of the grid plays a big role as ideally one wants to stop the grid from being a primary emitter. In order to avoid this, the use of high work function materials can be implemented along with the use of lower operating temperatures for the thermionic emitter. Coating the grid with a higher work function material is also an option.

Oxide cathodes are of particular importance due to barium evaporation on the grids. The rate of evaporation is a function of both time and cathode temperature. If the grid temperature is high enough the barium will evaporate from the thermionic emitter onto the grid , it will deposit on the surface of the grid forming an emitting surface. To mitigate this affect the thermionic cathode should berun at a low enough temperature to achieve the required current density as well as outgassing the gridto remove contaminants from the grid surface.

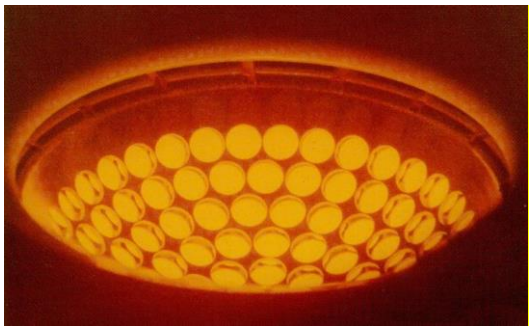

Figure 2-13. Example of a pepperpot type control grid widely used for a Pierce electron gun. (photograph courtesy of TMD Technologies Ltd).

2.3 Electron beam physics

2.3.1 Phase and trace space description of an electron beam

To understand the performance of an electron injector, we need to quantify the quality of the electron beam. Phase space is the basic tool by which charged particle beam transport is characterised.

A particle follows a trajectory described by the position vector [$x(t)$, $y(t)$, $z(t)$] and the velocity vector [$v_x(t)$, $v_y(t)$, $v_z(t)$] using a 6-D mathematical space with axes in both space and velocity [x, y, z, v_x, v_y, v_z] called phase space. A phase space plot is for a specific location (time) in the accelerator, since the particle positions and momenta evolve as a beam propagates. For relativistic particles the phase space is defined in terms of position and momentum [x, y, z, p_x, p_y, p_z]. For an electron beam, the trajectories of the electrons will not cross in phase space because no two electrons can have the same velocity at the same point in space. This means that the 6-dimensional phase space can be separated into one transverse 4-D phase space [x, y, v_x, v_y] or [x, y, p_x, p_y] and one axial 2-D phase space [z,v_z] or [z, p_z]. Now suppose that at some time an arbitrary closed surface S in phase-space is chosen as shown in Figure 2-13 which is bound by volume V. Liouville's theorem states that the phase-space volume V bounded by the surface S is constant, provided that only conservative forces act on the particles. [91]. Furthermore, Liouville's theorem is still valid for large numbers of particles, referred to as "beams" or "bunches" important concepts in accelerator physics.

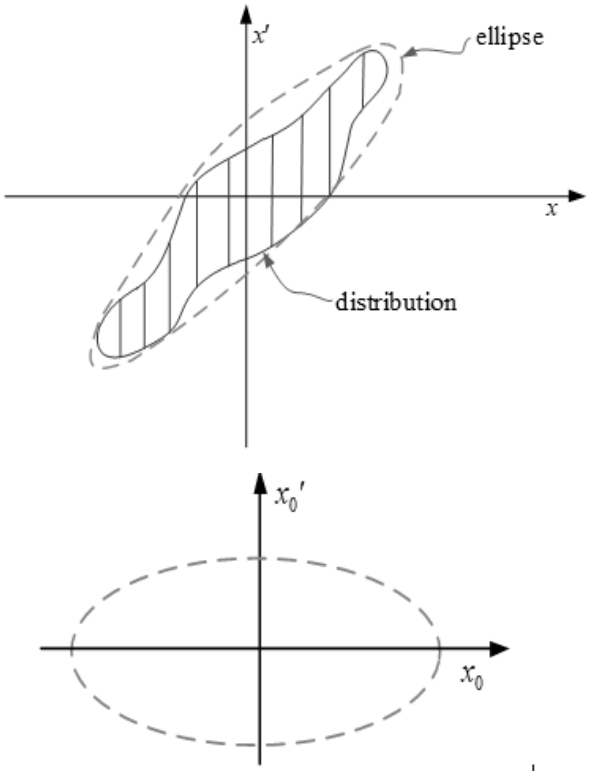

Figure 2-14. Graphic representation of phase space. The particles in the beam can be viewed as an ensemble in phase-space (distribution) evolving in time including the constraint of Liouville's theorem. The lattice ellipse can be filled with particles evolving in time [130].

2.3.2 Emittance of an electron beam and beam brightness

Emittance is the property of a particle beam that characterises beam quality. The emittance is related to the volume occupied by a bunch, or some part, of it, in phase-space. Sometimes motion in each plane is very weakly coupled; in this case it may be possible to treat the motion in each plane independently. Suppose a beam is directed along the z-axis and x and y are the transverse coordinates. The angle a particle makes with the beam axis of symmetry is given by $x' = \frac{dx}{dz}$ and $y' = \frac{dy}{dz}$. The co-ordinates (x, x', y, y') are functions of z and describe the trace of the particle orbit. The co-ordinate space (x, x', y, y') is the "trace" space. Roughly, emittance is an area or volume in the phase space of the particles. The hyperemittance is the product of the 2-D emittances

$$\text{Hyperemittance} = \varepsilon_x \varepsilon_y \tag{2-17}$$

Where

$$\varepsilon_x = \iint \frac{dxdx'}{\pi} \text{ and } \varepsilon_y = \iint \frac{dydy'}{\pi} \tag{2-18}$$

The emittance normally used in accelerator physics is referred as normalised RMS emittance and is given by Equation 2-19.

$$\varepsilon_{norm} = \beta\gamma\varepsilon_x \tag{2-19}$$

Where β and γ are the relativistic functions and ε_x is the root mean square (RMS) transverse beam emittance is defined as

$$\varepsilon_x = \sqrt{\langle x^2 \rangle \langle x'^2 \rangle - \langle xx' \rangle^2} \tag{2-20}$$

where angle brackets indicate averages of the bracketed quantities over the entire bunch.

Beam brightness quantifies the maximum focused power flux of a beam and is a function of emittance,

$$B \approx \frac{I}{\pi^2 \varepsilon_x \varepsilon_y} \qquad (2\text{-}21)$$

The brightness B is measured in units of $Am^{-2}rad^{-2}$ where I is the current of the beam. As it can be seen from equation (2-21) the smaller the emittance the better the beam quality with the brightness defined as the current of the beam divided by the transverse emittance. To increase the brightness, one needs to increase the peak current, or to decrease the emittance, or both. There are different techniques for both increasing the peak current and decreasing the emittance like compressing the electron bunches into shorter time–length and dilute effects such as non-linear fields for the emittance.

Summary

The purpose of this chapter was to provide the introductory theory for the operation of electron guns. This involved the different emission mechanisms for electron production, the different types of electron guns and cathodes, the way the electrons are formed into a beam and the techniques used to overcome the electrostatic repulsion between the electrons to form a high brightness, low emittance beam.

Chapter 3

3 A Theoretical Model of a Modulated Electron Gun

Ideal features of an electron gun used in a LINAC involve the absence of back-bombarding electrons, low energy spread and a short length of the bunches. This thesis aims to investigate the modulation of the electron beam, produced by a thermionic cathode, to significantly improve the efficiency of the electron beam acceleration. The method to achieve this is by the use of a grid to gate the electron beam. This method has attracted a great deal of interest as the electron micro-pulses can be matched with the acceleration RF buckets. From this investigation, important parameters like bunch charge, bunch length and emittance have been studied. Their relation was firstly obtained from a simplified theoretical model and further studied by particle-in-cell simulations. In this chapter, the configuration of the RF gun and the RF cavity is discussed. Furthermore, the operation mode of the electron gun and its validity for our case along with a theoretical model of the RF gun is presented.

3.1 Initial electron beam parameters for the LINAC

The initial electron beam parameters of the proposed linear accelerator (LINAC) supplied by Dr Boris Militsyn, AsTeC Daresbury are listed in Table 3-1. The study was to design a thermionic cathode RF gated gun to meet the required beam parameters, and also to investigate the properties of the electron bunch, including the bunch charge, bunch length and emittance.

Beam energy	$6MeV$
Acceleration frequency	$3\ GHz$
Repetition rate	$300\ Hz$
RF pulse length	$7.5\ \mu s$
RF gated frequency	$1.5\ GHz$
Bunch charge Q	$33.3\ pC$
Bunch length τ	$< 200ps$
Peak current	$Q/\tau\ (A)$
Pre − acceleration voltage	$25kV$
Beam radius	$< 2.5mm$

Table 3-1. Specifications of the LINAC.

It is important to notice the value of the bunch charge which is one of the requirements and the bunch length which needs to be as short as possible which in this case means <200ps. The relationship between these two parameters was investigated and the minimum bunch length for 33pC bunch charge was obtained from the theoretical model described in this chapter.

3.2 Modulation of an electron gun

The electron gun structure is used for generating and shaping a beam of electrons which is injected into an accelerating field. These electron guns can operate in different modes, continuous or pulsed. Bursts of electrons can be generated depending on the method of electron extraction from the cathode.

The configuration of an electron gun could be a diode or a triode. Diode type is configured by the cathode, the focussing electrodes and the anode. Triode type shares the same configuration however a grid is placed at a very close distance in front of the cathode. Diode guns are normally used to generate continuous electron beam or operate at a very low repetition rate to generate electron beam pulses that do not have a short bunch length. Therefore, the electron beam capture efficiency is low in the application as the electron beam source for an RF LINAC. At the same time, one significant disadvantage of the diode gun is the continuous supply of electrons leading to the back bombardment effect (BBE) of the cathode [92, 93]. This is due to the electrons that are emitted in the late phase of the accelerating RF period before the electric field reverses direction. This leads to additional heating of the cathode which causes a ramp in the emission current and shortening of the cathode's lifetime. This problem can be partially solved by using the triode-type configuration, by adding a grid in front of the cathode, and controlling the timing of the electron beam injection by negatively biasing the grid in the electron gun structure. The negative bias on the grid suppresses the electron emission which combined with direct RF modulation via a coaxial cavity can produce a high current bunched electron beam. The configuration of two possible different geometries and the decision of our choice to develop a triode-

type gridded thermioinic cathode electron gun as the electron beam source for the RF LINAC are explained in the next section.

3.3 Configuration of an electron gun with RF gating

There are two possible configurations of the gridded electron gun. Both configurations are shown in Figure 3-1. In both cases the emitted electron current is modulated by an RF voltage which is applied between the cathode and the grid.

Starting with a simpler geometry, the RF gun in Figure 3-1(a) is placed at the entrance of the RF acceleration cells, and the electron beam will be directly accelerated by the electric field in the cells [63, 94]. However, this presents a problem when the cathode needs to be dismounted as the whole structure (RF gun and LINAC) needs to be vented to atmospheric pressure and disconnected from the LINAC which will result in having to re-condition the RF linac making maintenance a complicated task.

The configuration in Figure 3-1(b) contains an additional DC acceleration section. In this case, the electrons get emitted by the cathode and are pre-accelerated resulting in a better beam quality by achieving a smaller beam radius and divergence. Furthermore, with this configuration, the cathode and the acceleration cells are separated enabling the gridded electron gun to be demounted from the RF LINAC reducing the cost of replacing the whole LINAC and reducing the maintenance costs. This configuration is more desirable due to the ability to remove and replace the thermionic cathode without affecting the cavity's parameters hence this configuration is studied in this thesis.

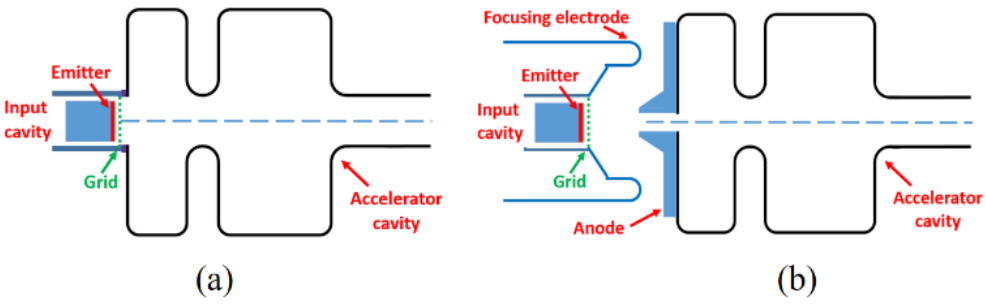

Figure 3-1. Two different configurations of the RF gun, (a) without DC pre-acceleration, (b) with DC pre-acceleration.

3.4 Capacitively-loaded coaxial cavity for the RF electron gun

The RF input signal is applied between the cathode and the grid which is aligned and positioned close to the cathode's front surface. The RF voltage can be driven through a coaxial cavity and the cathode-grid gap plays the role of a cavity gap and contributes to the interaction between the electron beam and the input RF signal. The cathode-grid gap is small to ensure efficient modulation takes place for sufficient bunching of the electrons. A schematic diagram of the cavity structure placing the cavity onto the cathode-grid gap is shown in Figure 3-2 .

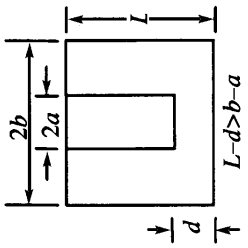

Figure 3-2. The schematic of the coaxial input cavity.

This type of cavity structure is similar to a radial cavity whose inductance, capacitance and resonant frequency can be estimated from equations (3-1), (3-2), (3-3) [131] where L is the inductance produced in the cavity wall, μ is the permeability, C is the

capacitance in the cavity gap, ε_0 is the permittivity of free space, f_r is the resonant frequency, $\varepsilon_r$is the relative permittivity of the material of the cavity, a and b are the radius of inner and outer conductor respectively, d is the cathode-grid gap, l is the height of the cavity and c is the velocity of light in vacuum. The parameters a, b and d are determined by the electron gun geometry and the resonance frequency which depends on the cavity length as described in equation 3-3.

$$L = \frac{\mu l}{2\pi} \ln\left(\frac{b}{a}\right) \qquad (3\text{-}1)$$

$$C = \varepsilon_0 \left[\frac{\pi a^2}{d} - 4a \ln\left(0.765/\sqrt{\{l^2 + (b-a)^2\}}\right)\right] \qquad (3\text{-}2)$$

$$f_r = \frac{c}{2\pi\sqrt{\varepsilon_r}\sqrt{\left\{al\left[\frac{a}{2d} - \frac{2}{l} ln\left(\frac{0.765}{\sqrt{[l^2+(b-a)^2]}}\right)\right] ln\left(\frac{b}{a}\right)\right\}}} \qquad (3\text{-}3)$$

The dimensions of the whole cavity, inner and outer conductor, are decided depending on parameters like the cathode diameter, the resonance of the desired frequency and the cathode-grid gap. The cathode radius (a) and the cathode-grid distance (b) was decided depending on the values used in existing electron guns manufactured in TMD Technologies Ltd. The cathode has to be placed within the inner conductor of the cavity. Therefore, the estimation of the inner conductor's diameter is taken from the cathode diameter. The values of the cavity's dimensions and the resulted values of inductance, capacitance and resonant frequency of the cavity are given in Table 3-2.

$Cathode\ radius, a\ (mm)$	4
$Cathode\ grid\ distance, d\ (mm)$	0.16
$b\ =\ d + a\ (mm)$	4.16
$Length\ of\ cavity, l\ (mm)$	96
$Inductance, L\ \ (nH)$	0.99
$Capacitance, C\ (pF)$	2.56
$Resonance\ frequency, f_r (GHz)$	1.5

Table 3-2. Dimensions of the coaxial cavity and resulting values of inductance, capacitance and resonant frequency obtained from equations (3.1), (3.2) and (3.3) respectively.

As mentioned above the resonance frequency is strongly dependant on the cavity length. The variation of the resonant frequency to the cavity length for different operation modes is shown in Figure 3-3. For the 1.5 GHz frequency the second mode of operation is chosen corresponding to 96mm cavity length.

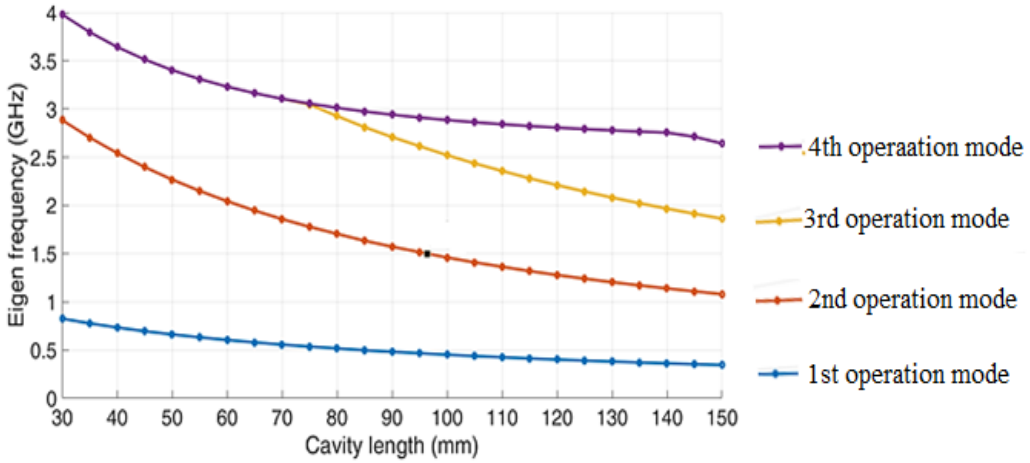

Figure 3-3. Variation of resonant frequency with the cavity length.

One of the most important dimensions is the cathode-grid gap. The gap needs to be small so that efficient modulation takes place for sufficient bunching of the electrons. On the other hand, decreasing the gap distance below a specified value may result in RF breakdown issues.

3.5 Breakdown Physics

Generally, the operation of a structure in the presence of a high electric field is limited by a phenomenon known as vacuum RF breakdown. RF breakdown is a major phenomenon affecting and causing irreversible damage to RF structures where the electic field rises above a threshold and the structure casn no longer mainting the field and a vacuum arc occurs.

RF breakdown limits the input power that can be coupled to the structure as breakdown produces irreversible surface damage inside the structure, electron gun region and RF components. Imperfections on the surface of the structure can be created via the breakdown process, which in turn can lead to further breakdown [95].

One of the main ways that the limit of breakdown in an RF structure can be calculated is known as Kilpatrick's Criterion. This is where breakdown is considered to occur when regular field emission is enhanced by a cascade of secondary electron ejected from the surface via ion bombardment. The probability of field-emitted electrons and the linear dependence of secondary electron on the ion energy, leads to the relation

$$W\,E_K^2 \exp\left(\frac{K_1}{E_K}\right) = K_2 \qquad (3\text{-}4)$$

where W is the maximum possible ionic energy, E_K is the electric field gradient on the surface of the structure, $K_1 = 1.7 \times 10^5$ V/cm, and $K_2 = 1.8 \times 10^{14}$ V/cm. The maximum possible energy of an ion of mass M_0 and charge e, which is accelerated across a large gap between parallel plates, taking into account the transit time, was found to be

$$W = \frac{0.153\,eE^2}{M_0\ \pi f^2} \qquad (3\text{-}5)$$

where f is the frequency of the RF power. Assuming that the ion is hydrogen, the Kilpatrick criterion [96] is then derived as

$$f(MHz) = 1.65\,E_K^2 e^{-8.5/E_k} \qquad (3\text{-}6)$$

This criterion provides a conservative estimate of the voltage at which RF breakdown occurs, and takes the form where f is the frequency in MHz, and E_k is the breakdown field in units of MV/m. Varying one parameter and assuming all others to be fixed, associated limits can be found using the scaling law [97] $\frac{E_K^6 t_p}{BDR^{\frac{1}{5}}} = const.$

3.5.1 Modified Poynting Vector

The quantity which limits the electric field that can be sustained by a structure was long considered to be the surface electric field due to its direct role in electron field emission. The quantity which limits the accelerating gradient of a structure was long considered to be the surface electric field due to its direct role in electron field emission. However, it was found that the power flow in the structure is important due to local heating of potential breakdown sites due to field emission currents [98]. Generally the size and shape of potential breakdown sites are not known before breakdown. Therefore, a standard picture is used where there are small features present on the surface that enhance the local surface electric field. The features are considered to be a cylindrical protrusion of height h and radius r with a rounded top [98].

These protrusions enhance the field by the so-called field enhancement factor

$$\beta = \frac{h}{r} \qquad (3\text{-}7)$$

at the highest point of the tip, such that the local electric field at the tip is βE, where E is the homogeneous electric field around the tip. The most natural way to describe the power flow in a structure is via the Poynting vector.

$$\boldsymbol{S} = \boldsymbol{E} \times \boldsymbol{H}$$

where E and H are the electric and magnetic field vectors respectively. Due to the electric field at the tip, a field emission current is induced which heats the tip. The current creates a corresponding magnetic field, which gives a power flow $\mathbf{P_{FN}}$, which transfers the energy from around the tip through the tip and then along the electron

flow to the outer volume where it is absorbed by the electrons. This process is schematically shown in Figure 3-4.

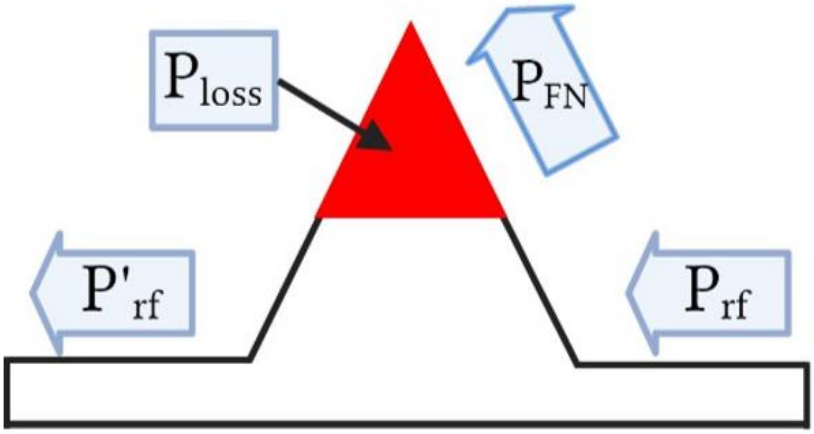

Figure 3-4. A schematic diagram of the power flow near a protrusion on the surface of an accelerating structure which would lead structure to breakdown.

Assuming that a normal conducting structure is being considered, then the surface is most likely to be made of copper. Copper is a very good conductor of both heat and electricity, therefore the amount of power lost in the tip due to heating is much smaller than the amount of power flowing along the tip. As the only source of electromagnetic power flow in the structure is provided by the RF input, the following relationship can be made

$$P_{loss} \ll P_{FN} \ll P_{RF} \qquad (3\text{-}8)$$

where P_{loss} is the power loss in the tip due to Ohmic heating, P_{PN} is the field emission power flow and P_{RF} is the input RF power flow. Assuming a harmonic time dependence of the electric field, the RF power flow is

$$P_{RF}(t) = E_0 H_{RF}^{TW} \sin^2(\omega t) + E_0 H_{RF}^{SW} \sin(\omega t) \cos(\omega t) \qquad (3\text{-}9)$$

where H^{TW} and H^{SW} are the parts of the RF magnetic field which are in phase and 90◦ out phase with the electric field respectively. The first term on the RHS of Equation 3-9 represents the active power flow, whereas the second term presents the reactive power flow, which are 90◦ out of phase with each other. The phase difference between the active and reactive power flows is significant as the reactive power is less efficient in providing power for field emission due to it being zero at the time when the field emission is maximum. Also, the active power flow and field emission power are in phase with each other. The real part of the complex Poynting vector $R\{S\}$ gives the active power flow and the imaginary component $I\{S\}$ gives the reactive power flow. The modified Poynting vector can then be defined as

$$\boldsymbol{S_C} = R\{S\} + g_c I\{S\}, \qquad (3\text{-}10)$$

where g_c is a weighting factor typically taken as 1/6 which can be used to describe the high gradient performance limit of metal structures in the presence of vacuum RF breakdown. The scaling law given in Equation 3-11 can be expressed in terms of the modified Poynting vector as [95]

$$\frac{S_C^3\, t_p}{BDR^{\frac{1}{5}}} = const. \qquad (3\text{-}11)$$

The study of RF breakdown is an area of active investigation and its application to gridded gun structures requires further investigation [99].

3.5.1.1 Gated electron gun operation below RF breakdown

To operate the RF gated gun, the applied total voltage between the cathode and grid should be lower than the breakdown threshold. Figure 3-5 shows the breakdown field as the function of the operating frequency

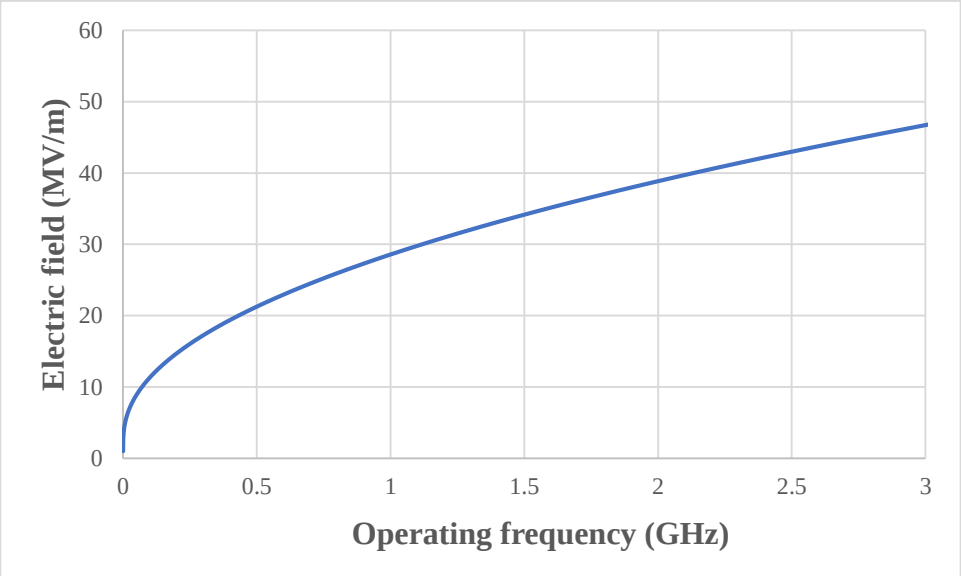

Figure 3-5. The Kilpatrick formula for conservatively calculating the breakdown potential for a given operating frequency.

Note for a given frequency the equation needs to be solved iteratively for E_k. Assuming the operating frequency of 1.5GHz, the breakdown electric field corresponds to 33 MV/m. Therefore, by defining the gap distance the maximum voltage applied can be estimated. This value was compared with the yielded measurements for the electric field obtained with the initial CST simulations. Figure 3-6 shows the electric field which corresponds to 10^5 which in our case is well below the breakdown value of 33 MV/m for the 1.5GHz operating frequency.

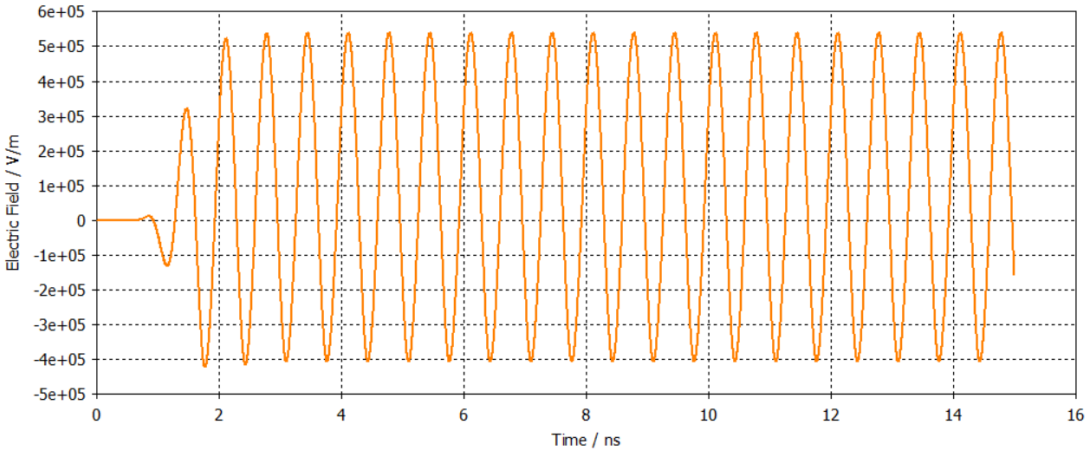

Figure 3-6. Electric field between the cathode and the grid for 0.16mm cathode-grid spacing.

Furthermore, some more initial simulations were made considering different gap distances and the effect on the collected current along with the CST model is shown in Figure 3-7. It can be seen that as the gap distance increases, the current decreases. Considering the above results for the breakdown potential, the desired current value and being a physically attainable distance when assembled, the chosen 0.16 mm gap distance satisfies all these requirements. From practical experience of gridded electron gun manufactures such as TMD Ltd a similar gap distance (0.13-0.17mm) was used. This was the closest distance the grid could be located to the hot thermionic emitter while still maintaining its geometry and shape even when undergoing thermal expansion due to the heat generated by the thermionic cathode. The acceptable tolerance between the cathode and grid distance is about 10% which corresponds to a distance of 0.01mm.

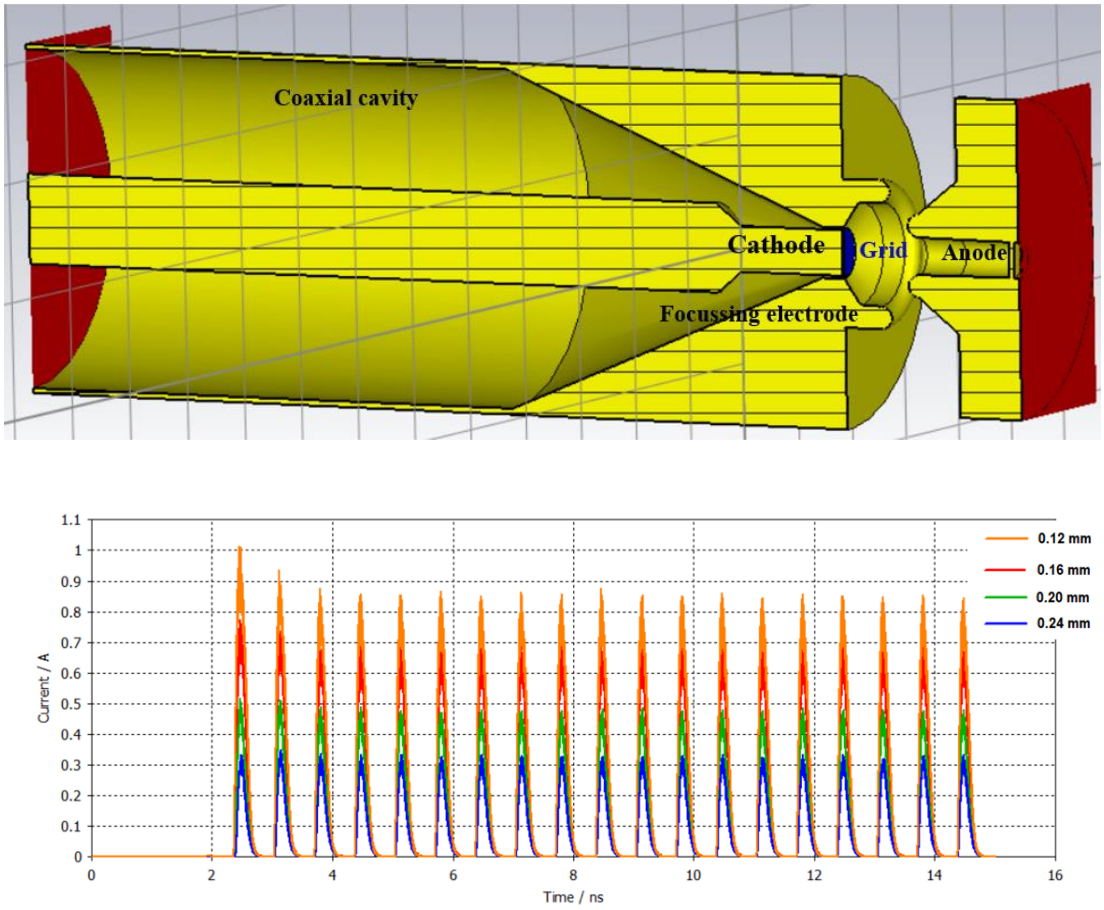

Figure 3-7. CST model of the electron gun geometry (top), collected current at the anode for different values of cathode-grid spacing (bottom).

3.6 Operation of the RF electron gun

The basic emission laws used to describe the generation and emission of electrons from the cathode, the electric/magnetic fields and trajectories of electron beams are given below. For the case when the electric field extracts all the thermally generated electrons then the emission current density is given by Richardson Dushman's law

$$J = AT^2 \exp(-\frac{e\Phi}{kT}) \qquad (3\text{-}12)$$

Where A is a Richardson's constant with theoretical value 120 $\mathrm{A/cm^2K^2}$, while Φ is the cathode work function and T is the temperature of the cathode. For space charge limited emission, the emission current density of electrons is given by Child-Langmuir's law

$$J = C\left(\frac{V^{3/2}}{d^2}\right) \qquad (3\text{-}13)$$

Where C is Child's constant with a value of 2.33×10^{-6} mA $\mathrm{V^{-3/2}}$, V is the potential difference between the cathode and the anode lying at a distance d. The electric field in the gun is first calculated using Poisson's equations derived from Maxwell's equations in the absence of the magnetic field. The electron trajectories are then calculated using the Lorentz force equations. The governing equations of the fields are the time-independent Maxwell's equations given by:

$$\nabla \cdot \mathrm{E} = \frac{\rho}{\varepsilon_0} \qquad (3\text{-}14)$$

where E is the electric field, ρ is the charge density and ε_0 is the permittivity of vacuum. The electron trajectories are determined by Lorentz force given by

$$F = \frac{dP}{dt} = q(E + v \times B) \qquad (3\text{-}15)$$

which simplify to (there is no magnetic field)

$$F = \frac{dP}{dt} = qE \tag{3-16}$$

The above equations form the basis of any theoretical calculations and simulation packages. The thermionic electron gun can operate in the space charge limited or temperature limited regimes. The space charge-limited current density follows Child's law, which is determined by the field strength at the emitter surface, while the current density at the temperature limited regime follows Richardson's law and it is mainly determined by the temperature at the emitter surface [60].

In more detail, gridded guns may be operated in three regimes, namely, saturation, amplification and cut-off, determined by the applied voltage [100]. In saturation, the current is limited by space charge and is governed by the Child-Langmuir equation. If the magnitude of the grid voltage is increased sufficiently, the gun will be brought into triode amplification mode, where the current is governed by

$$J = K_T \left(V_{gk} + \frac{V_{ak}}{\mu}\right)^{3/2} \tag{3-17}$$

where J is the current density produced from the cathode, K_t is a constant depending on the geometry of the triode, V_{gk} is the voltage between the cathode and the grid, $V_{ak}$is the voltage between the cathode and the anode, and μ is the triode amplification factor [100]. If the magnitude of the grid voltage is increased even more so the term inside the parenthesis is less or equal to zero

$$V_{gk} + \frac{V_{ak}}{\mu} \leq 0 \tag{3-18}$$

the gun will be driven in to cut off so that no electron will escape. If the gun is operated in pulsed mode, the voltage applied between the grid and the cathode will contain both a dc component (bias voltage) and a pulsed component (RF voltage). Normally, the bias and the RF voltage will be adjusted to drive the gun fully into cut-off or fully into saturation, producing a flattop beam pulse.

3.7 Validity of the Child Langmuir law for high RF voltage

To be RF gated, the electron gun should operate at the space charge limited regime to totally switch off the electron beam. Furthermore, when the electron gun is operating in the space charge regime there are certain benefits to the lifetime of the cathode.

The maximum steady-state current density that can be transported across a gap of spacing d and potential difference Vg is described by the one-dimensional Child-Langmuir (CL) law

$$J_{CL} = \frac{4\varepsilon_0}{9}\sqrt{\frac{2e}{m}}\frac{V_g^{3/2}}{d^2} \qquad (3\text{-}19)$$

When ($Vg > 0$) and where e and m are the charge and mass of the electron, respectively, and ε_0 is the free space permittivity.

However, when the frequency of the RF voltage increases and the pulse length of the electron beam is less than the transit time from the emitter to the grid, the classical Child-Langmuir law is not valid and there are certain corrections for calculating the current density. A classical short-pulse law has been derived which shows that the current density can be obtained by applying a correction factor to the equation which is given by [101]

$$\frac{J_{SCL}}{J_{CL}} = 2\frac{1-\sqrt{1-3X_{CL}^2/4}}{X_{CL}^3} \qquad (3\text{-}20)$$

where $X_{CL} = \frac{\tau}{T_{CL}} \leq 1$ is the normalized transit time and $T_{CL} = \frac{3d}{\sqrt{2eV_g/m}}$ is the gap transit time of the 1D classical Child-Langmuir law.

One thing that is needed to be investigated in our theoretical model is if in our case the classical law stands or the modified version need to be taken into account. Using the equations for τ and T_{CL} for the thermionic RF gated gun studied in this thesis, it was found that the transit time and the pulse length duration are ~60 ps and ~100 ps respectively. These calculations show that the transit time is less than the pulse length so the classical law is still valid.

3.8 Control voltage and emitted current

The grid voltage is a combination of the bias and the RF voltage. Figure 3-8 shows the typical waveforms of the control voltage and the emitted current. In the LINAC, the required electron beam current is relatively small and the beam energy is low.

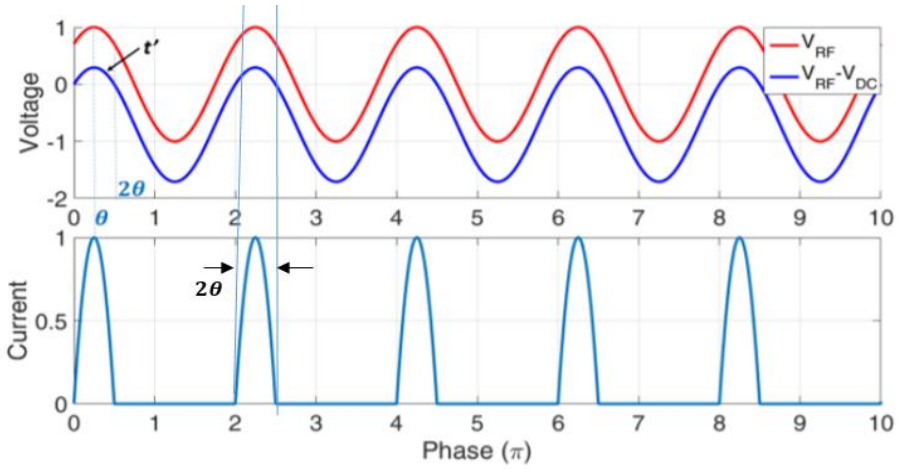

Figure 3-8. Time dependence of the grid voltage and the electron current.

One term that is important and is used for the derivation of the emitted current, bunch charge and bunch length is the conduction angle. Conduction angle θ is the angle at which the triode conducts. To determine the conduction angle, we need to determine the angles at which the triode starts and ceases conduction.

For a sinusoidal drive with amplitude U_{rf}, the conduction angle, 2θ, is given by

$$cos\theta = (-U_b + U_c)/U_{rf} \tag{3-21}$$

Where U_b is the dc bias voltage on the grid and U_c is the cut-off voltage. Under the assumption of a purely linear relation between I_a and U_g, the peak beam current is

$$I_p = G_{emit}\big(U_b + U_{rf} - U_c\big) = G_{emit}U_{rf}(1 - cos\theta) \tag{3-22}$$

Where G_{emit} is the emission coefficient and is defined as $G_{emit} = \frac{\Delta I_a}{\Delta U_g}$ which is in the range of 10-30 mA/V for practical cathodes [102]. Both emission coefficient and cut-off voltage depend on the cathode material and geometry. As the actual field in between the cathode and the grid is affected by the field penetration from the anode they are also depending on the anode voltage.

The time-averaged beam current is

$$I_0 = G_{emit}U_{rf}(sin\theta - \theta cos\theta)/\pi \tag{3-23}$$

and the first harmonic component which has a frequency of 1.5GHz in our case as determined by Fourier decomposition is

$$I_1 = G_{emit}U_{rf}(\theta - sin\theta cos\theta)/\pi \tag{3-24}$$

The RF voltage amplitude can be eliminated by substitution of equation 3-21 resulting in

$$I_0 = G_{emit}(-U_b + U_c)(tan\theta - \theta)/\pi \tag{3-25}$$

Equation 3-25 gives us the emitted current. The other two important parameters that need to be taken into account are the bunch charge and the bunch length. The charge per bunch Q can be expressed as

$$Q = \frac{2G_{emit}}{2\pi f} U_{rf}(sin\theta - \theta cos\theta) \qquad (3\text{-}26)$$

where

$$cos\theta = (-U_b + U_c)/U_{rf} \qquad (3\text{-}27)$$

denotes when the electrons are allowed to travel and f is the RF frequency. The bunch length of the emitted current is determined by θ given by equation (3-28)

$$\tau = \frac{\theta}{2\pi f}. \qquad (3\text{-}28)$$

Using the above equations, the parameters for our theoretical model were calculated and the relation between bunch charge, bunch length and applied voltages could be calculated. The bottom threshold of the emitted bunch length for a given bunch charge (33pC in our case) was obtained and shown in the next section.

3.9 The theoretical model of bunch length and bunch charge

The theoretical model provides the emission process of the electron beam, as well as the relationship between the electron bunch length, bunch charge, and the applied RF and bias voltages. Furthermore, this model is investigating the minimum possible bunch length obtained and the relation between its value and the bunch charge which will be compared with the simulation results in chapter 5.

In developing this theoretical model, some simplifications were made. These include, ignoring the space charge effect and considering the electric field between the cathode and the grid as a uniform distribution. Under these circumstances, the electrons will travel to the grid under the applied electric field. The electron's longitudinal position follows

$$\ddot{L}(t) = \frac{e}{m}\frac{U_{grid}}{d} \qquad (3\text{-}29)$$

These electrons may experience both accelerating and decelerating electric fields. The electrons that travel during the positive half cycles of the microwave input voltage U_{grid}, travel faster than the electrons that passed the gap when $U_{grid} = 0$. The electrons that travel during the negative half cycles of the voltage U_{grid}, travel slower than the electrons that passed the gap when $U_{grid} = 0$. Only the electrons emitted before time t' are able to pass through the grid and escape the cathode grid region to the anode. If these electrons don't make it, they will be reflected back to the emitter. The time t' is the time that determines the bunch duration from the emitter, and is defined as

$$L(2\tau) - L(t') = d \qquad (3\text{-}30)$$

Ideally t' needs to be close to 2τ to reduce the beam current lost which means the gap distance d needs to be as small as possible. As it has already be seen there are both physical limits and restraints on the voltage between the cathode and the grid. The first arose due to physical limitations on how close it is possible to place the grid in front of the cathode and the second due to the RF breakdown.

The theoretical model developed in this section provides the emission process of the electron beam, and the relationship between the different required parameters and the grid voltage. The bottom threshold of the emitted bunch length for a given bunch charge was obtained by solving equations (3-21), (3-22), (3-26), (3-28) and (3-30) to obtain the values for each of the parameters.

For these simulations a gap distance of 0.16 mm was used, an emission coefficient G_{emit} of 18 mA/V, and a limit of $U_{rf} + |U_{bias}|$ = 600V was chosen. The relationship between the bunch charge and the bunch length is given for different conduction angles in Figure 3-10. With these values, the bottom threshold of the bunch length possibly attainable has been established. Two different operating frequencies were used in these calculations to investigate the effect on the bunch charge/bunch length. The results for operating frequencies of 1.5 GHz and 3GHz are shown in Figure 3-10 top and bottom respectively. With a bunch charge of 33.3 pC which is the specific requirement for the LINAC at 1.5 GHz, the smallest bunch length corresponds to about 68 ps when the conduction angle is θ = 40°. For the 3GHz case a bunch charge of 16.7 pC with a bunch length of about 23 ps can be achieved when θ = 45°.

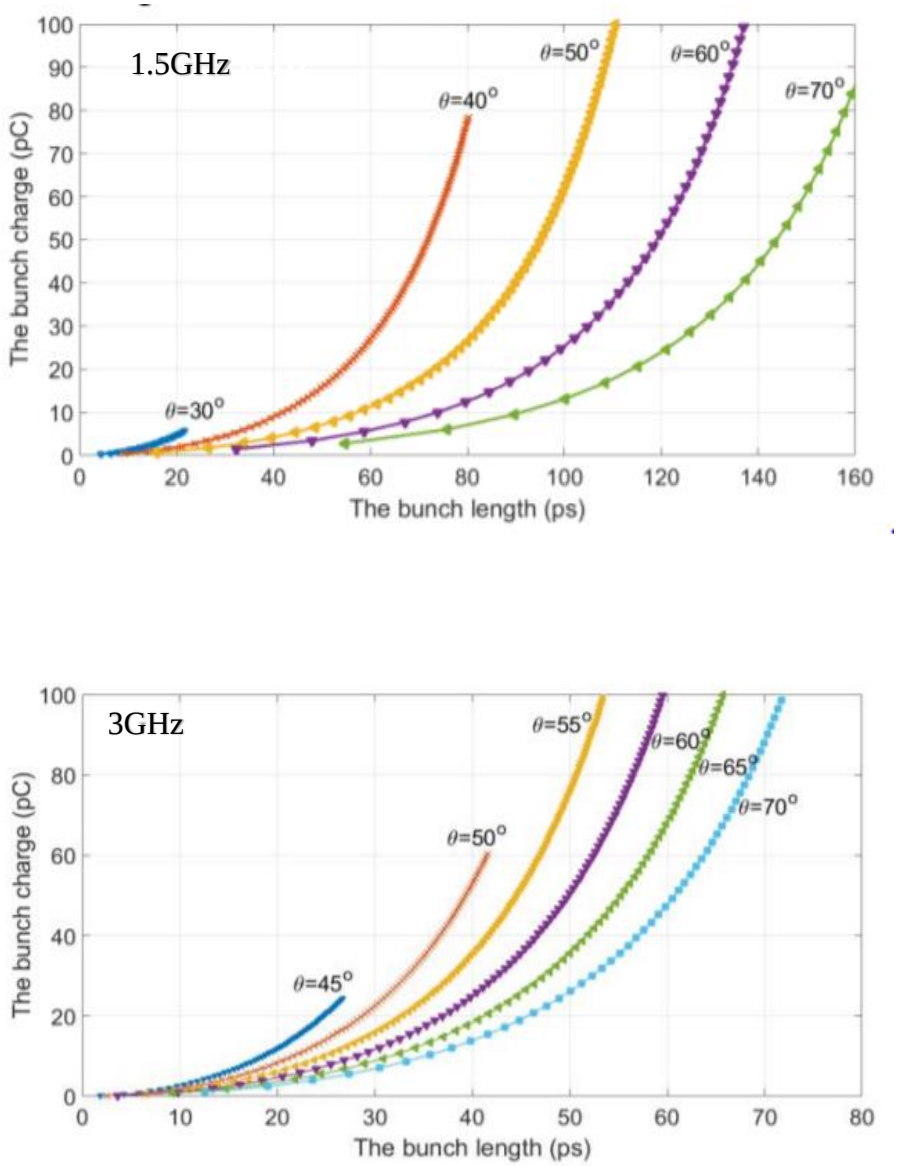

Figure 3-9. Relationship between bunch charge and bunch length for 1.5GHz (top) and 3GHz (bottom) operating frequency.

Summary

This chapter aimed to develop a theoretical model for the gridded thermionic electron gun based on the initial electron beam parameters of the LINAC. The configuration of the electron gun with RF gating and the coaxial cavity for this configuration was discussed and the waveform of the control voltage and the emitted current was obtained along with other important parameters like bunch charge, bunch length. The minimum bunch length for the required value of bunch charge was established from this theoretical model and was found to be 68ps. Operating at higher frequency showed that the minimum bunch length had a lower value of 23ps.

Chapter 4

4 Design and Simulation of an Electron Gun in 2D

The electron gun studied in this thesis was a Pierce electron gun and was designed using two different simulation programs, TRAK for the static, DC electron gun, and MAGIC for the RF electron gun. In the previous chapter, a theoretical model of this electron gun was developed. However, in this analysis effects like space charge, thermal emission distribution and beam dynamics between the grid and anode were not taken into account for simplification purposes. The design of a Pierce electron gun using Vaughan synthesis and the TRAK simulation software was developed. This design was the basis for the RF gun described in the chapter 5.

4.1 Pierce electron gun

Electrons are emitted by the cathode and get accelerated across the gap between the cathode and the anode by applying a potential. At high current densities, space charge is building up distorting the equipotential lines resulting in the beam spreading out. This problem can be avoided by adding an electrode at the edge of the beam. The angle at which the electrode needs to be placed to counteract the distortion effect is derived below by firstly make the following assumptions.

1) The magnetic field effect and the thermal velocities of the traversing electrons are neglected
2) Only the electrostatic forces are considered.

Under these assumptions, the electron velocity (v_e) at any point is specified by a potential φ and at $\varphi = 0$, $v_e = 0$. The charge density (J/v_e) is continuous where J is the current density which is constant throughout the flow and v_e is the electron velocity as specified by φ. The one-dimensional Poisson's equation for the region between the electrodes is given by equation

$$\frac{d^2\varphi}{dx^2} = \frac{-Ze.n(x)}{\varepsilon_0} \tag{4-1}$$

where in a steady-state the current density $j_0 = Ze.n(x).v_x(x)$ is the same at all positions in the gap. The particle density as a function of the position is given as

$$n(x) = \frac{\frac{J}{Ze}}{v_x(x)} \tag{4-2}$$

Considering the electrostatic potential to be zero at the particle source the particle velocity is

$$\frac{m_0 v_x^2}{2} = Z_e \phi \qquad (4\text{-}3)$$

Rearranging the two above equations (4-2) and (4-3) and substituting into (4-1) Poisson's equation can be rewritten as

$$\frac{d^2\varphi}{dx^2} = -\frac{J}{\varepsilon_0\sqrt{2.Z_e.\varphi/m_0}} \qquad (4\text{-}4)$$

Equation (4-4) needs to be solved with the appropriate boundary conditions. Firstly, conservation of energy and particle flux is used to express the beam density as a function of the field quantity, φ and secondly Equation (4-4) can be more efficiently rewritten by introducing the dimensionless variables $\xi = x/d$ and $\Phi = \phi/V_0$

Equation (4-4) becomes

$$\frac{d^2\Phi}{d\xi^2} = \frac{\beta}{\sqrt{\Phi}} \qquad (4\text{-}5)$$

Where

$$\beta = \frac{J.d^2}{\varepsilon_0.V_0\sqrt{2.Z_e.V_0/m_0}} \qquad (4\text{-}6)$$

Equation (4-5) is solved by multiplying both sides by $2\Phi'$ where $\Phi' = \frac{d\Phi}{d\xi}$

$$2.\Phi'.\Phi'' = \frac{2.\beta.\Phi'}{\sqrt{\Phi}} \qquad (4\text{-}7)$$

The left-hand side is an exact differential of $(\Phi')^2$ Equation 4-7 is then integrated both sides for the regime, x=0 (the source position), to x=x position.

$$[\Phi'(\xi)]^2 = 4.\beta.\sqrt{\Phi(\xi)} \qquad (4\text{-}8)$$

Equation 4-8 can be rewritten as

$$\frac{d\Phi}{\Phi^{1/4}} = \sqrt{4.\beta}.d\xi \qquad (4\text{-}9)$$

Integrating both sides of equation 4-8

$$\Phi^{3/4} = \left(\frac{3}{4}\right).\sqrt{4.\beta}.\xi \qquad (4\text{-}10)$$

At the boundary condition $\Phi = 1$ implies $\beta = 4/9$. Substituting β from above and solving for the current density j_0 the space charge is calculated from the well-known Child-Langmuir law for space charge limited extraction

$$j_0 = \frac{4.\varepsilon_0}{9}.\sqrt{\frac{2.Z_e}{m_0}}.\frac{V_0^{3/2}}{d^2} \qquad (4\text{-}11)$$

The value of V_0 is obtained as

$$V_0 = \left[\frac{9.j_0}{4.\varepsilon_0}.\sqrt{\frac{m_0}{2.Z_e}}\right]^{2/3}.d^{4/3} \qquad (4\text{-}12)$$

For space-charge-limited flow, the variation of electrostatic potential with the position is given as

$$\varphi(x) = V_0.(\frac{x}{d})^{4/3} \qquad (4\text{-}13)$$

Where V_0 is applied voltage, d is the gap between cathode to anode and x is the variable position between cathode and anode.

Substituting V_0 from Equation (4-12) into (4-13), the ultimate expression of the space charge potential distribution is written as

$$\varphi(x,0) = \left[-\frac{9.j_0}{4.\varepsilon_0}.\sqrt{\frac{m_0}{2.Z_e}}\right]^{2/3}.x^{4/3} \qquad (4\text{-}14)$$

The potential distribution as given by

$$\varphi(x,y) = \left[-\frac{9.j_0}{4.\varepsilon_0}.\sqrt{\frac{m_0}{2.Z_e}}\right]^{2/3}.Re(x+jy)^{4/3} \qquad (4\text{-}15)$$

It satisfies the Laplace equation $\nabla^2\varphi$, outside the beam. Reducing the equation (A) at y = 0, zero electric field or zero potential gradients is obtained normal to the beam edge. It implies that $\frac{\partial\varphi}{\partial y} = 0$ at y = 0.

According to Equation (4-15), equipotential surfaces are observed to be those for which $\theta = tan^{-1}(y/x)$

$$(x^2+y^2)^{\frac{2}{3}}.cos\left(\frac{4}{3}.\theta\right) = \frac{V}{\left[\frac{9.j_0}{4.\varepsilon_0}.\sqrt{\frac{m_0}{2.Z_e}}\right]^{2/3}} \qquad (4\text{-}16)$$

The zero potential V = 0 is a plane, whose intersection with y-x plane is given by $y = x\ \tan 67.5^{\circ}$. The angle of 67.5º arises from the power 4/3 in equation (4-14) and is called Pierce angle hence the name of the Pierce electron gun.

4.2 Modelling of a Pierce electron gun

A Pierce electron gun is divided into three regions as shown in Figure 4-1. The first region is the cathode which is spherical in shape and the focus electrode which produces equipotential surfaces to match the cathode's curvature. In region 2, the equipotential surfaces may get distorted due to the anode hole so a divergent electrostatic lens exists to counteract this effect. In region 3, the electrons are only

under the influence of space charge forces and some form of magnetic focusing is sometimes required. Using Vaughan synthesis [103], the design of a Pierce type thermionic cathode electron gun is described in the next section.

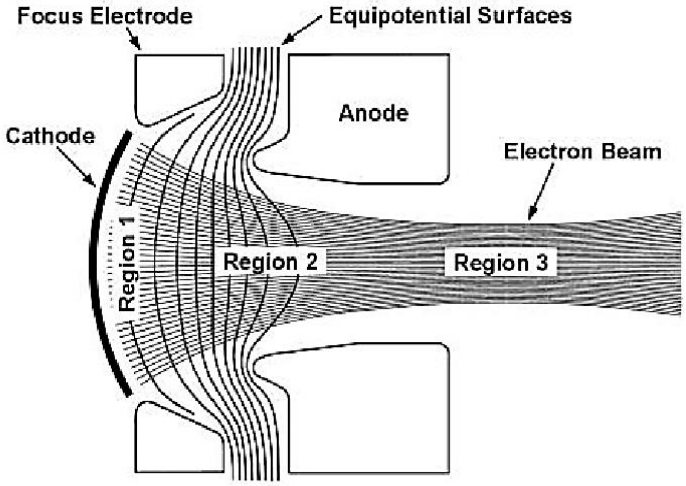

Figure 4-1. Overview of a Pierce gun including the three regions of interest [104].

4.2.1 Vaughan synthesis, input and output parameters

The design of Pierce guns has been based on graphical methods and on the designer's intuition in the past, however this approach is not reliable and a more robust method is needed. Vaughan synthesis is a procedure that allows the designer to specify the desired beam and calculate the configuration needed to produce it.

The primary requirements for the gun design, known as input parameters are the beam voltage (V), the current (I), the beam diameter which refers to the waist diameter ($2r_w$) and a fourth parameter can be assigned and this is the current density (J_c). These four parameters are not arbitrarily chosen. They are all related to the beam quality and the lifetime of the cathode. These four quantities V, I, r_w and J_c, define a unique Pierce gun.

The outputs for a basic gun design include the convergence half angle (θ), the cathode disc (r_c) and spherical radii (R_c), the anode-cathode spacing (z_{ac}) and the radius of the anode aperture (r_a). A schematic representation of both the input and output parameters is shown in Figure 4-2.

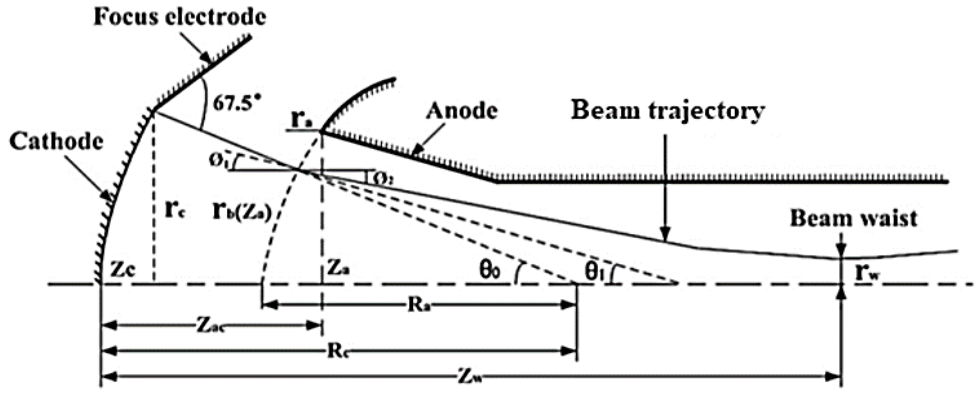

Figure 4-2. Schematic representation including the input and output parameters of a Pierce electron gun [105].

The initial geometry of our gun was generated based on the Vaughan synthesis with the four input parameters. The primary beam parameters for the particle accelerator which dictates the design of a Pierce type thermionic cathode electron gun were specified as follows: Beam voltage (25kV), current (502mA), beam waist radius (0.5mm) and current density (1A/cm^2). These initial parameters were chosen for an ideally low emittance beam and a longer lifetime for the cathode by choosing a moderate current density. For higher electron emission current density, the higher the temperature of operation needs to be and the shorter the lifetime of the cathode. To ensure a cathode lifetime is over the lifetime of the other components in the linac, an electron emission current density of 1 A/cm^2 was chosen.

After having specified the input parameters for the electron gun, the output parameters were obtained using the Vaughan synthesis. The input and output values are summarised in Table 4-1 and Table 4-2 respectively.

Parameter	***Value***
$Cathode\ Voltage$	$25000\ V$
$Cathode\ current$	$500\ mA$
$Cathode\ current\ density$	$1\ A/cm^2$
$Beam\ waist\ radius$	$0.5\ mm$

Table 4-1. Input parameters for the design of the Pierce electron gun.

Design Parameters	***Synthesised data***
$Beam\ Perveance\ (\mu P)$	$0.16\ \mu pervs$
$Half\ beam\ cone\ angle\ \theta$	12.0^o
$Cathode\ spherical\ radius\ R_c$	$20.1\ mm$
$Anode\ spherical\ radius\ R_a$	$9.8\ mm$
$Cathode-anode\ distance\ (Z_{ac})$	$10.2\ mm$
$Axis\ location\ of\ beam\ waist\ (Z_w)$	$39.1\ mm$

Table 4-2. Output parameters determined with Vaughan synthesis.

4.2.2 Emittance

Emittance is an important parameter for the quality of the beam as explained in Chapter 2. When designing the electron gun, one of the requirements is as small emittance as possible. Some initial work was carried out before deciding the values of the parameters for a lower emittance beam. Several sources contribute to the overall beam emittance. This contribution comes from the finite cathode temperature, the magnetic field on the cathode, the roughness of the cathode and the emittance of the grid wire [60]. The equations giving the emittance due to the different sources are given below and summarised in Table 4-3.

For the finite cathode temperature equation, the emittance is given by equation (4-17)

$$\varepsilon_{n,T} = (\frac{1}{2})R_c(\frac{k_b T_c}{mc^2})^{1/2} \quad (4\text{-}17)$$

where R_c is the radius of the cathode and T_c is the cathode temperature.

The emittance due to magnetic field is given by

$$\varepsilon_{n,B} = qB_0R_c^2/2mc^2 \quad (4\text{-}18)$$

where $B_0 = 0.5G$ is the assumed magnetic field on the cathode from the Earth.

The emittance due to roughness on the cathode is given by

$$\varepsilon_{n,R} = \pi h/(2l)R_c(\frac{qE_s h}{2mc^2})^{1/2} \quad (4\text{-}19)$$

where h is the amplitude of surface roughness and l is the period of the roughness. Some typical values for h and l are 1 μm and 20 μm [60]. Finally, the emittance from the grid wire is given by

$$\varepsilon_{n,grid} \approx R_c\langle\beta_x\rangle \approx \frac{2\mu_1(a)}{3}\left(\frac{a}{z_G}\right) R_b \frac{\left|\Phi_G - \left(\frac{z_G}{z_A}\right)\Phi_A\right|}{\left(\frac{z_G}{z_A}\right)^{1/2}\Phi_A^{1/2}} \qquad (4\text{-}20)$$

Where $\langle\beta_x\rangle$ is the averaged normalized electron velocity and $\mu_1(a)$ is the shielding parameter due to one wire. The potential on the grid relative to the cathode is denoted by $\Phi_G(t)$ and consists of a dc bias and rf component while the anode potential is $\Phi_A(t)$ The grid wires form an infinite array located at $z = z_G$. The grounded cathode is located at $z = 0$ and the anode at $z = z_A$.

The total emittance is the sum of the emittance risen by all of the sources given by

$$\varepsilon_{total} = \sqrt{\varepsilon_{n,r}^2 + \varepsilon_{n,B}^2 + \varepsilon_{n,R}^2 + \varepsilon_{n,grid}^2} \qquad (4\text{-}21)$$

The relation between the emitter radius, the cathode voltage and the emittance was investigated to establish the values used for the design of our electron gun. The results are shown in Figure 4-3. Figure 4-3 (top) shows the relation between the cathode radius and the emittance. The bigger the cathode radius the higher the emittance which implies a smaller cathode radius with an adequate current density is preferred. Another parameter that was investigated was the cathode voltage and the effect on the emittance. Figure 4-3 (bottom) shows that the beam voltage does not increase emittance significantly. In this case, a slightly higher beam voltage of 25kV was chosen to have larger energy entering the acceleration structure.

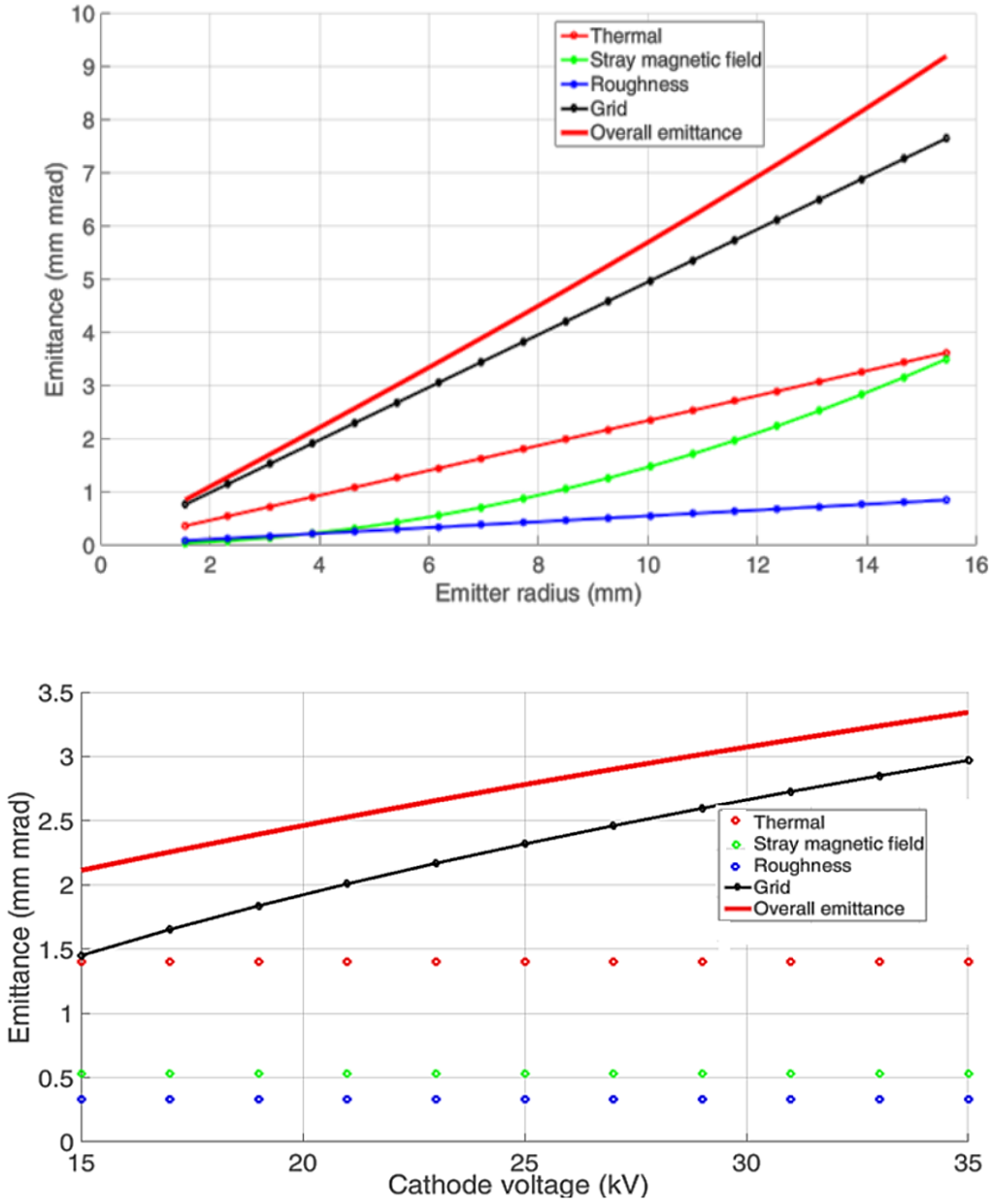

Figure 4-3. Effect of the emitter radius on the emittance (top) and the effect of the cathode voltage on the emittance (bottom).

4.3 Modelling using TRAK

4.3.1 Finite Element Method

TRAK 8, Field Precision LLC is a program for charged-particle optics with a variety of applications. These applications include electron and ion guns, particle accelerators, ion sources and electron guns for microwave sources. TRAK operates using the Finite Element Method (FEM) which has been applied to model the electron trajectories from the Pierce type electron gun. It has the advantage of ease of treating boundary conditions and an efficient method of selecting the mesh size. First the potential distribution is calculated by solving Poisson's equation in an axially-symmetric case in cylindrical co-ordinates given by equation (4-22)

$$\frac{\partial^2 V}{\partial r^2} + \frac{1}{r}\frac{\partial V}{\partial r} + \frac{\partial^2 V}{\partial Z^2} = -\frac{\rho}{\varepsilon_0} \qquad (4\text{-}22)$$

where V is the electric potential, ρ is the space charge, ε_0 is the dielectric constant of free space, r is the radial coordinate and z the axial coordinate. Secondly the electron trajectories are computed by solving the momentum equations of the electrons, equation (4-23 and 4-24).

$$\frac{\partial^2 r}{\partial t^2} = -\eta . \frac{\partial V}{\partial r} \qquad (4\text{-}23)$$

$$\frac{\partial^2 Z}{\partial t^2} = -\eta . \frac{\partial V}{\partial Z} \qquad (4\text{-}24)$$

where η is –e/m, e is the charge of the electron and m is the mass of the electron.

These two parts are not independent as the trajectory influences the potential distribution through the space charge, and this potential distribution directly influences the trajectory. Figure 4-4 is a block diagram of computations carried out in TRAK.

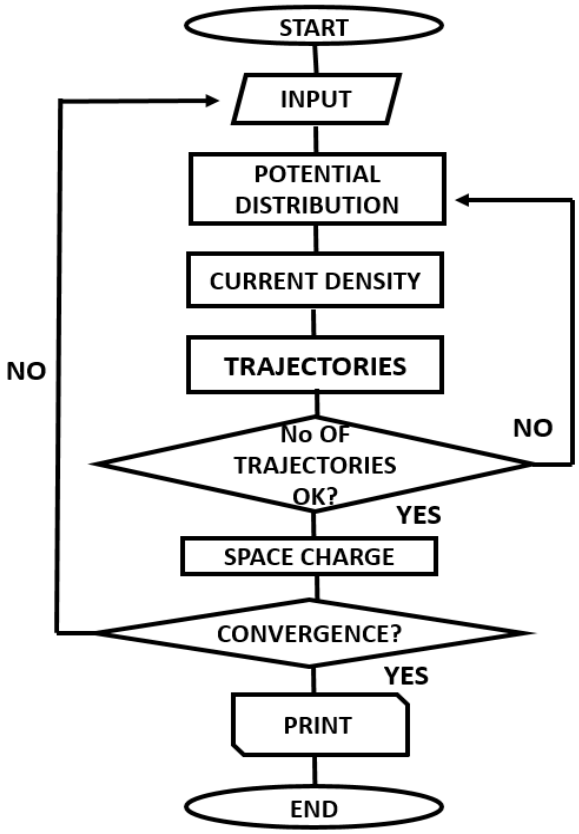

Figure 4-4. Block diagram of FEM computations.

The first step in a finite-element solution is to divide the solution volume into small pieces or cells called elements. This process produces the so-called mesh. There are two steps in the mesh generation procedure. These involve firstly, fill the solution cross-section with a set of triangles of appropriate sizes and secondly shift nodes so that the element facets lie close to material boundaries as shown in Figure 4-5. In the next section the TRAK process is analysed and the simulation results are presented.

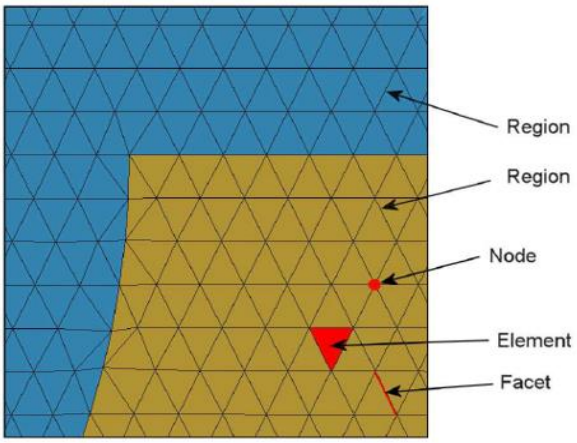

Figure 4-5. Definition of terms in a triangular formed mesh.

4.3.2 Simulation using TRAK (E-static electron gun)

A Pierce-type electron gun is appropriate for producing an electron beam with constant current density for a linear beam. The electron gun consists of an electron emitter, a focus electrode held at cathode potential and a grounded anode with shaped electrodes to modify the equipotential profile due to the effect of the anode aperture. This structure of an electron gun was simulated using TRAK along with the Mesh and the Estat features. Estat carries out electrostatic calculations and the potential is determined at the nodes and the material characteristics are assigned to the triangle volumes. Certain orders must be kept when using TRAK. First the Mesh feature is used to create the gun design including all the input and calculated output parameters. The input and output parameters can be found in Table 4-1 and Table 4-2 respectively.

Taking into account our parameters, the electron gun geometry is divided into 4 regions as shown in Figure 4-6 (top). These are the cathode, the anode, the focusing electrode and the vacuum. The outline of the Mesh is shown along with information about the filled (F) and unfilled regions (U). Once the initial geometry was created, Estat was used to obtain information about the distribution of the equipotential line in the different regions of the electron gun. The profile of the electric field is shown in Figure 4-6 (bottom). The beam waist position and beam waist radius in the electron gun are also presented. Because of the anode aperture, the equipotential surfaces are bent into the anode aperture and make the beam diverge in region 2. Furthermore, there is no electric field in drifting region 3 and the electron motion is then affected by space charge. The laminarity of the electron gun indicates the electron beam quality in the focusing electromagnetic field and the defocusing electromagnetic field.

Taking a first look at the results, the first observation made is that some of the electron beam is blocked by the anode. This is an indication that the geometry of our electron gun needs to go through the process of optimisation. When optimising the electron gun, the radius of the focusing electrode, the distance between the anode and the cathode and the emitter radius should be concerned in the optimisation of the electron gun. The optimisation process is shown in the next section.

It needs to be mentioned that the Pierce-type gun is normally with a curved emitter surface as shown in Figure 4-6. The reason for this is to achieve a large beam compression ratio. However, it is not a critical parameter when it comes to the RF gun since a large beam radius is acceptable. The process of the optimisation for this purpose used a flat surface and furthermore, the flat emitter surface also helped to save the simulation time since a less dense mesh grid could be used to represent a flat surface as compared to a curved cathode surface.

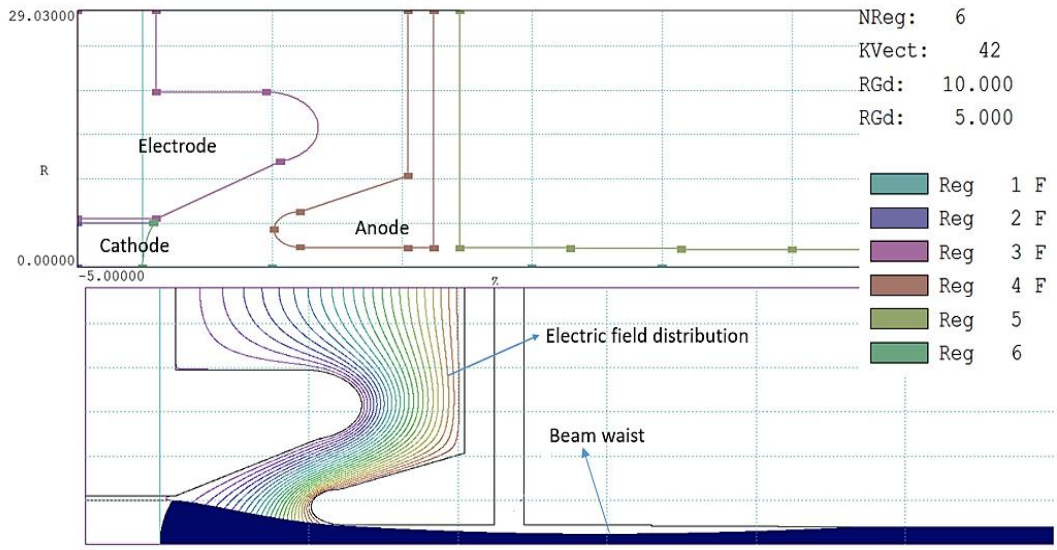

Figure 4-6. Regions of the electron gun using the feature Mesh (top) and Estat for the electric field distribution (bottom).

4.3.3 Optimisation of the electron gun from the initial geometry

The initial geometry obtained with Vaughan synthesis was used as the starting point for further optimisation to get more accurate simulation results and to further improve the electron beam quality, including good laminarity and a small emittance. Moreover, there are requirements for the total emitted current (I) and the beam waist radius (r_w), values that need to be achieved through the process of optimisation. Beam waist radius is the measure of how much the beam confines, that is the minimum beam radius. The required values for these parameters are given in Table 4-3.

$Parameter$	$Required\ value$
$Total\ emitted\ current\ (I)$	$\sim 1\ A$
$Beam\ waist\ radius\ (r_w)$	$\sim 1 - 1.5\ mm$

Table 4-3. Required parameters for the optimised electron gun.

The emitter surface used in these simulations was a readily available, commercial gridded cathode. The model chosen was the NJK2221A gridded thermionic cathode from Japan Radio Co. Ltd. It has a flat emission surface with a radius of 4.0 mm, and a grid distance of 0.16 mm. The cathode specifications and the outline are given in Table 4-4 and Figure 4-7 respectively. The flat emitter surface of this particular cathode helped to save the simulation time since a less dense mesh grid could be used to represent a flat surface as compared to a curved cathode surface.

Cathode type	*Ir coated dispenser cathode*
Cathode diameter	$8mm$
Current density	$10\ A/cm^2$
Heater voltage	$6.7V$
Heater current	$1.6A$

Table 4-4. Specifications of the emitter surface used in the simulations.

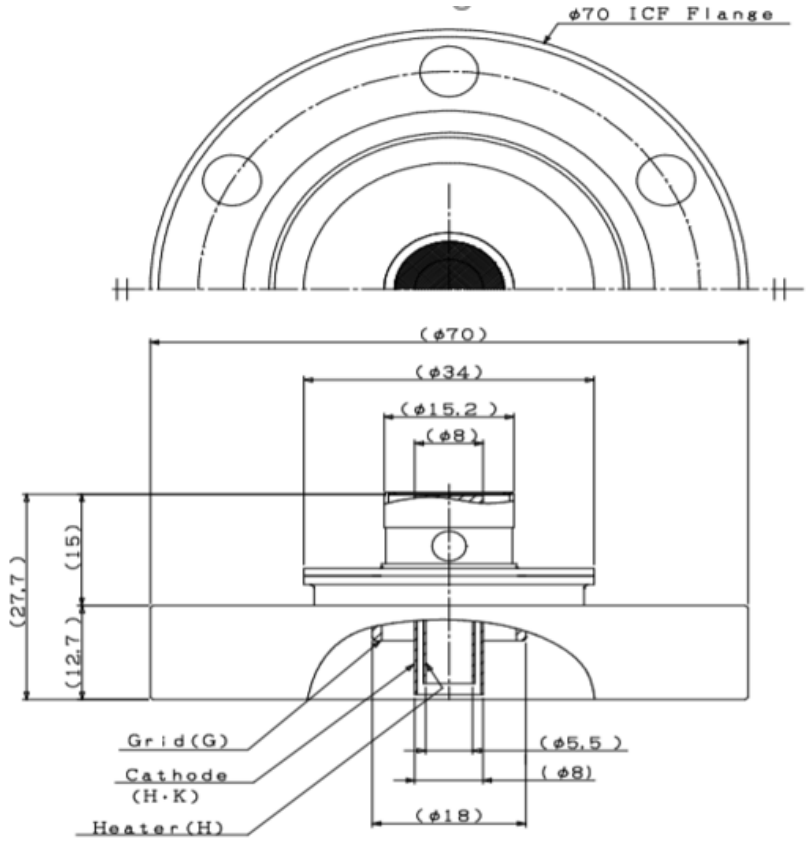

Figure 4-7. Schematics representation of the NJK2221A gridded thermionic cathode, dimensions are expressed in mm.

The initial geometry of the electron gun was obtained using TRAK and optimisation was carried out by investigating parameters like the cathode radius, the cathode-anode

gap distance and the focusing electrode angle and how these parameters affect the beam current and the beam waist radius. Figure 4-8, 4-9 and 4-10 show the variation of the emitted current and the beam waist radius with the cathode radius, cathode-anode gap distance and the focusing electrode angle respectively.

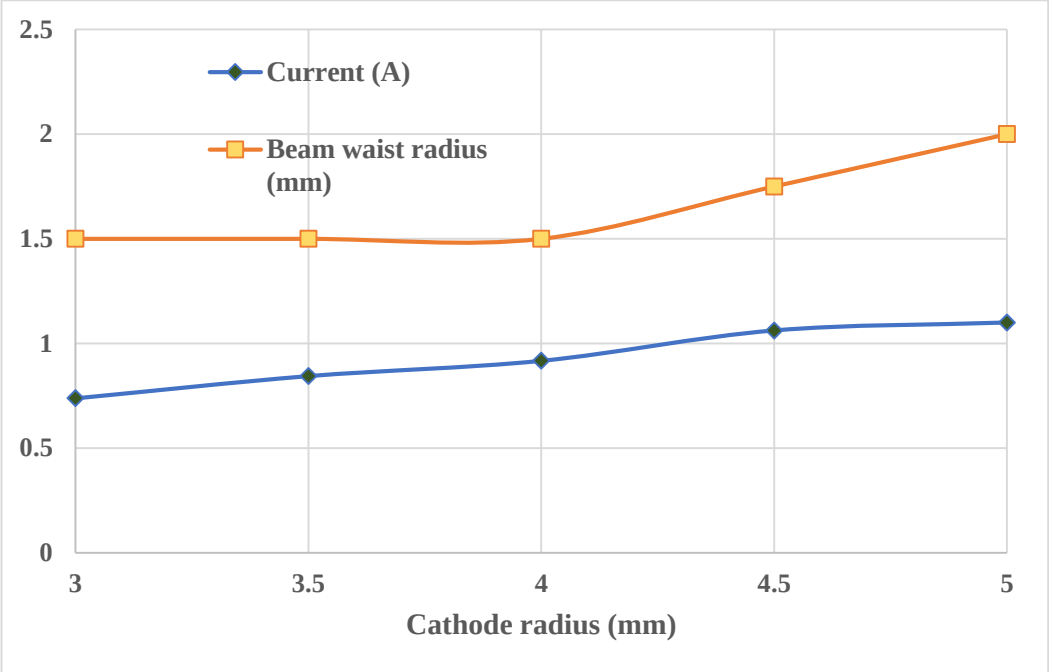

Figure 4-8. Resultant values for the total emitted current and beam waist radius for different cathode radiuses.

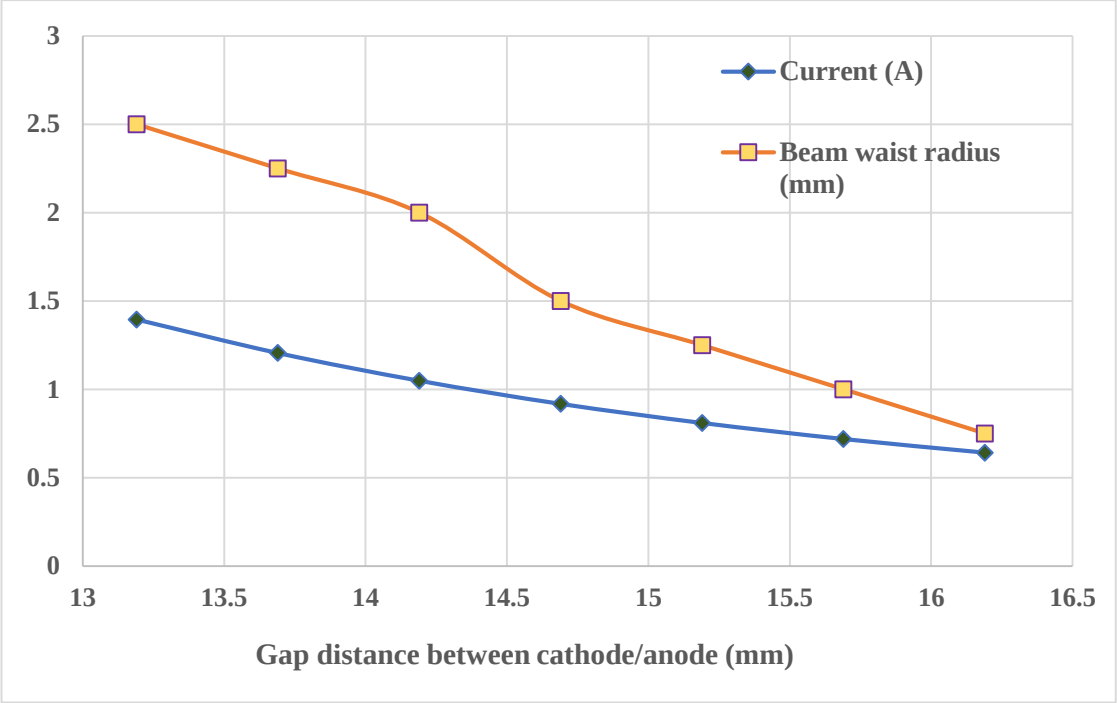

Figure 4-9. Resultant values for the total emitted current and beam waist radius for different gap distances between cathode/anode.

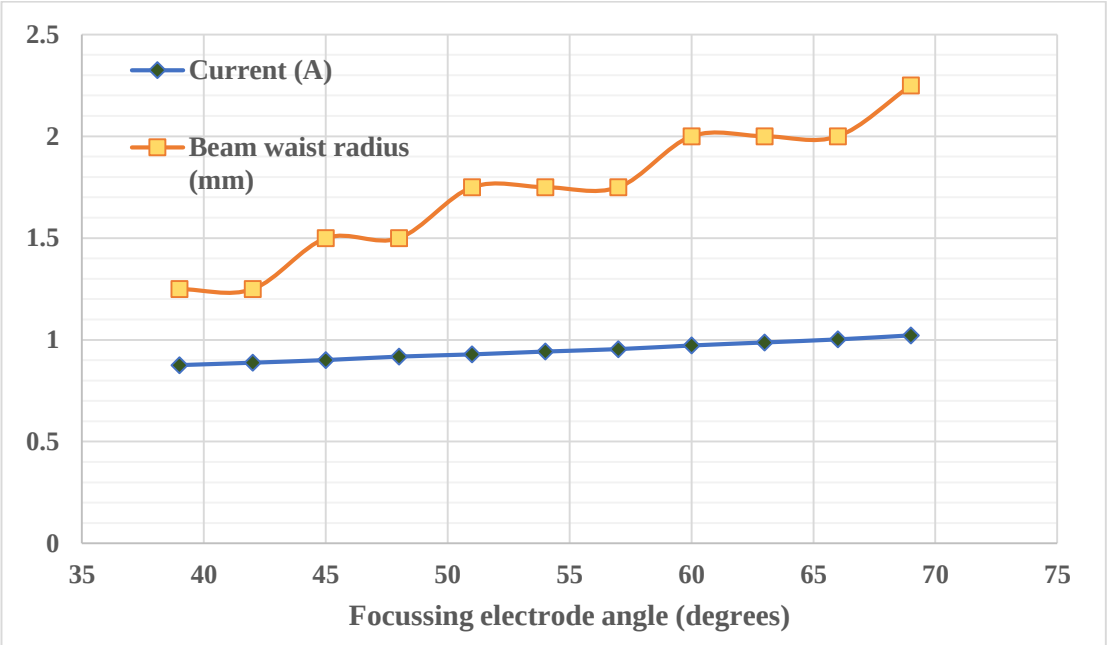

Figure 4-10. Resultant values for the total emitted current and beam waist radius for different focusing electrode angles.

From figures, 4-8, 4-9, 4-10, it is clear that when the beam current is increasing, the beam waist radius is increasing too, potentially making the beam focussing harder. In Figure 4-8 it can be seen that the cathode length is directly related to the beam current something which is expected from the Child-Langmuir law. On the other side, in Figure 4-9 it is shown that as the gap distance between the cathode and the anode is increasing, the emitted current decreases. This is due to the change in the electric field as the gap distance changed. More specifically, as the distance increases the electric field strength decreases. The beam waist radius follows a similar trend due to space charge forces decreasing. The electric field for different cathode-anode distances is shown in Figure 4-11.

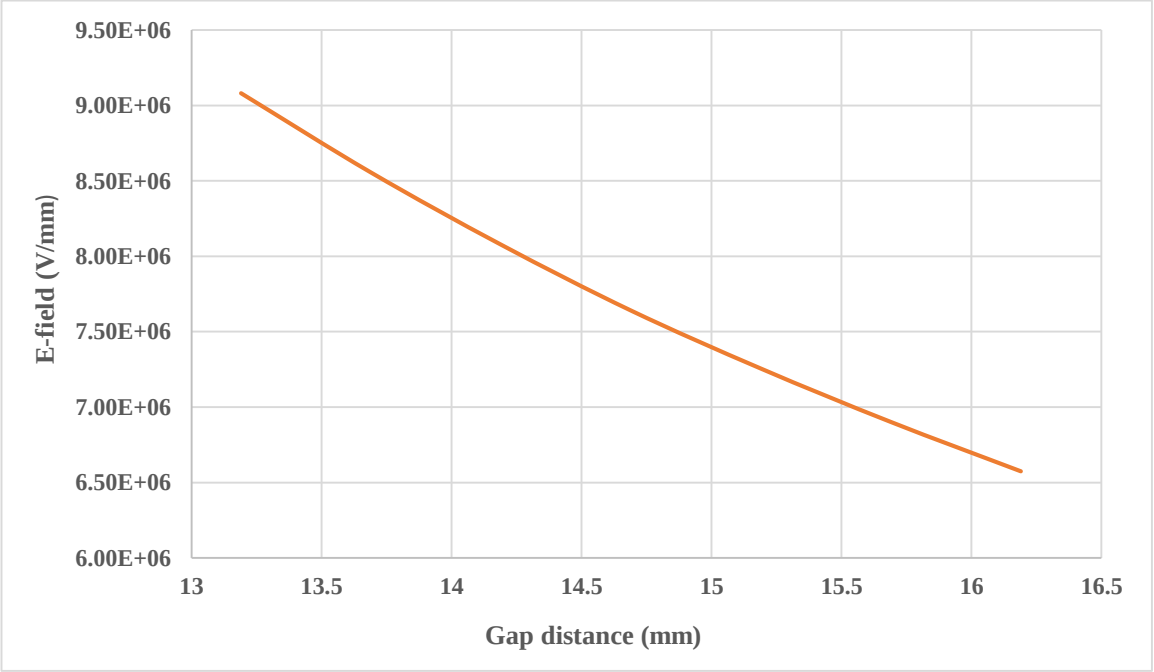

Figure 4-11. The simulated electric field as a function of gap distance.

Similarly, to the gap distance, the focusing electrode angle has a direct effect on the modification of the electric field thus on the beam waist radius as seen in Figure 4-10. The last parameter examined, wasn't involved in the optimisation of the electron gun's geometry but it examined the effect of the cathode temperature on the emitted current. As it has been mentioned in chapter 3 operating in the space charge regime has numerous benefits. One of them is that the cathode temperature has no effect on the emission and so the temperature across the cathode need no longer be uniform in order to obtain uniform emission. Figure 4-12 shows the variation of the current with the cathode temperature which shows only a slight difference in the emitted current as the temperature increases.

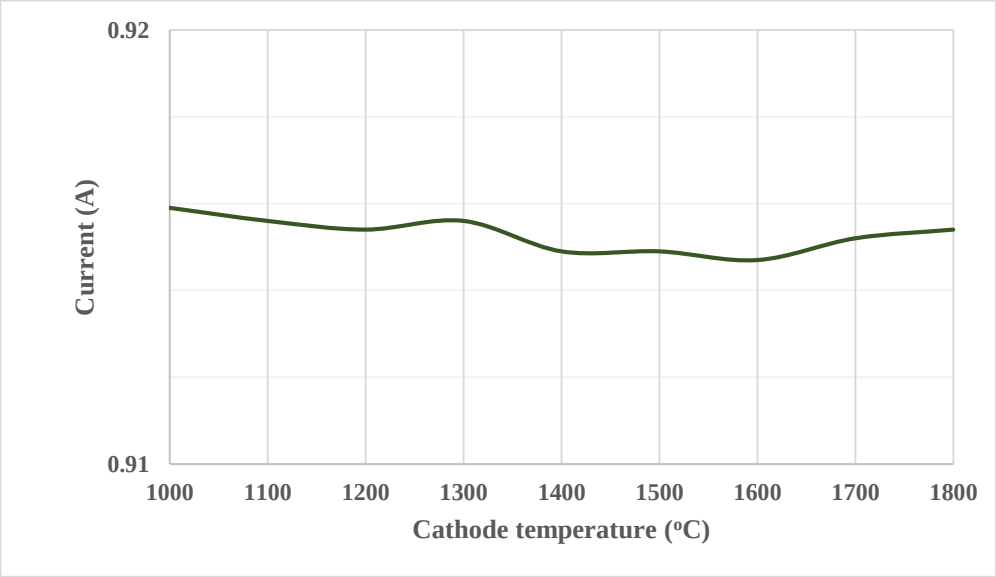

Figure 4-12. Values of current for different cathode temperatures.

The beam trajectory of the optimised geometry simulated is shown in Figure 4-13. The geometry chosen was corresponding to values of 1 A for the emitted current, and 1.5 mm for the beam waist radius. These values are in accordance with the values in Table 4-4.

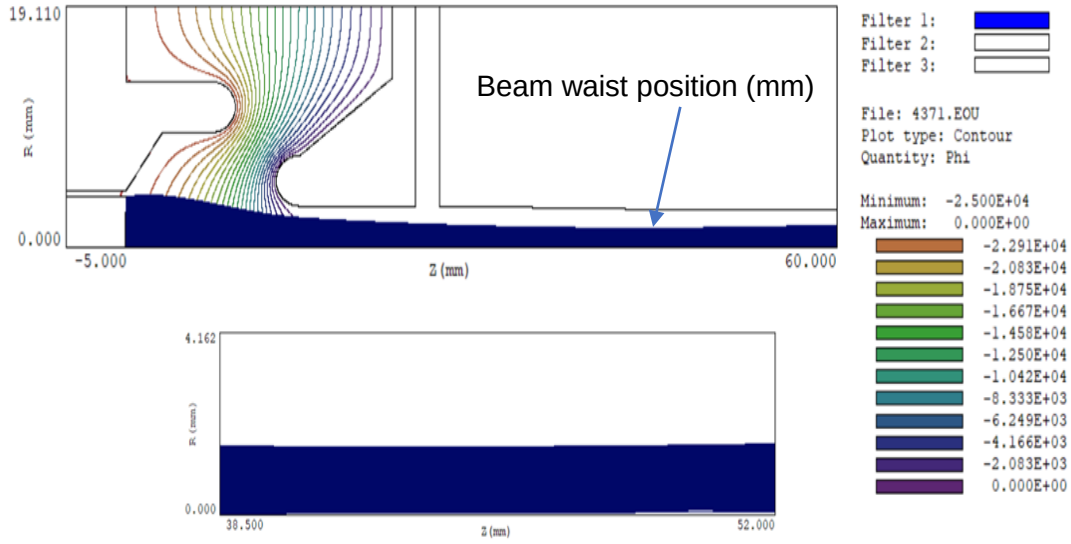

Figure 4-13. Optimised geometry to achieve the desired values for the beam parameters.

The beam trajectories from the TRAK simulations were exported for post-processing and calculation of the emittance. The root mean square (RMS) normalised transverse beam emittance defined by $\varepsilon_{x,RMS} = \sqrt{\langle x^2 \rangle \langle x'^2 \rangle - \langle xx' \rangle^2}$ at the exit of the anode was 1.0 mm·mrad, where x and x' were the position and angle of the electrons in x coordinate. The normalised emittance which is given by $\varepsilon_{norm} = \beta\gamma\varepsilon_{x,RMS}$ corresponded to 0.3 mm·mrad.

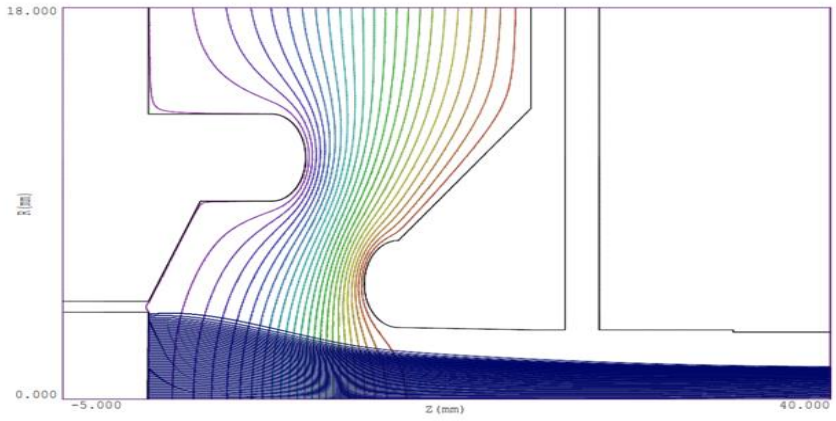

Figure 4-14. TRAK simulation used for calculating for the emittance at the exit of the anode.

Summary

The intention of this chapter was the design and the simulation of the static electron gun using a Finite Element Method code called TRAK. Initially, the electron gun was designed based on Vaughan synthesis and was further optimised for better beam laminarity using the TRAK code. Parameters like the cathode radius, the cathode-anode gap distance and the focusing electrode angle and how these parameters affect the beam current and the beam waist radius were investigated. Furhemore, it was validated that operating in the space charge regime resulting in the cathode temperature to have no effect on the emission. The root mean square (RMS) normalized transverse beam emittance defined by $\varepsilon_{x,RMS} = \sqrt{\langle x^2 \rangle \langle x'^2 \rangle - \langle xx' \rangle^2}$ at the exit of the anode was 1.0 mm·mrad. This design was the basis of our RF electron gun whose performance will be compared with the developed theoretical model from chapter 3.

Chapter 5

5 Particle-in-Cell Simulations of the RF Gun

The optimised geometry of the static electron gun was obtained using the 2D TRAK code. This geometry was transferred into an FDTD-PIC code, MAGIC, where the RF signal was introduced and the performance of the electron gun in terms of bunch charge, bunch length and emittance was investigated.

5.1 Particle-in-Cell (PIC) Method

Particle in Cell (PIC) is a numerical method that simulates the motion of charged particles. Charged particle motion involves simulation between charged particles and electromagnetic fields which could be quite complicated, however the PIC simulation method has some reduced computational procedures. These procedures involve a simulation region that is divided into cells with discrete charge and current density defined in each cell. The two quantities that play an important role in these calculations

are the charge density and the current density. The charge density results from the number of the particles in the specific cell with the charge of each divided by the cell volume. The current density is a product of the average velocity of the particles and their charge divided by the cell area. In order to generate an electromagnetic field, Maxwell's equations, the current density equation and space charge are solved together. The PIC process can be visualized from the flow chart shown in Figure 5-1 [106]. Each step of the cycle is described below.

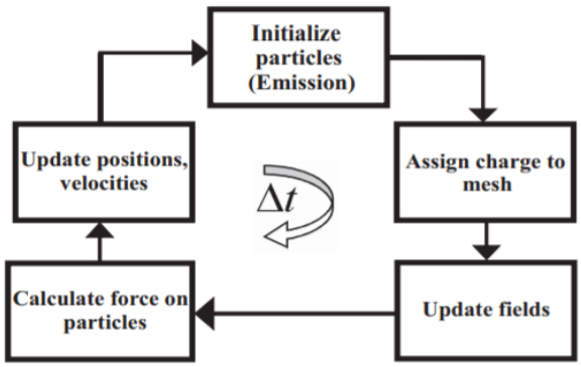

Figure 5-1. Particle In Cell simulation cycle.

A PIC simulation starts by defining the particle positions and their initial velocities. The emission sources are identified and position vectors for particles are defined over the surface. The velocities are initialised by Maxwell-Boltzmann distribution function or can also be set to zero, depending on whether the particles are emitted with initial velocities which could play an important role in the overall dynamics of the system.

The next step involves assigning the charge of all particles inside a cell and relate the exerted forces on the particles due to the fields defined at the cell nodes. There are different ways to do this depending on the accuracy required and the computational cost. One of the ways implemented is called the Nearest Grid Point (NGP) [107].

The Nearest Grid Point (NGP) is a weighting scheme where the force is calculated from the nearest grid point from the particle position and the same procedure is applied to the charge deposition as shown in Figure 5-2. If we consider a one-dimensional mesh for simplicity reasons with corresponding mesh nodes separated by a distance H as shown in Figure 5-2 then the weighting function for the NGP scheme can be written as

$$W(x - x_p) = \begin{Bmatrix} 1, |x - x_p| \leq \frac{H}{2} \\ 0, |x - x_p| > \frac{H}{2} \end{Bmatrix} \quad (5\text{-}1)$$

where, x_p is the position of the particle and x is the position of the grid point. Now the force interpolation function can be written as

$$F(x_p) = q_p \sum_{p=0}^{N_p - 1} W(x - x_p)\,(E_p + v \times B_p) \quad (5\text{-}2)$$

where, N_p is the number of grid points, q_p is the charge and $E_p$is the electric field and B_p the magnetic field at the grid point. Similarly, the charge deposition over the grid can be written as,

$$\rho(x) = \sum_{p=0}^{N_p - 1} \frac{q}{h} W(x - x_p) \quad (5\text{-}3)$$

where $\rho(x)$ is the total charge density at a grid point x and q is the charge of the particle located at x_p.

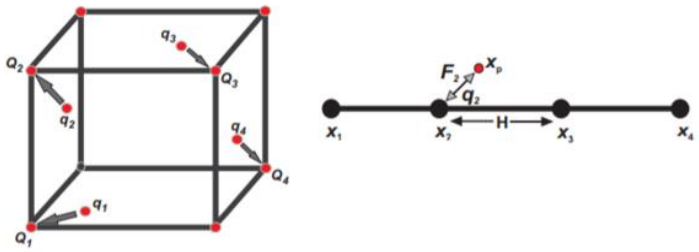

Figure 5-2. The Nearest Grid Point (NGP) scheme.

5.2 Finite-Difference Time-Domain (FDTD)

PIC method solves Maxwell's equations in each mesh cell. The nature of Maxwell's differential equations is that the time derivative of the magnetic field (H) depends on the curl of the electric field (E), and the time derivative of the electric field is dependent on the curl of the magnetic field. These interdependent properties were the key reason for introducing the Finite-Difference Time-Domain (FDTD) technique. At any point in space, an updated value of an E/H-field in time is dependent on the stored value of the E/H-field, and the numerical curl of the local distribution of the H/E-field in space.

5.2.1 Maxwell's equations

The differential form of Maxwell's equations are

$$\frac{\partial \boldsymbol{D}}{\partial t} = \nabla \times \boldsymbol{H} - \boldsymbol{J} \tag{5-4}$$

$$\frac{\partial \boldsymbol{B}}{\partial t} = -\nabla \times \boldsymbol{E} \tag{5-5}$$

$$\nabla \cdot \boldsymbol{B} = 0 \tag{5-6}$$

$$\nabla \cdot \boldsymbol{D} = \rho \tag{5-7}$$

Where $\boldsymbol{D}$ is the electric flux density, $\boldsymbol{H}$ is the magnetic field density, $\boldsymbol{B}$ is the magnetic flux density, $\boldsymbol{E}$ is the electric field density, $\boldsymbol{J}$ is the electric current density and ρ is the

electric charge density. Equations 5-6 and 5-7 represent differential form of Gauss's laws for electric and magnetic fields, equation 5-5 represents differential form of Faraday's law and 5-4 represents the differential form of Ampere's law.

Constitutive relations, equation 5-8 and equation 5-9, allow manipulation of Maxwell's equations and relate **B** to **H** and **D** to **E**

$$\mathbf{B} = \mu \boldsymbol{H} \qquad (5\text{-}8)$$

$$\boldsymbol{D} = \varepsilon \boldsymbol{E} \qquad (5\text{-}9)$$

Here $\mu = \mu_0 \mu_r$ and $\varepsilon = \varepsilon_0 \varepsilon_r$ with μ_0 and ε_0 the permeability and permittivity of free space respectively and μ_r and ε_r the relative permeability and permittivity of a specific medium respectively.

5.2.2 Finite-Difference Time-Domain (FDTD) Technique

The FDTD technique was originally introduced by Yee in 1966 and is based on the time and spatial discretization of Maxwell's equations to obtain solutions for the electromagnetic field in the time domain [108] [109].

The technique is numerically implemented by continuously sampling the electromagnetic field over the wave propagation in the medium which is discretized into a grid. This grid is popularly called the Yee lattice, and is a numerical three-dimensional space lattice comprised of multiples of Yee cells. Figure 5-3 (top) [110] shows a standard Cartesian Yee cell.

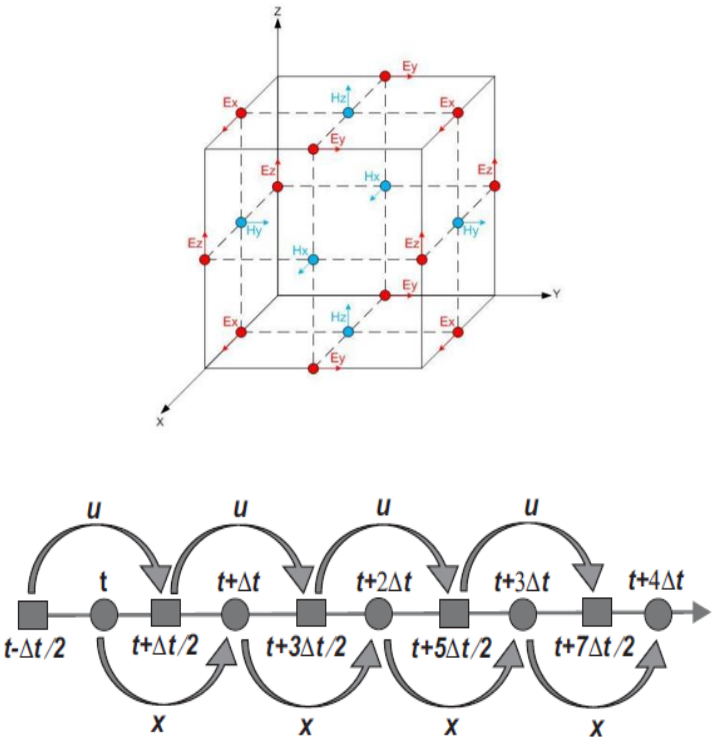

Figure 5-3. Standard Cartesian Yee cell used for FDTD technique(top) and the leapfrog method where the position and the velocity is calculated between two consecutive forward and backward time value (bottom).

As it has been shown in the picture by dashed lines, there is a time step difference between electric field (**E**) and magnetic field (**H**). Due to the central difference approximation technique in time, the magnetic field is present at $t = (n + \frac{1}{2})\Delta t$ where "n" is an integer and electric field is known at integral multiples of the time step. These half-time steps are introduced to perform the finite difference computation of electric field based on the magnetic field and vice versa. After calculation of initial conditions with satisfaction of Maxwell's equations, the electric and magnetic fields are then advanced in time using finite-differenced forms of Ampere's law and Faraday's law, and Equations (5-4) and (5-5). Also, other Maxwell's equations, which were illustrated through Equations (5-6) and (5-7), remain satisfied in time. The FDTD method

approximates both temporal and spatial derivatives of Maxwell's equations through substitution with finite differences, discretising in both time and space to iteratively step the electric and magnetic fields, advancing the fields such that the unknown future fields are predicted from the known past fields and particle trajectories, the leapfrog method, as shown in Figure 5-3. Updated at each time step are the six vector electromagnetic field components associated with each grid cell and the positions and velocities of each particle in the simulation. The difference equation using the leapfrog method becomes

$$F_i^n = qE_i^n + q\left(\frac{u_i^{n+1/2} + u_i^{n-1/2}}{2}\right) \times B_i^n \qquad (5\text{-}10)$$

where F_i^n is the Lorentz force on the i[th] particle due to electric field E_i^n and B_i^n magnetic fields and q the charge of the particle.

The Yee algorithm incorporates edge elements (used to define a vector value along edges between nodes) of one field type (electric or magnetic) with centre point evaluation of the other. The Yee unit cell, Figure 5-3, forms the computational grid with the magnetic field vector components known at points situated at half cell offsets between the electric field nodes in each dimension and vice versa.

Hence the Yee cell is constructed such that all electric field components are centred on and surrounded by four 'circulating' magnetic field components. Conversely all magnetic field components are centred on and surrounded by four 'circulating' electric field components i.e. the centre point evaluation method. Calculations are interleaved in both domains with only adjoining cell interactions being considered when the fields are advanced.

FDTD codes can be computationally intensive as the entire system to be simulated must have a continuous structured grid, with the grid resolution sufficiently high to resolve both the smallest geometrical entity comprising the system and the smallest wavelength with enough sampling points. A typical constraint on this grid resolution, to produce accurate results, is that the mesh cell dimensions should be one tenth (or less) of the wavelength calculated for the highest frequency of interest. From this grid cell resolution the maximum time step can be calculated [111].

Electromagnetic waves propagating in free space cannot exceed the speed of light, c, and as such this provides a physical limit to give a relationship between the spatial and temporal domains. This limit is referred to as the Courant stability criterion, where the maximum time step is selected to be smaller than the smallest possible transit time for a particle across a unit cell.

$$\Delta t \leq \frac{1}{c\sqrt{\frac{1}{\Delta x^2}+\frac{1}{\Delta y^2}+\frac{1}{\Delta z^2}}} \qquad (5\text{-}11)$$

This condition ensures the stability of a system and means that energy cannot propagate beyond one spatial grid cell in one time step [112].

5.3 Modelling using MAGIC (RF gated gun)

The Particle-in-cell (PIC) based MAGIC Toolsuite 2D software tool has been used in this thesis for simulating the Pierce electron gun. MAGIC is a 2D and a 3D numerical simulation code that self-consistently solves the full set of time-dependent Maxwell's equations and the complete Lorentz force equation to provide the interaction between space charges and electromagnetic fields. FDTD electromagnetic algorithms are

combined with PIC approaches to provide fast, accurate, time-dependent calculations of the fields and particle motion in phase-space.

The accuracy of the simulation results in MAGIC (which is based on the PIC method) is highly dependent on the size and number of the grids or cells. As a general rule, having more cells with finer sizes leads to higher accuracy in the results. However, a simulation with finer grids takes more time and computational costs. MAGIC is used to provide a reliable solution for the interaction between charged particles and electromagnetic fields. MAGIC code is able to represent structural geometries, material properties, incoming and outgoing waves and particle emission processes. These emission processes include explosive emission, field emission, photoelectric emission, thermionic emission and secondary emission.

Explosive emission results from plasma formation on a material surface. A simple, qualitative explanation for initiation of the explosive emission is that an applied external voltage creates high electric fields (in the 10^7–10^8 V/cm) at cathode micro-protrusions or “whiskers”. Electrons are then emitted from the surface by processes such as field emission. The current density is given by the Fowler-Nordheim equation as seen in Chapter 2. In thermionic emission, thermal energy is required to overcome the work function. In this condition, the current density is given by Richardson’s law. For secondary electron emission the incident electrons provide the required energy for overcoming the potential barrier of the function.

In MAGIC, rectangular grids are used and the spatial grid is the primary determinant of accuracy. The grid dimensions, such as Δr and Δz, must be defined in the program. The results of a FEM model must be independent of mesh size. A convergence study

was carried out to ensure the FEM model captures the systems behaviour, while reducing the running time. This can be shown in the following graph where the running time (s) and the collected current (A) is plotted against the number of the mesh cells. As expected, the addition of mesh cells increases this time. However, at a point there is no more refinement in the solution. Refinement past this point is an inefficient application of FEM.

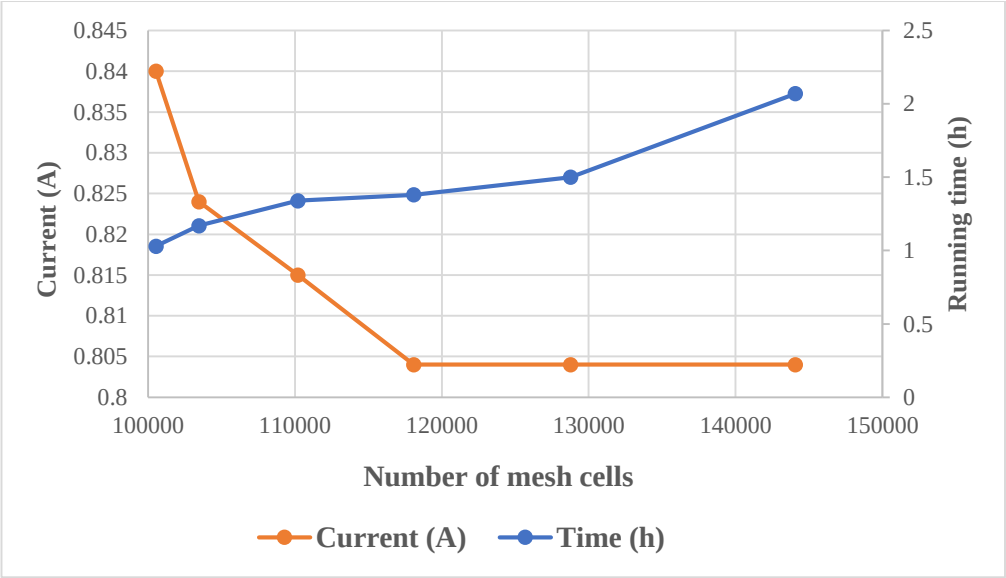

Figure 5-4.Running time and collected current at the anode against the number of mesh cells showing convergence at 120,000 mesh cells.

Using this mesh size, the optimised geometry of the E-static electron gun obtained from TRAK simulations was transferred into MAGIC. For this case an RF field was introduced through the coaxial cavity as described in the previous chapter and our theoretical model including the grid structure. The eigenmode solver of CST Microwave Studio was used to calculate the eigen-frequency of the input section for the RF gun (please refer to chapter 6). The complete configuration including the input cavity together with the grid structure is shown in Figure 5-5.

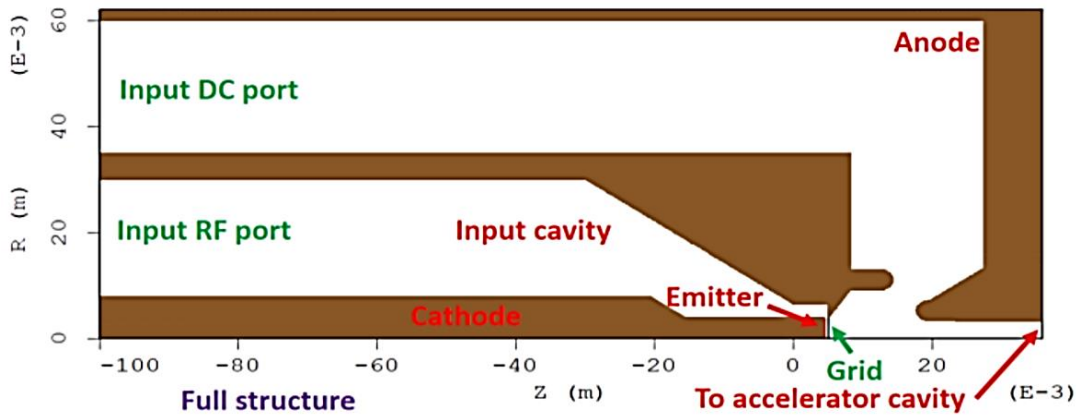

Figure 5-5. Geometry of the RF electron gun using MAGIC.

Using MAGIC, when the electron gun is driven by a combination of an RF voltage and a bias voltage, an electron bunch was generated. Figure 5-6 shows the spatial distribution of electrons at different time frames, corresponding to the process of bunch emission from the emitter, bunch acceleration by the electric field and bunch at the exit of the anode. The running time for each simulation corresponded to 1h and 50 minutes.

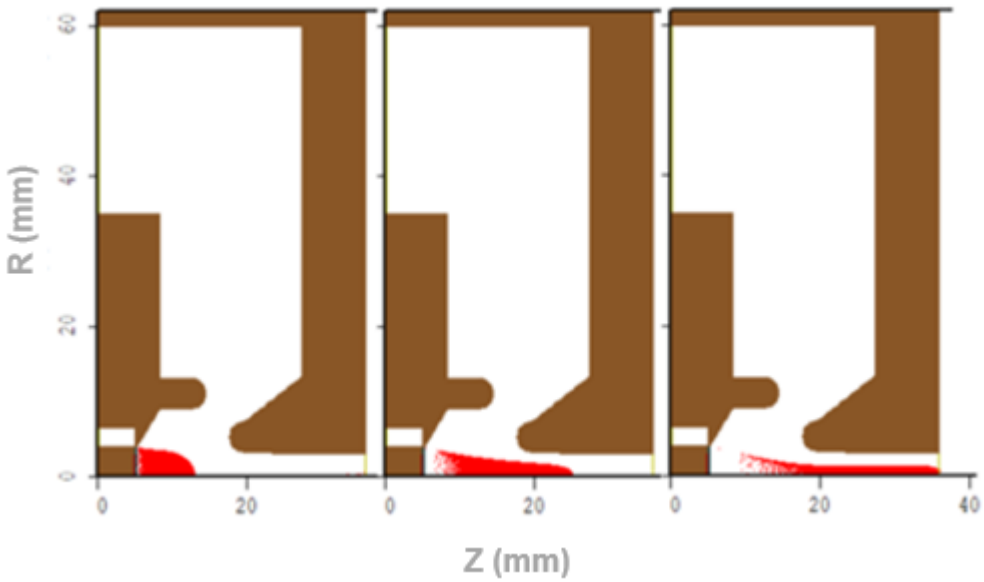

Figure 5-6. Different time frames showing the evolution of the beam bunching at the different regions.

5.4 Effect of different combinations of RF and bias voltage on the emitted current

The simulated results of the peak emitted current as a function of the applied voltage are shown in Figure 5-7. At different bias voltage, U_{bias} but same total voltage, U_{grid} as indicated in the graph, the emitted current is linear over a wide range of the total voltage. This observation validates the approximation of equation 5-11 and 5-12 used in our theoretical model.

$$U_{grid} = U_{rf}\cos(2\pi ft - \theta) + U_{bias} \tag{5-11}$$

$$I = G_{emit}\left(U_{bias} + U_{rf} - U_c\right) \tag{5-12}$$

From Figure 5-7, the value of the G_{emit} for this particular cathode can be extracted from the linear fit. This value was about 18 mA/V.

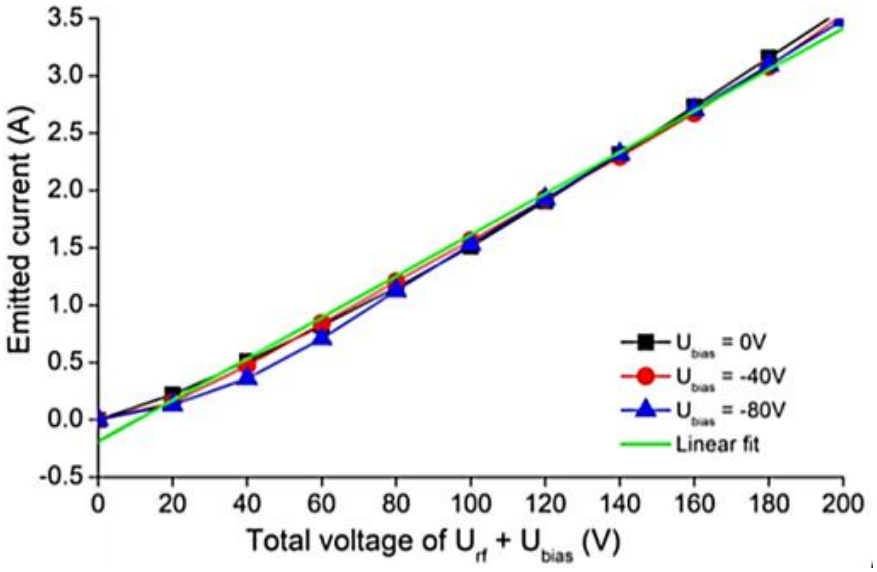

Figure 5-7. Relationship between the grid voltage and the emitted current.

5.5 Discrepancies between the theoretical model and simulation

Before starting the comparison between the theoretical model and the simulation results, it needs to be mentioned that the theoretical model did not include the effects of space charge at the emitter, thermal emission distribution and the beam dynamics between the grid and anode. This potentially could be a reason for any discrepancies risen between them.

Figure 5-8 shows the emitted current from the cathode and the collected current at the entrance of the acceleration cavity at U_{rf} = 170 V and U_{bias} = −115 V. The first comparison involved the waveform of the emitted current which matched well with the theoretical model in Chapter 3. The second comparison involved the amplitude of the collected current pulse waveform of the emitted current which was about 40% of the emitted current. By integrating the current, the charge in the collected and emitted current pulse was calculated. The calculated values corresponded to 72 pC for the

collected current pulse and 43 pC for the emitted. The ratio between them was about 60%, which indicated that 40% of the electrons emitted from the cathode back streamed to the emitter surface due to the deceleration voltage. Comparing the PIC simulation values to the values of the theoretical model for the emitted bunches which were 33pC, the simulation results in a much larger value to the theoretical prediction.

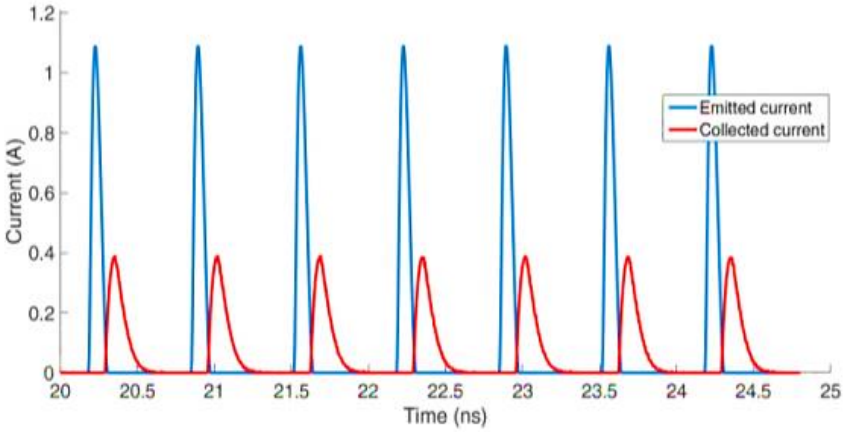

Figure 5-8. The emitted current from the cathode and the collected current at the entrance of the accelerator cavity.

Another comparison between the theoretical values and the values obtained by simulation involves another parameter which is the bunch length. The Full-width-half-maximum (FWHM) lengths of the emitted and collected bunches were 72 ps and 107 ps respectively from the simulation. Again in this case these values are much larger compared with the theoretical prediction for emitted bunches of 68 ps as shown in Chapter 3. As mentioned at the start of this section some effects were not taken into account when the theoretical model was developed. Considering these effects, further simulation work was carried out to quantify these factors that lead to much larger values thus widening the bunch. Each one of them is described below. The values

obtained by the theoretical model and the simulation for the bunch length are summarised in Table 5-1.

Bunch length(ps)	Theoretical model	Simulations
1.5 GHz	68	106
3.0 GHz	23	100

Table 5-1. Summarised values for the bunch length at 1.5 GHz and 3.0 GHz for both the theoretical model and simulations.

5.5.1 Reasons for bunch widening

The different grid voltages as a function of time are one of the major reasons for the widening of the pulse. Taking into account the head of the bunch which had larger energy compared to the tail when driven by the RF field, further work was carried out for different grid voltages. The results showed that a time difference arises when electrons are accelerated by different grid voltages for the same travelling distance. As an example for grid voltage of 10V and 30V the time difference for travelling distance of 0.36 mm which is the grid distance plus the grid thickness the time difference was 81 ps which is quite a large value which majorly contributes to the widening of the bunch. The second contribution comes from the different distances the electrons have to travel from the cathode. The electrons emitted from larger emitter radius travel longer distances. The difference in the traveling time from the TRAK simulation was 28 ps.The last contribution comes from the space charge which was not taken into account when developing the theoretical model. The space charge force accelerates the head of the bunch and decelerates the tail of the bunch which in our case there was

about 16 ps additional contribution to the pulse length due to space charge effects. One way of preventing space charge effects is when operating at a smaller beam current.

5.6 Transverse emittance of the RF gun

The sliced transverse emittance was calculated by statistically counting the electrons at the exit of the anode. The emittance along with the current is shown in Figure 5-9. The two regions of the bunch, head and tail have different values of emittance. The emittance was lower at the head of the bunch and larger at the tail. The region around the tail exhibits some noise due to the statistical variation caused by a small number of electrons. The major part of the bunch had a normalised emittance of less than 5.6 mm.mrad. There are two types of emittance calculated. These were, the geometrical and the normalised emittance. The relationship between these two types of emittance is given by

$$\varepsilon_{norm} = \beta\gamma\varepsilon_{geometrical} \tag{5-13}$$

Where β & γ are the relativistic functions.

The value for the normalised emittance at the exit of the anode for the static, DC electron gun was 0.3 mm·mrad which is a much smaller value compared to the PIC simulation result. The reason for this discrepancy is assigned to the weak acceleration field due to the RF voltage applied between the cathode and grid, as well as the uneven space charge force on the bunch resulting in higher emittance for the RF gun compared to the DC gun.

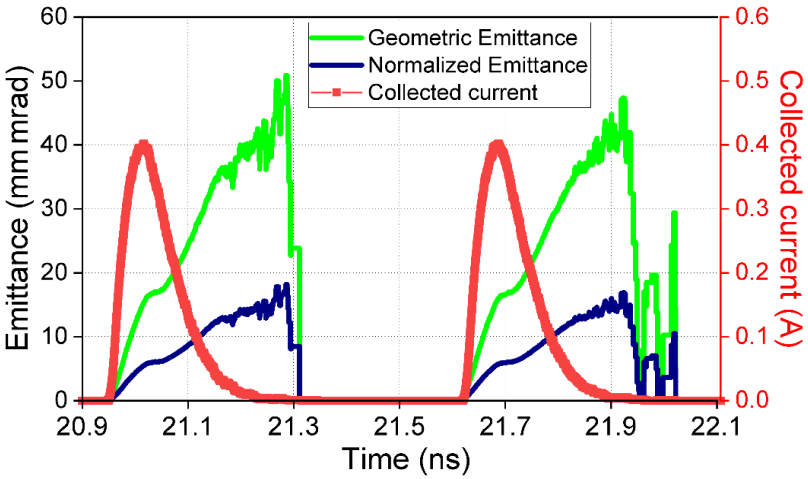

Figure 5-9. The emittance of the electron at the exit of the anode .

The major part of the bunch had a transverse or geometric emittance of less than 17 mm·mrad, corresponding to a normalised emittance of 5.6 mm·mrad. The emittance was lower at the head of the bunch and it increased as a function of the bunch charge. The noise of the emittance at the end of the bunch was due to the unstable statistical variation due to the small number of electrons. The PIC simulation showed a much bigger emittance compared to the static electric field case, due to the energy spread and space charge effect in the RF gun.

5.7 Relationship between bunch length and bunch charge at 1.5 GHz and 3.0 GHz RF frequency

Figure 5-9 (top) shows the simulation results at different combinations of U_{rf} and U_{bias} at a driven frequency of 1.5 GHz. Investigating how the U_{bias} and the U_{rf} affect the bunch charge and the bunch length it was observed that when fixing U_{bias} while increasing U_{rf} both larger bunch charge and longer bunch length were growing in a linear trend, which was different from the theoretical prediction. The theoretical model showed that a larger U_{bias} value which corresponds to a smaller θ helps to reduce the bunch length which also got verified with the PIC simulations however the impact on the bunch length was very small compared to the predicted value. By increasing the bias voltage from -80 V to -170 V, the difference in the bunch length was about 5 ps only at the same bunch charge. The minimum bunch length of 106 ps could be achieved with a bunch charge of 33.3 pC.

Another prediction of the theoretical model involved the reduction of the bunch length by operating at the higher RF frequency. The PIC simulation proved the trend, however, it was found that more electrons were back streamed to the emitter when operating at a higher frequency. The bunch length and bunch charge at different grid voltages with RF frequency of 3.0 GHz is shown in Figure 5-10 (bottom). The minimum bunch length of 100 ps could be achieved with a bunch charge of 16.7 pC, which means the bunch length at the entrance of the LINAC was reduced slightly at a higher frequency. As we saw in the previous sections the main two reasons for the pulse widening were mainly determined by the electron gun structure. In this case no significant advantage was to be gained by operating at a higher RF frequency as this does not reduce the pulse width or shorten the bunch length. When operating at a

higher frequency, the emitted current had to have larger compensation due to the higher ratio of the backstreaming electrons. The space charge force, therefore, became larger and resulted in longer pulse widening. It also results in larger emittance.

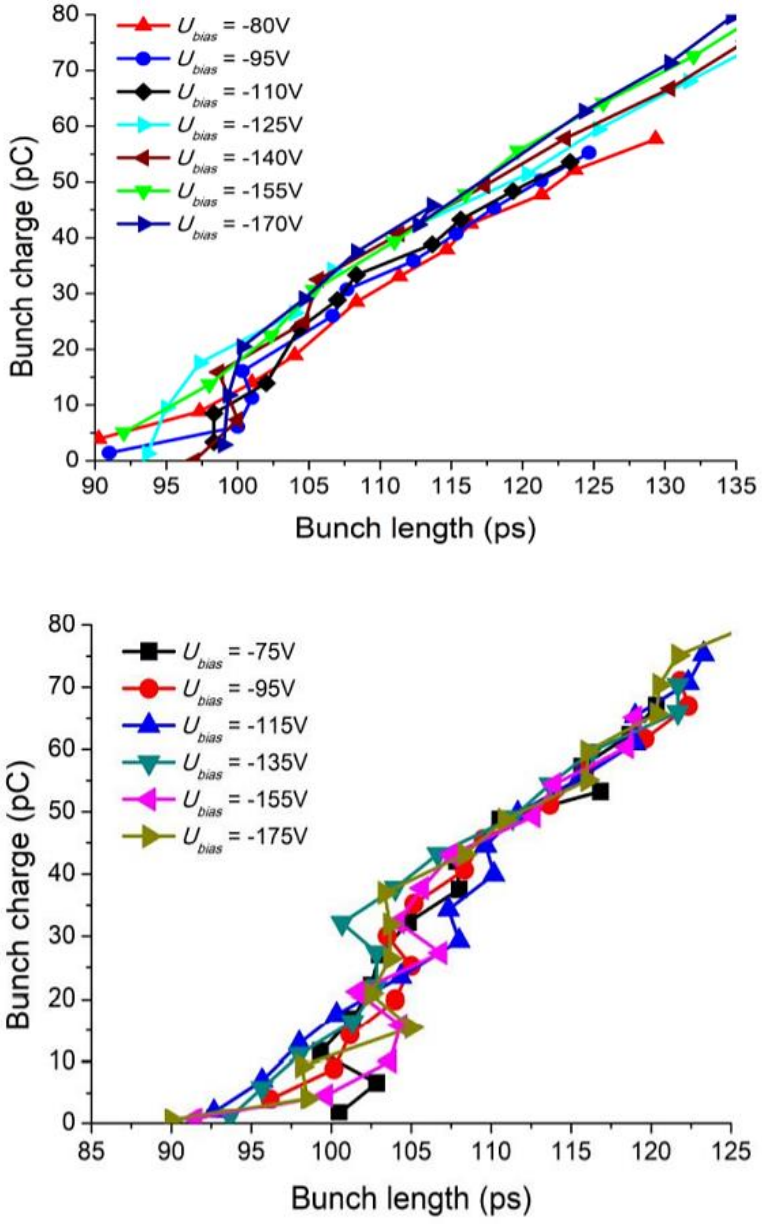

Figure 5-10. The relationship between the bunch length and bunch charge at different grid voltages with RF frequency of 1.5 GHz (top) and 3.0 GHz (bottom).

Summary

In this chapter the performance of our RF electron gun was presented. The developed and optimised static electron gun using TRAK was used as a basis while introducing an RF signal in our design. This time a FDTD code, MAGIC, was used to simulate the RF electron. The effect of the combination of the RF and a bias voltage on the emitted current and the relationship between the bunch length and bunch charge was examined. The minimum pulse length of 106 ps could be achieved with a bunch charge of 33.3 pC when the driving RF frequency was 1.5 GHz. These values indicate a longer bunch length compared to 68ps obtained from the theoretical model in Chapter 3. The main reason for the bunch lengthening was the energy difference of the electrons passing through the grid which lead to different travel time of the electrons. Lastly, the average normalised emittance was 5.6 mm·mrad.

Chapter 6

6 3D Simulation of RF gated Gun using CST Particle Studio

CST Particle Studio, Simulia Dassault Systemes, is used to simulate charged particle dynamics under electric and magnetic fields. In this thesis, 3D simulation work was carried out using CST Particle Studio to be compared with the 2D simulations results obtained in Chapter 5. In Particle Studio, there are four different solvers namely Particle Tracking, Particle-in-Cell, Eigen Mode solver and Wakefield Particle solver. No frequency domain simulations were carried out using CST Microwave Studio. For this work, the Particle Tracking and the Particle-In-Cell code were used for the static and the RF gun respectively. Most of the simulations were done using the time domain FDTD solver in CST to complement the simulations carried out using MAGIC presented in chapter 5. Particle Tracking Solver track particles in pre-calculated electromagnetic fields by using Lorenz force equations. The gun iteration option takes into account space charge effects on electromagnetic fields as shown in Figure 6-1.

Particle Tracking Solver is suitable for the problem types which do not include time variation and RF field while Particle-in-Cell solver takes into account particle and time-varying electromagnetic fields.

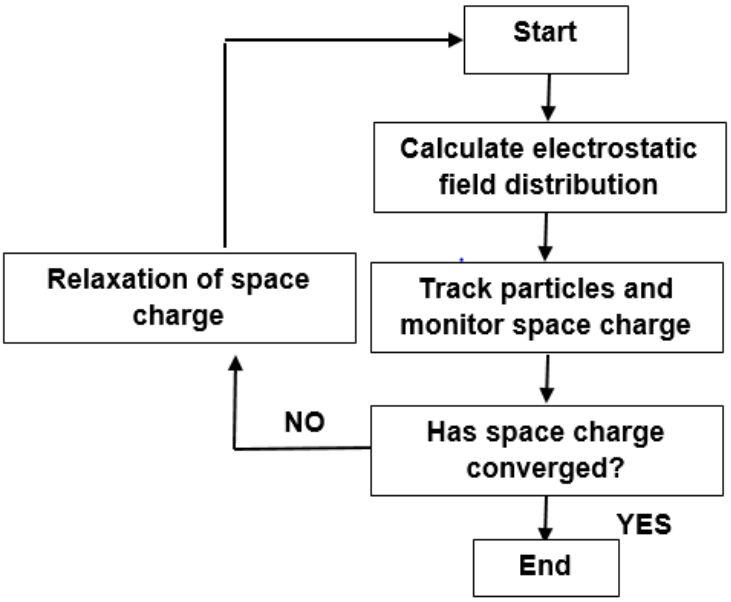

Figure 6-1. Gun iteration algorithm including space charge.

In CST simulations, the emitted particle can be an electron, a proton or a helium ion. Furthermore, the particle type can be defined with its charge and mass. There are three types of emission models which are thermionic, space charge and field emission. The space charge emission model is based on the Child-Langmuir model and particles are emitted according to Child's law. The thermionic emission model is based on the Richardson-Dushman equation. The last emission model is the field emission in which particle extraction occurs due to a high electric field and is governed by the Fowler-Nordheim equation.

In this part of the thesis, a parametrical analysis of the Pierce electron gun was carried out in 3D to compare with the 2D simulation results. Some of the geometrical

parameters examined with TRAK (cathode radius, cathode-anode gap) and one electrical parameter (cathode voltage) were investigated for direct comparison to our 2D simulation work. Furthermore, 3D simulation work of the RF electron gun was conducted to be compared with results obtained with MAGIC 2D.

6.1 Beam dynamics comparison between 2D and 3D simulations

6.1.1 Static electron gun

Simulation results of investigating the effect of different geometrical and electrical parameters of a Pierce electron gun on the beam quality are directly compared to the results obtained with 2D simulations (TRAK). This analysis was carried out by examining one electrical and two geometrical parameters and the effect they have on the collected current at the anode. These results were compared with the 2D simulations. These parameters included the cathode voltage (electrical parameter), the cathode-anode gap and the cathode radius (geometrical parameters).

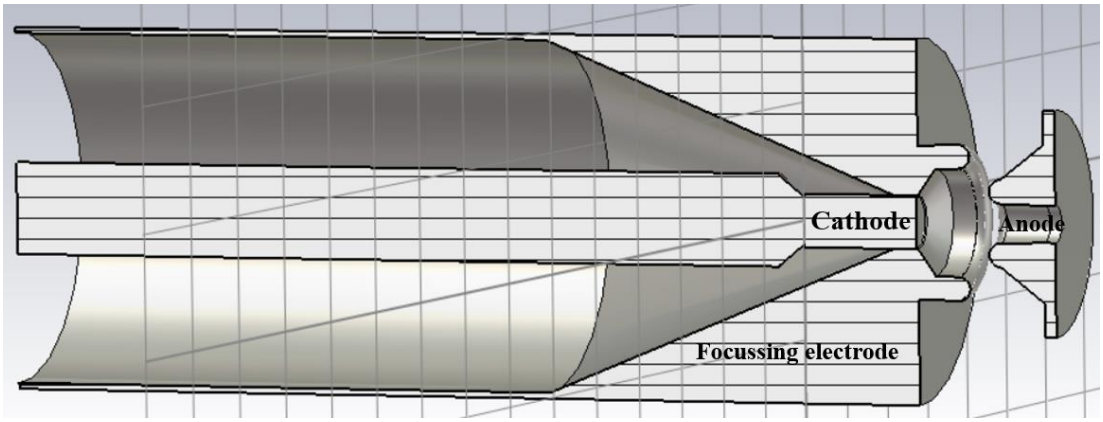

Figure 6-2. Schematic diagram of the 3D geometry of the static electron gun using Particle CST Studio.

6.1.1.1 Cathode Voltage

The voltage potential between the cathode and anode is produced by inserting a negative voltage value into the cathode body. It is expected that the current rises with cathode voltage. This expected pattern is observed in Figure 6-3 where the value of the current is increasing with the cathode voltage. The CST results showed a similar trend as the TRAK results however a slightly lower value of current was obtained for higher voltages as seen in Figure 6-3. One possible reason for this discrepancy at higher voltages could be due to space charge which would be higher in a 3D surface compare to a 2D area suppressing in this way the current. The space charge effects would be more prominent at higher values of cathode voltage thus the observation at these values.

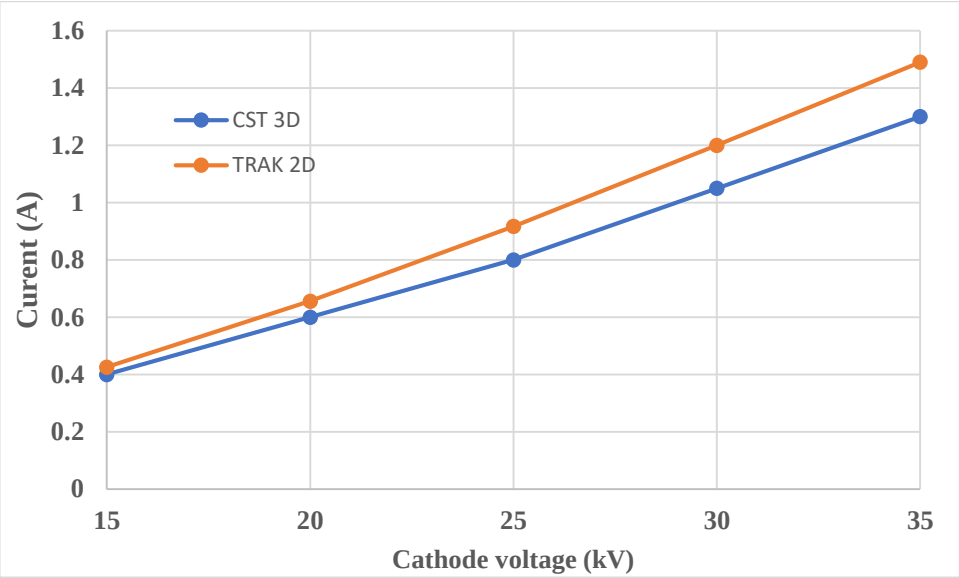

Figure 6-3. Collected currents for different cathode voltages and comparison between the results obtained with TRAK 2D and CST 3D.

6.1.1.2 Cathode-anode spacing

Another important parameter in gun design is the anode-cathode gap. Seven different values of the cathode-anode gap were used. The current versus the cathode-anode gap is given in Figure 6-4. As the emitted current decreases, the cathode-anode gap increases. Again, for this set of simulations slightly higher value of current was obtained with TRAK 2D than CST 3D. The decreasing trend of the current as the gap distance between the cathode and the anode increases is due to the change in the Electric field as shown in Figure 6-5.

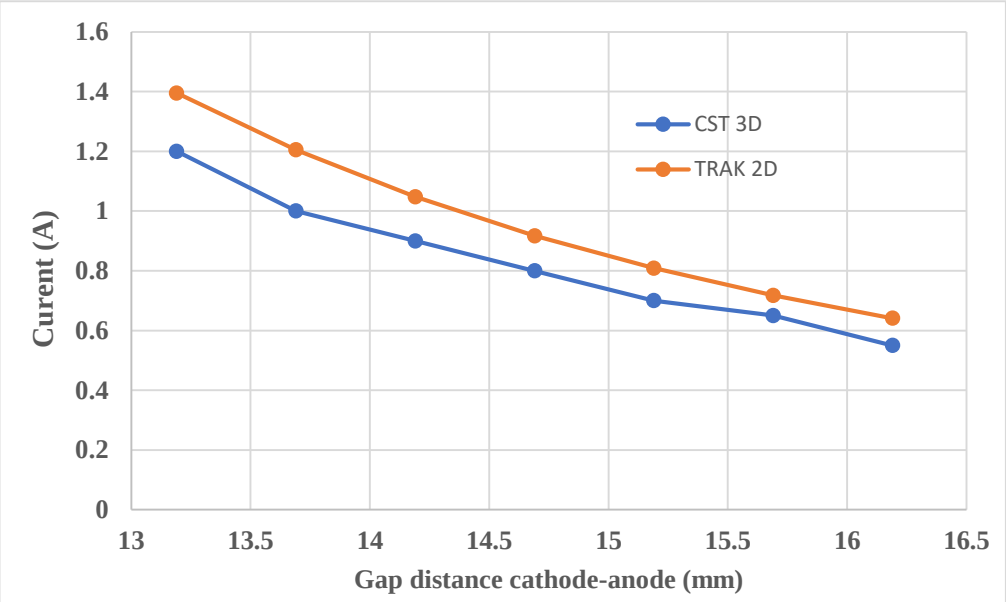

Figure 6-4. Collected currents for different gap distances between the cathode and the anode.

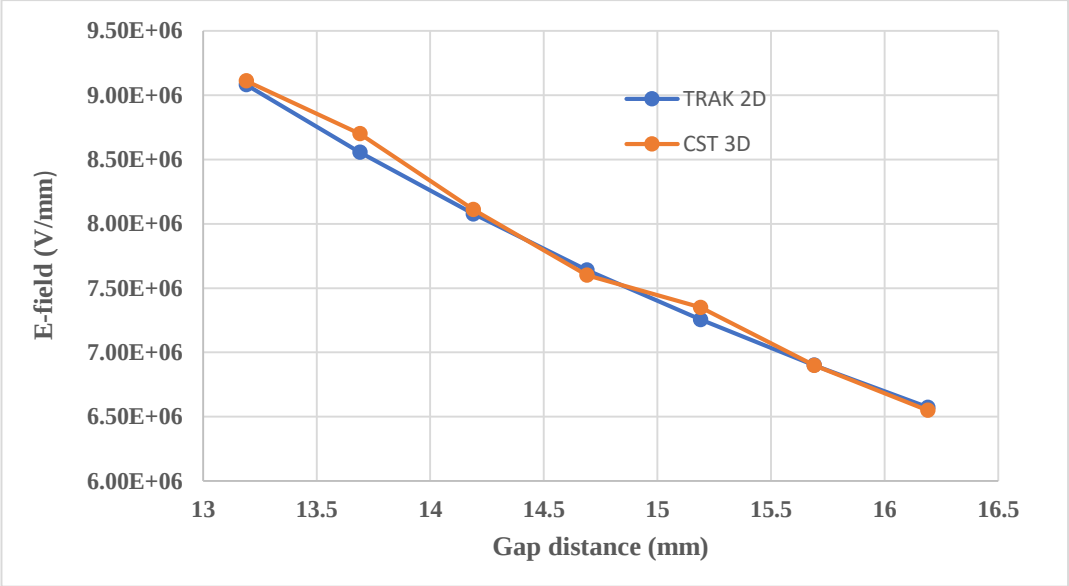

Figure 6-5. Electric field variation for different cathode-anode distances.

6.1.1.3 Cathode Radius

Cathode radius is one of the most important parameters influencing the beam current as the cathode area is directly related to the current according to the Child-Langmuir law

$$J = \frac{4}{9}\varepsilon_0\sqrt{2\frac{2Z_e}{m_0}}\frac{\pi r^2}{d^2}\frac{V^{3/2}}{x^2} \qquad (6\text{-}1)$$

Figure 6-6 shows the emitted current for different cathode radiuses. From Figure 6-5 it can be seen that as the cathode radius is increasing, the beam current follows the same trend as expected. Once more, TRAK gave slightly higher values of collected current compared to CST.

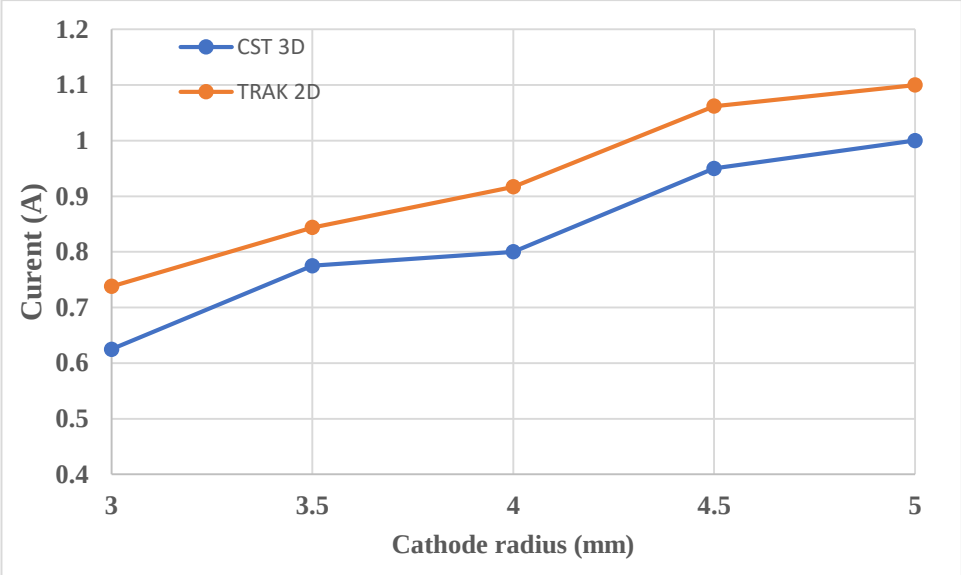

Figure 6-6. Collected currents for different cathode radiuses.

6.2 CST modelling of the RF electron gun

The time domain CST solver of Maxwell's equation in integral form using the Finite Intergration Technique (FIT) was used to model the RF electron gun. The integral form of Maxwell's equations given by equations 6-2 to to 6-5 can be obtained by applying the divergence theorem to the differential form of Gauss' law and Gauss' law of magnetic fields in section 5.2.1.

$$\oint_S D.ds = \oint_V \rho \, dV \qquad (6\text{-}2)$$

$$\oint_S B.ds = 0 \qquad (6\text{-}3)$$

with the conversion from the differential form of both Faraday's law of induction and Ampère-Maxwell's law to their integral forms requiring Stokes' theorem which can be written as

$$\oint_S (\nabla \times H).ds = \oint_C H.dl \qquad (6\text{-}4)$$

where S is any surface bouded by C, and ds is the differential surface area combined with the unit vector in the direction determined by the righ-hand rule from Stokes' Theorem

$$\oint_C E.dl = -\frac{\partial}{\partial t}\oint_S B.ds \qquad (6\text{-}5)$$

$$\oint_C H.dl = \frac{\partial}{\partial t}\oint_S D.ds + \oint_S j.ds \qquad (6\text{-}6)$$

The transient solver of CST Microwave Studio based on the FIT with the perfect boundary approximation (PBA) solving electromagnetic finite integral equations (6-2 to 6-4) was used. The Perfect Boundary Approximation (PBA) technique applied to the FIT algorithm maintains all the advantages of structured Cartesian grids while allowing accurate modelling of curved structures.

The FIT was first proposed in 1977 by Weiland [113] and is based on the full set of Maxwell's equations in integral form discretised on a two grid system, known as the primary and dual grid, Figure 6-7. In the FIT, magnetic and electric grid voltages and grid fluxes are assigned to spatial objects of the grid, defined as integrals of the magnetic and electric field vectors associated with the grid, Figure 6-8 [114].

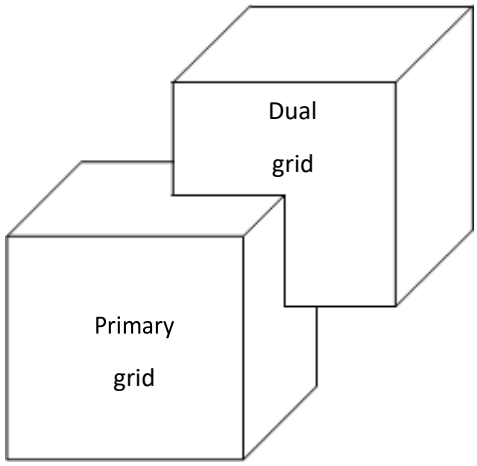

Figure 6-7. Illustration of the primary and dual grid cells used in the FIT [115].

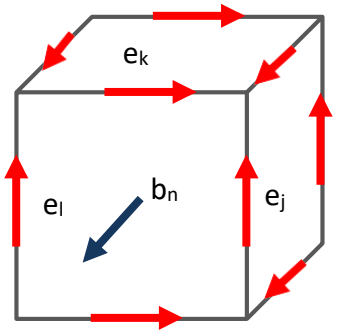

Figure 6-8. Allocation of voltages along edges and fluxes through surfaces in the FIT.

Electric grid voltages and magnetic grid fluxes are allocated to the primary grid on the edges and faces respectively. Assigned to the dual grid on the edges and faces are the magnetic grid voltages and electric grid fluxes [116]. For an individual cell surface Maxwell's equations are defined and the discretised fields summarised in a topological matrix. The full set of these algebraic matrix equations, which retain conservation of charge and energy, are known as Maxwell's Grid Equations (MGEs). MGEs precisely

represent Maxwell's equations on the grid since in this method discretisation is based entirely on the mathematical properties of the integral [117]

The inclusion of matrices however, which describe material properties, allow electromagnetic problems to be solved but introduce numerical approximations. FIT is not restricted to a Cartesian coordinate gird and can be applied to non-orthogonal and irregular grids, a prime advantage over the FDTD method [118]. However on a Cartesian coordinate grid system the FIT and FDTD methods are effectively equivalent[117].

6.3 RF electron gun

Figure 6-9 shows the electron gun along with the coaxial cavity and the added alumina insulator which was inserted to isolate the potential of the grid from the port the RF excitation signal is injected. In CST PIC simulations, thermionic emission or space charge is not an option so another model of emission was used. This emission model was the field emission model. The field emission equation for the current density is given by Equation 6-7

$$J = \frac{A.E^2}{\Phi} \exp\left(-B\frac{\Phi^{3/2}}{E}\right) \qquad (6\text{-}7)$$

Where A and B are the linear and exponential parameter respectively. The field emission parameters were adjusted to fit the Richardson equation for space charge emission with the use of MATLAB. The values for A and B resulted in $8x10^{-7}A/V^2$ and $1.1x10^6V/m$ respectively for a moderate current density of $1A/cm^2$.

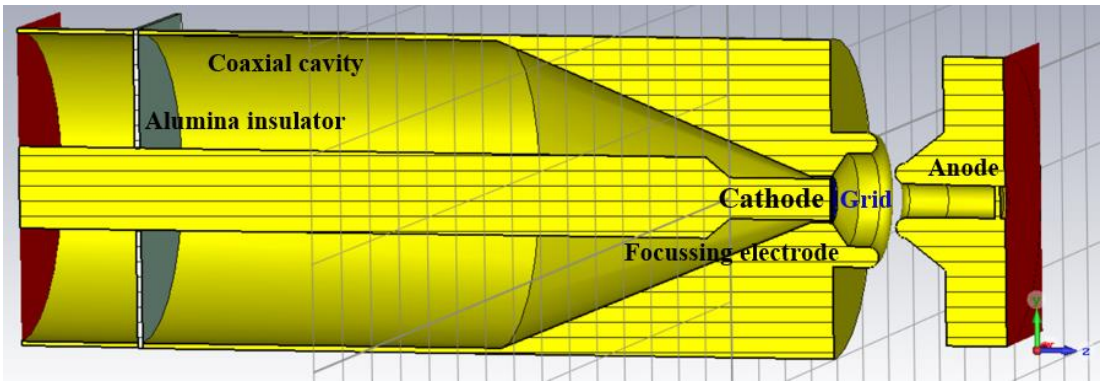

Figure 6-9. Electron gun with the coaxial cavity using 3D CST Particle Studio.

Two different voltages, a bias (V_{dc}) and an RF (V_{rf}) were used. The negative bias on the grid, suppresses electron emission which combined with direct RF modulation of the cathode-grid circuit via a coaxial feed line which was able to produce an electron beam that is bunched at the RF frequency. The RF modulation is introduced through a coaxial line that feeds the cathode-grid circuit. Different combinations of V_{dc} and V_{rf} were used and the effect on the beam was examined. The number of mesh cells corresponded to 2,170,000 and the running time for each simulation was about 4 hours.

The primary bunch diagnostics of interest in our simulations are the emitted current from the cathode, the collected current at the anode, the total charge per bunch and the bunch length for different values of V_{dc} and V_{rf}. The emitted and the collected current is given in Figure 6-10. The emitted current is lower than the cathode current due to interception by the grid.

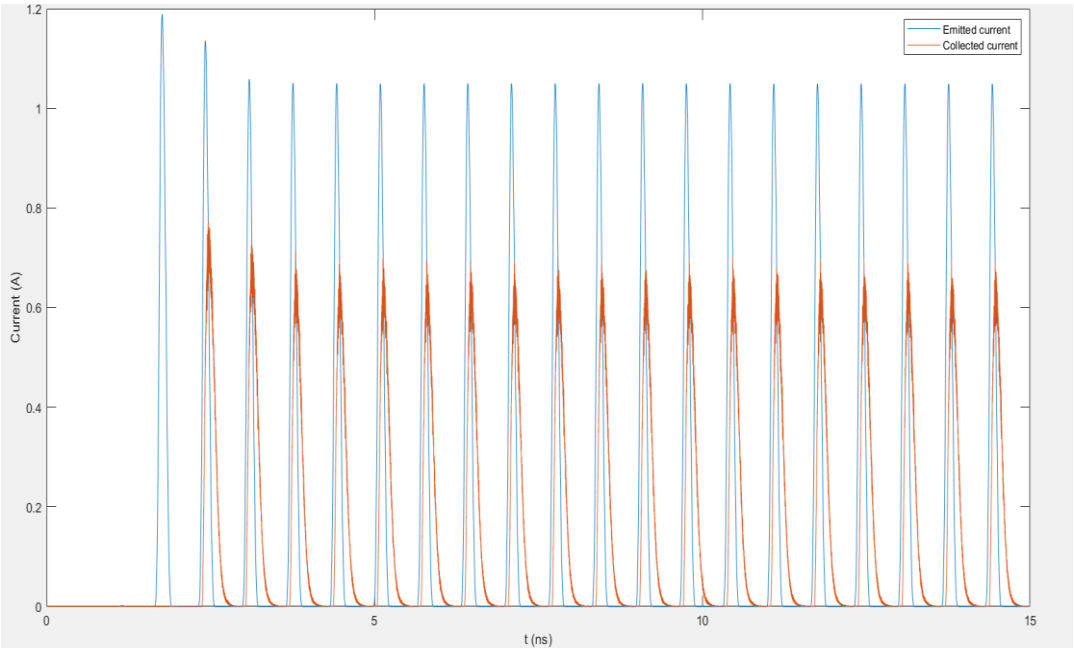

Figure 6-10. Emitted current from cathode and collected current at anode as a function of time for many pulses.

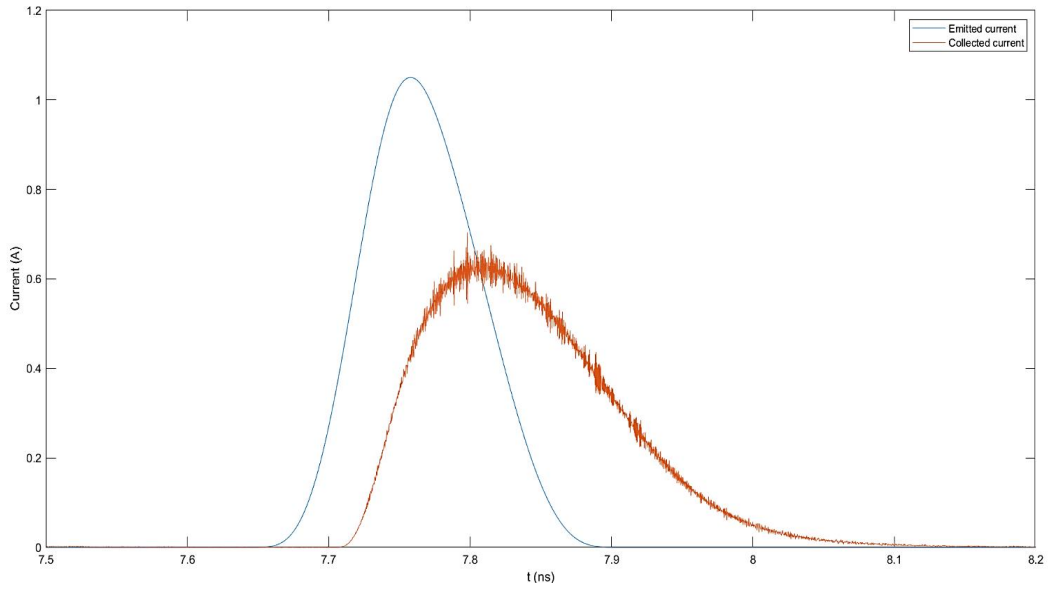

Figure 6-11. Emitted current from cathode and collected current at anode as a function of time for one pulse.

Initially, the amplitude of the RF voltage was set to 15V while varying the value of the bias voltage. Figure 6-12 presents the signals obtained for the collected current at the anode at V_{rf} =15V and V_{dc} = 50, 100, 150, 200 V. From these signals the values of the current (A) and subsequently the bunch length and bunch charge can be measured. Figure 6-12 shows the values of all the above parameters. From these graphs certain observations about the effect of V_{dc} on the beam can be made. Firstly, the collected current is decreasing as V_{dc} is increasing something which is expected as the purpose of the negative bias voltage is to switch off emission. Secondly, the bunch length is increasing as V_{dc} is increasing. Lastly, both the current and the pulse length depends on V_{dc}.

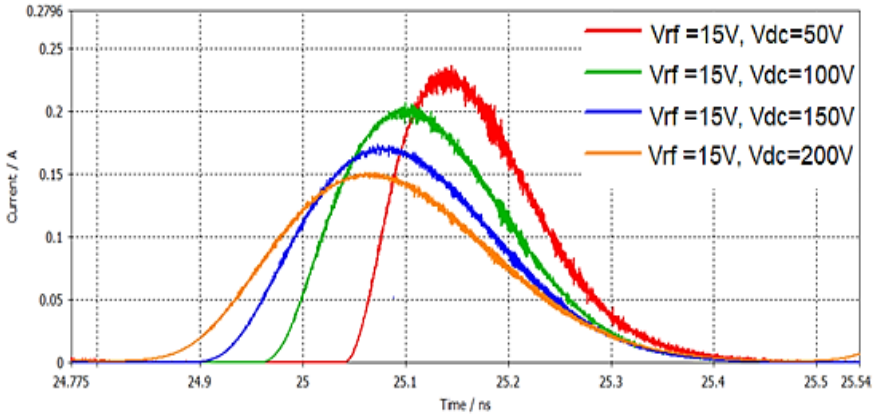

Figure 6-12. Collected currents for different V_{dc} voltages and V_{rf}=15V.

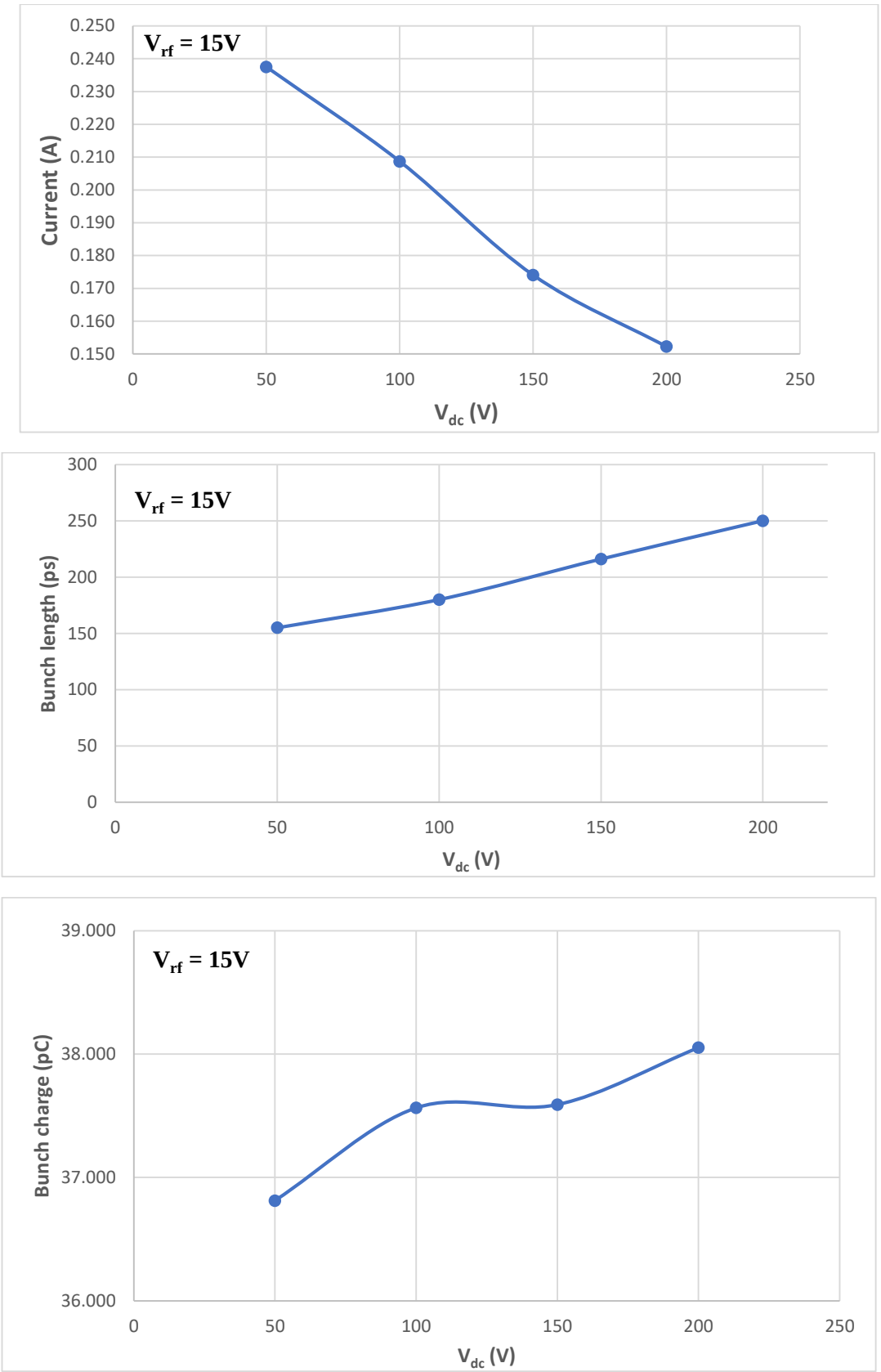

Figure 6-13. Collected current (A), bunch length and bunch charge for different values of bias voltage and V_{rf}=15V (top to bottom).

From the above graphs the value of bias voltage which gives the highest current pulse and the smallest pulse length corresponded to V_{dc} = 50 V. For the next set of simulations the effect of V_{rf} was examined while keeping the bias voltage constant. The values for V_{rf} used were 20, 25, 30, 35, 40 V. For these simulations the collected current, bunch charge and bunch length are given in Figure 6-14. As the amplitude of V_{rf} increases the collected current increases as well similar to our previous simulations for the different values of V_{dc}. However, this time the pulse length is not affected as much by the V_{rf} as it does with the V_{dc}. Overall, the two main observations made from this set of simulations were that the peak collected current depends on both V_{rf} and V_{dc} and the pulse length depends mainly on the V_{dc}.

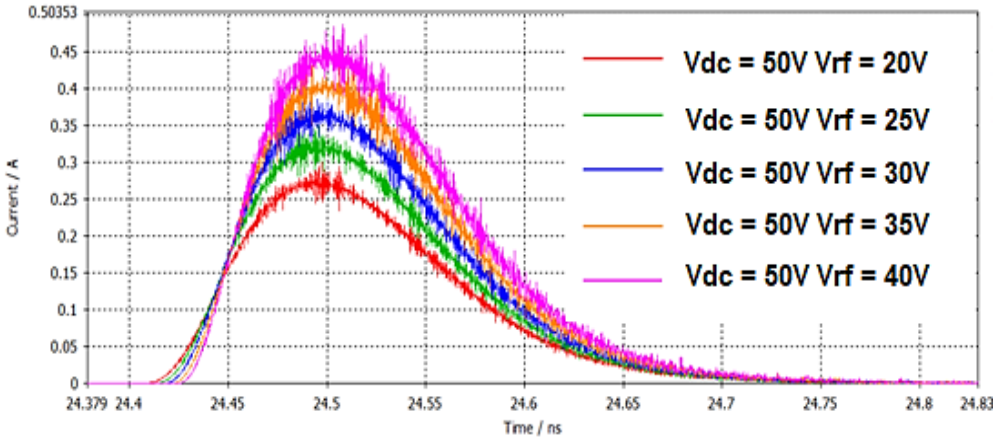

Figure 6-14. Collected current for different Vrf voltages and Vdc = 50V.

Comparing the results obtained with MAGIC 2D, it was observed that when fixing V_{dc} while increasing V_{rf} both larger bunch charge and longer bunch length were observed. In 3D CST Particle Studio, a similar trend was observed however the change in the bunch length was much smaller for different V_{rf} and V_{dc} had more impact on the value of the bunch length. Moreover, MAGIC showed the minimum bunch length of 106 ps could be achieved with a bunch charge of 33.3 pC which is a similar value to 102ps bunch length for 34.6pC bunch charge obtained with CST for V_{dc}=50V and V_{rf}= 25V. Overall, there is a good degree of consistency between 2D and 3D simulations.

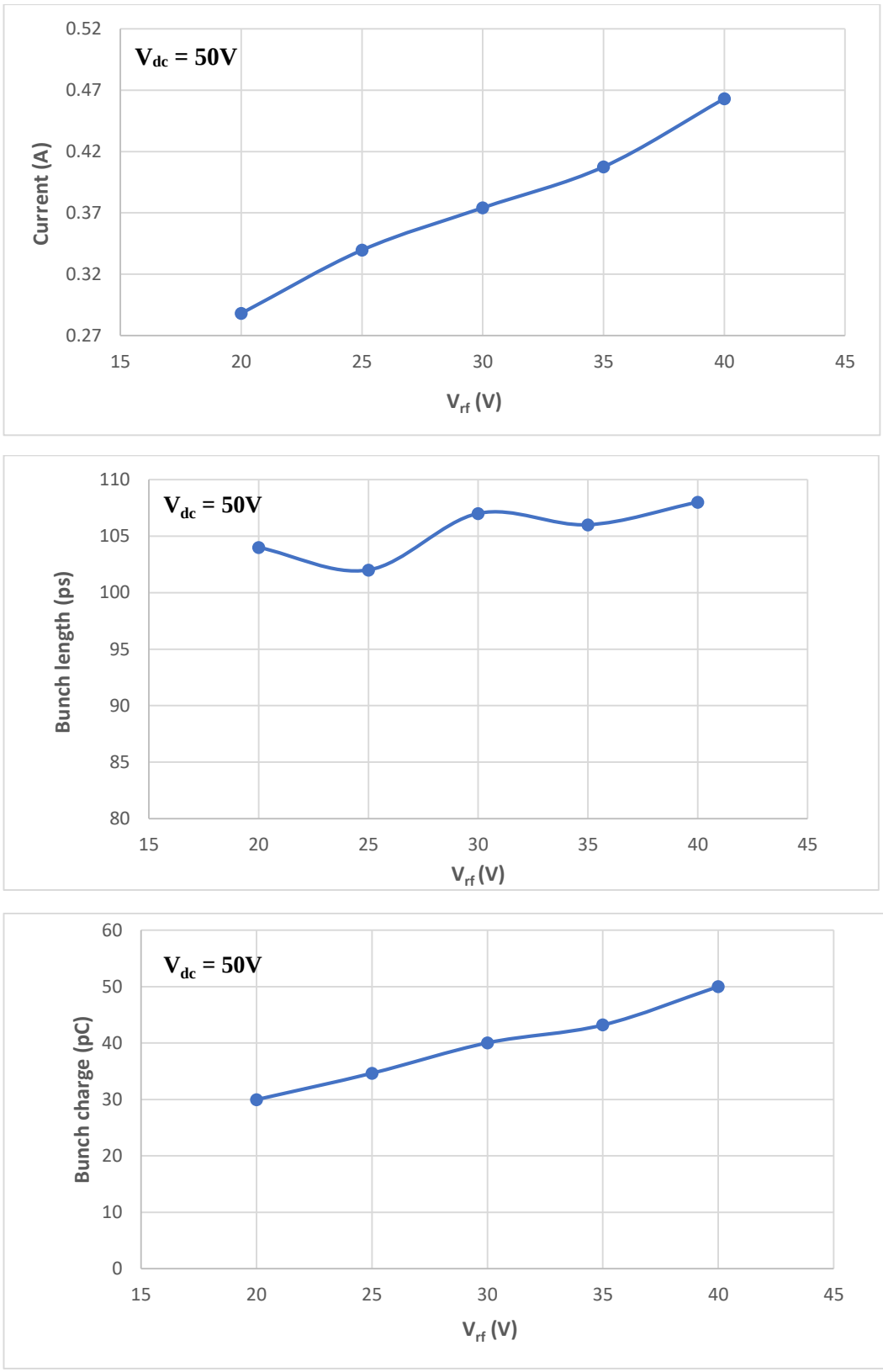

Figure 6-15. Collected current (A), bunch length and bunch charge for different values of Vrf and Vdc = 50V (top to bottom).

6.4 Effect of different designs of grid on the performance of the RF gun

The performance of the gridded cathode assembly gun was investigated in the previous section using 3D CST Particle Studio and more precisely, its PIC solver where the optimised 3D geometry was carefully modelled including a grid. Initially the grid was modelled as a 99% transparent lossy material (graphite) which was biased in order to limit the beam current exiting the cathode. In Figure 6-16 three different types of the modelled grid used in this set of simulations is shown. These are, lossy transparent material, spider web grid and pepper pot grid (top to bottom). These types of the grids chosen to be modelled are not arbitrary. The pepperpot and the spider web type grid are the main types of control grids used in electron guns for beam current control.

The cathode-grid structure shown is composed of the emitting material (cathode), which is connected to the heater power system and a thin grid of 0.16mm thickness, represented in blue and which is connected to the bias voltage supply. The material of the grid was set to graphite and the grid is isolated from the cathode. This time the number of mesh cells was increased to 12,000,000 and the running time corresponded to around 28 hours. The CST simulation results are presented in the following graphs.

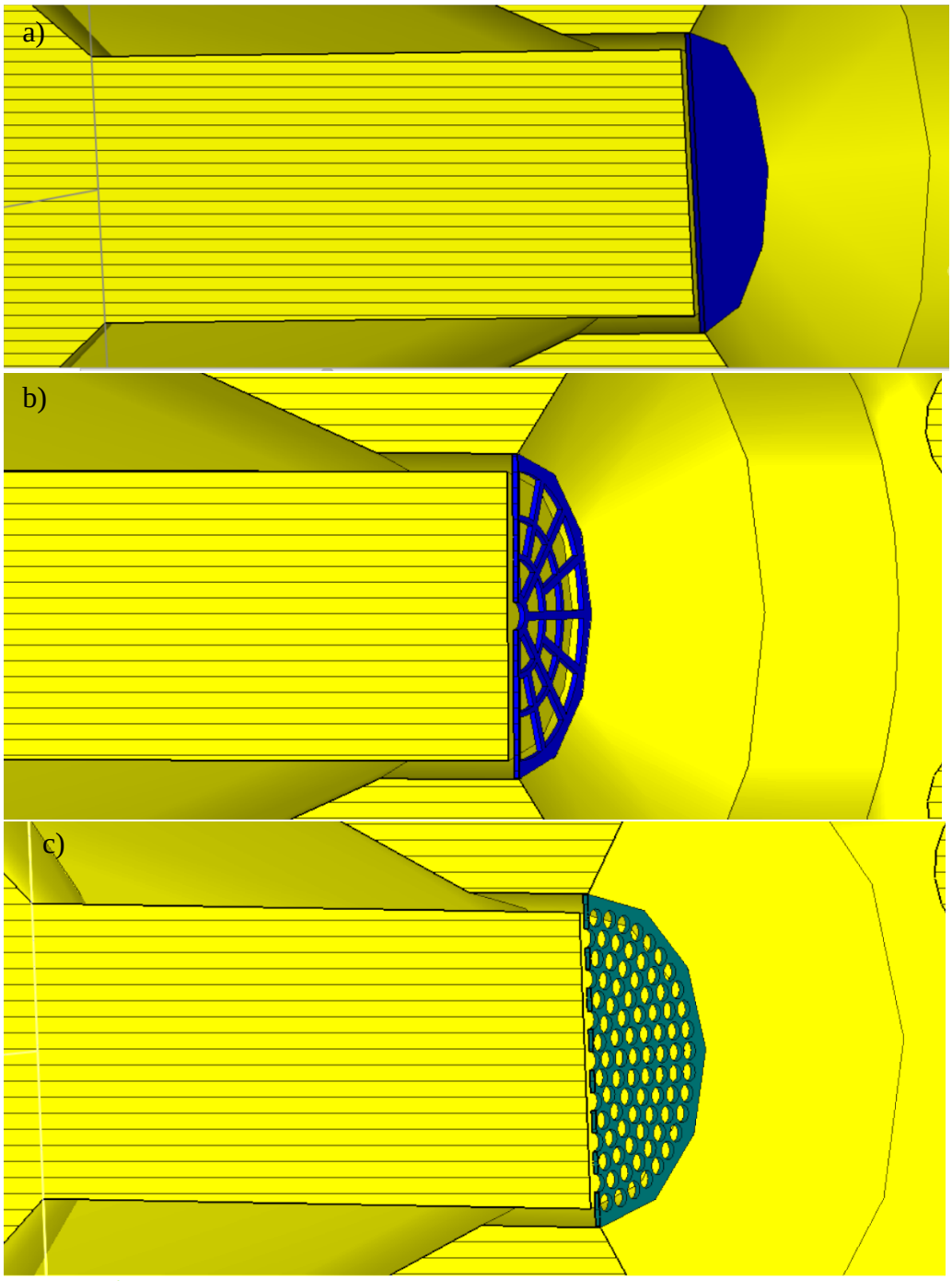

Figure 6-16. Three types of grid including a)transparent lossy material b)spider web grid and c) pepperpot grid (top to bottom).

Figure 6-17 illustrates the current pulse which is collected at the exit of the anode for all three types of grids used for modulation. The peak current obtained is much higher almost 63% more for the lossy transparent material while for the spider web grid and the pepper pot grid were quite similar. The primary difference between the types of grid is that the spider web and the pepper pot grid simulation contains radial grid wires. Each radial grid wire appearing in the 3-D geometry partially shields the cathode from the RF fields in the cavity. This shielding effect reduces the electric field at the cathode surface immediately behind the wire and therefore reduces the emitted current density at this location. Note also that the collected current pulse is largest at the head of the bunch, with a rapid rise time followed by slow decay into a low-charge tail. A more numerical comparison is shown in Figure 6-18 and 6-19 where there is a direct comparison for different values of V_{rf} and V_{dc} for the two types of grid. The information obtained by these results concerned the peak current (A), the bunch length (ps) and the bunch charge (pC). Both the spider web and pepper pot grid give quite similar values for both the current and bunch charge.

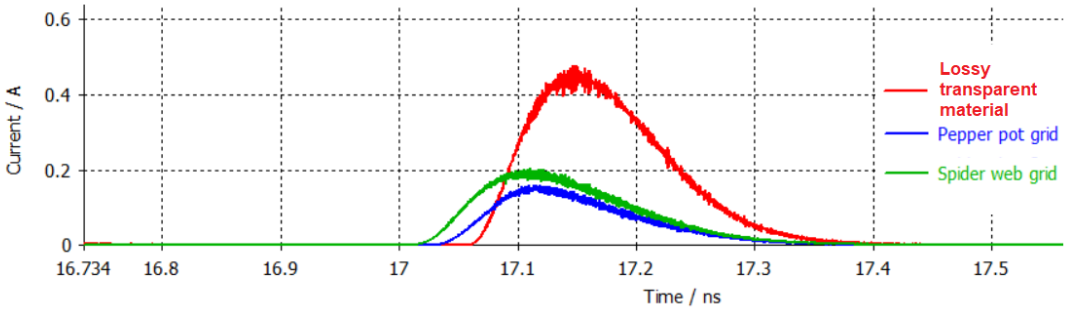

Figure 6-17 Current pulse at the exit of the anode for the the three types of grids.

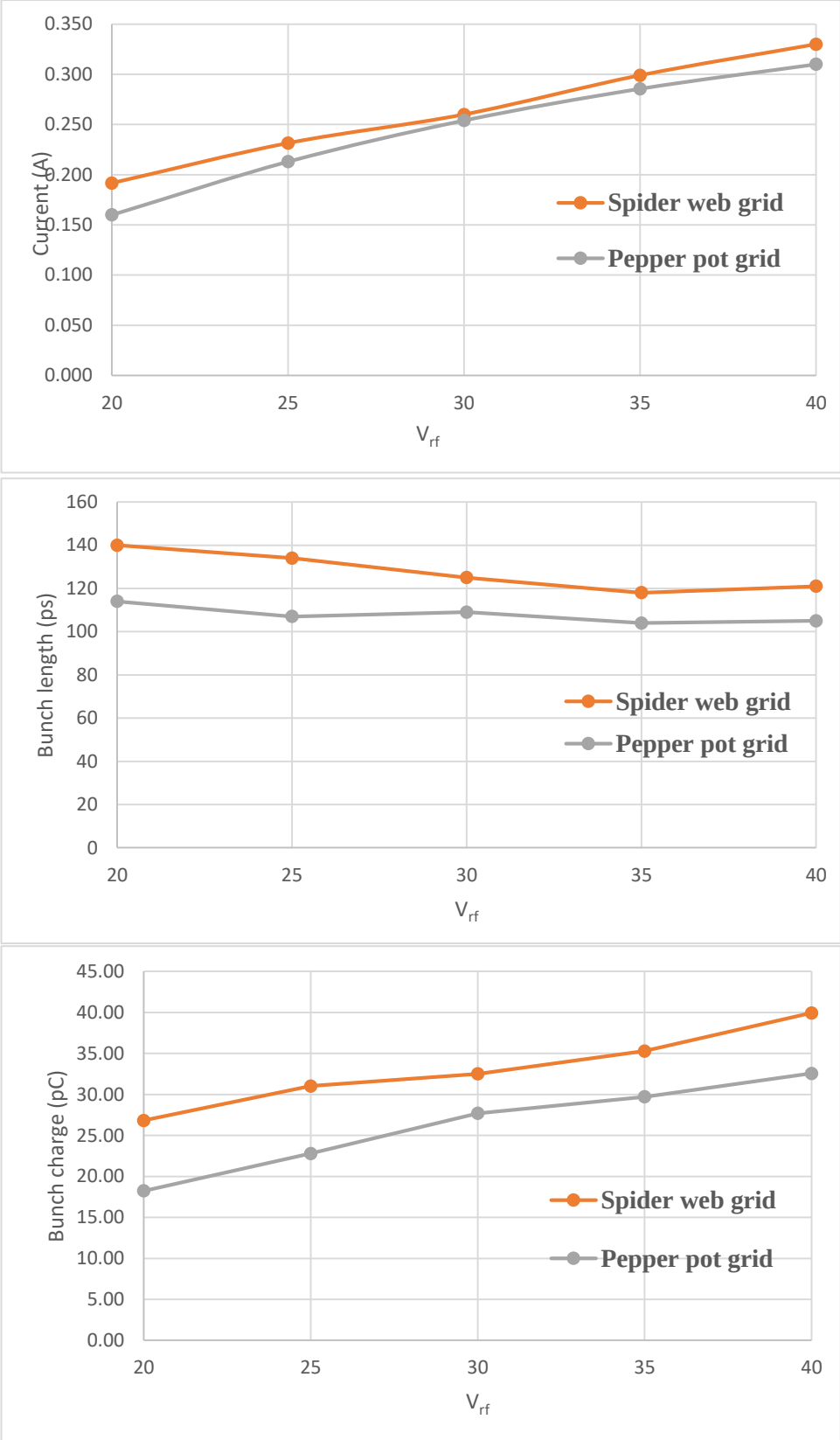

Figure 6-18. Collected current at the exit of the anode, bunch length and bunch charge for different values of V_{rf} and V_{dc}=50V.

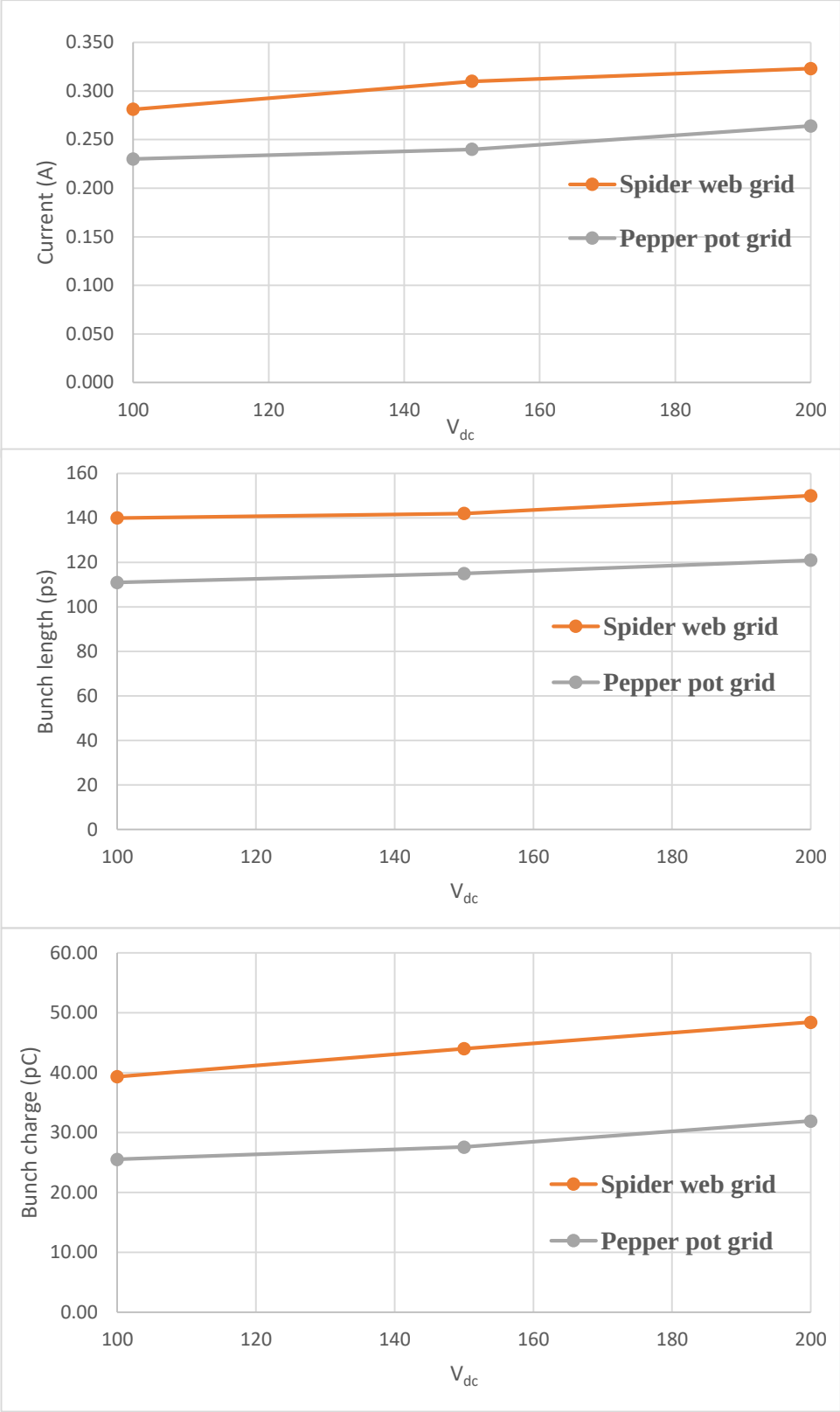

Figure 6-19. Collected current at the exit of the anode, bunch length and bunch charge for different values of V_{dc} and V_{rf}=25V.

6.5 Modulation of the RF-gated grid at higher harmonics of the fundamental frequency.

An RF thermionic electron gun is capable of operating simultaneously at the fundamental frequency and higher frequency harmonics. The main concept of using a higher harmonic frequency is to modify the slope of the RF voltage. According to Fourier series, square waves are mathematically equivalent to the sum of a sine wave at that same frequency while adding a series of odd-multiple frequency sine waves at decreasing amplitude. Basically, a square wave is made from a series of ever-increasing harmonics. The Fourier transform of a sequence of rectangular pulses is a series of sinusoids. The Fourier series is therefore

$$\mathrm{V}(t) = V_0 \sum_{N=1,3,5,\ldots}^{\infty} \frac{1}{N} sin\left(\frac{N\pi t}{T_0}\right) \qquad (6\text{-}8)$$

Figure 6-20 shows a graphical representation of equation 6-8 for an increasing number of harmonics. The second sine wave corresponds to the fundamental one. The third harmonic has an amplitude which is one-third of the fundamental and three times the fundamental frequency showing three periods. Same for the fifth harmonic amplitude which is one-fifth of the fundamental and shows five periods. Addition of the increasing harmonics results in a square wave (top).

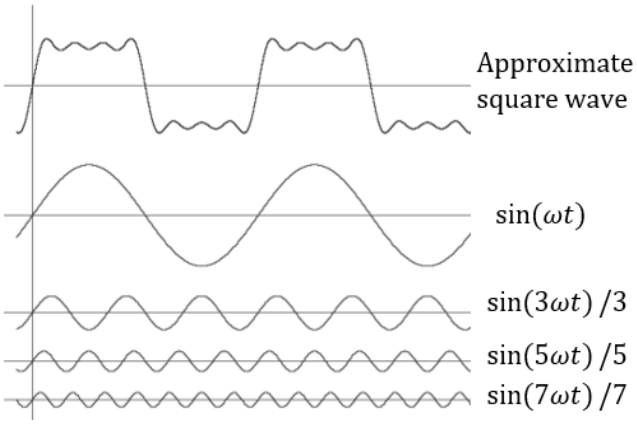

Figure 6-20. Addition of higher harmonics to form a square wave.

The addition of the harmonics is potentially a way of reducing the bunch length by modifying the RF voltage waveform. The effect of adding higher harmonic components to the fundamental could potentially better control the duration of the peak field which expands into a flattop. This may significantly reduce the energy difference of the electrons, which is the main reason for the pulse broadening as seen in the previous section. For example, adding a 3rd harmonic to the fundamental frequency can be written as

$$V_{sum}(t) = V_0 \sin(\omega_1 t + \varphi_1) + V_3 \sin(3\omega_1 t + \varphi_3) \qquad (6\text{-}9)$$

where ω_1 is the angular frequency of the fundamental field, V_3 is the amplitude of the 3rd harmonic field, φ_3 is the phase of the 3rd harmonic fields and t is time. We can choose to set $\varphi_1 = 0$ and we can also write $V_3 = \alpha V_1$ where α is a proportionality constant.

Investigation of the effect of insertion of higher harmonics of the fundamental frequency of the excitation signal to potentially reduce the pulse length was carried out in CST 3D. For this set of simulations, it has to be mentioned that an idealised case

of the insertion of a square wave instead of a series of sinusoidal waves for forming a square wave was implemented. The excitation signal of 1.5GHz (sinusoidal) and the square wave is shown in Figure 6-21. The resulted current pulse for both excitation signals is shown in Figure 6-22. It can be seen with the square excitation signal a higher peak current value thus higher bunch charge could be achieved. The bunch charge and bunch length for the 1.5 GHz excitation signal for this preliminary simulation corresponded to 96pC and 146ps respectively. For the square wave these values were 163pC and 179ps. From this result it can be seen that a longer bunch length was obtained but the bunch charge was much higher for this case. Based on these results it was decided to further investigate the effect of the duration of the excitation signal on the minimum possible bunch length.

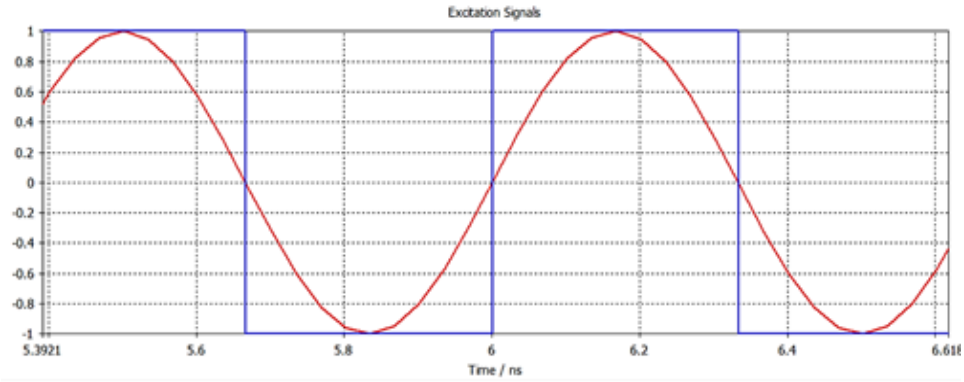

Figure 6-21. Excitation signal of 1.5GHz and square excitation signal.

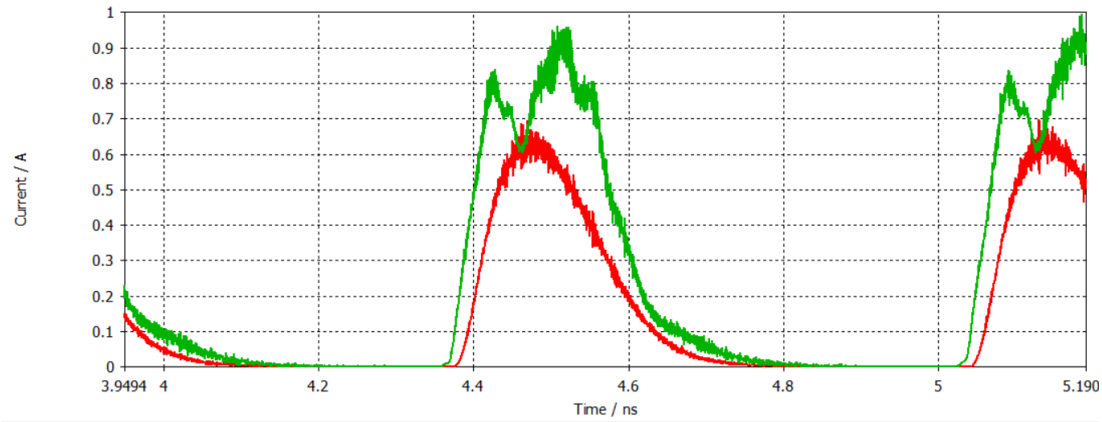

Figure 6-22. Collected currents for 1.5GHz sinusoidal excitation signal (red) and for a square excitation signal (green).

The different duration square pulses were obtained using MATLAB and the function of CST which allows a user input signal was used. The different duration signals are shown in Figure 6-23. The values of the bunch charge and bunch length achieved are shown in Figure 6-24. The minimum possible bunch length value obtained was 87ps corresponding to 94pC bunch charge for the 0.22ns excitation signal. Comparing the result obtained for the 1.5 GHz excitation signal to the 0.22ns square excitation signal, the bunch charge was almost the same for both signals however the square signal resulted into a much shorter pulse of 87ps compared to 146ps implying higher harmonics could potentially be a way for reducing the bunch length. Further simulation work could be carried out as future work to investigate the effect of adding a phase to the excitation signal to the peak current and the bunch length/charge.

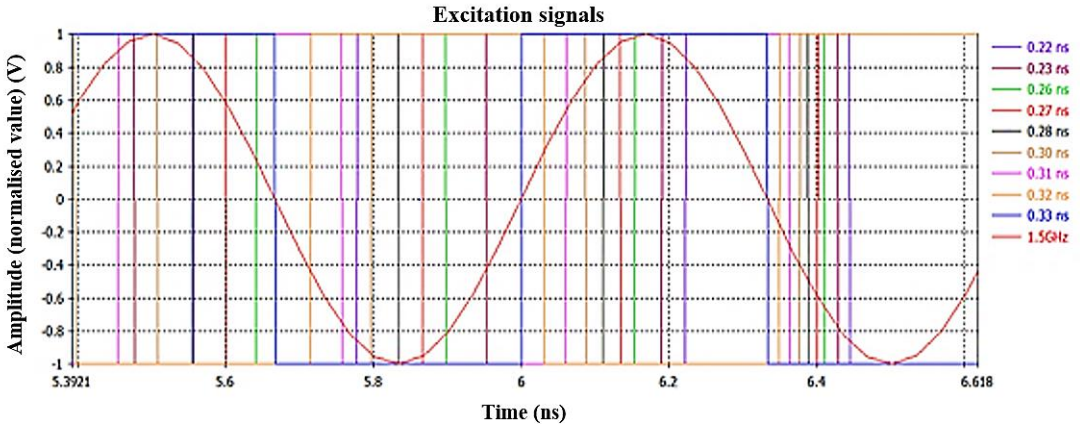

Figure 6-23. User input excitation signals for the different time duration.

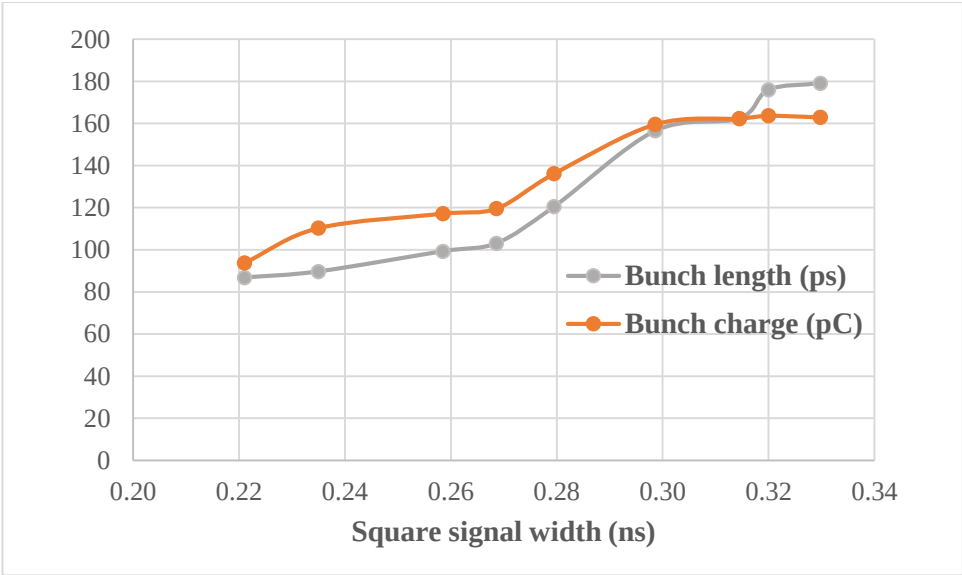

Figure 6-24. Bunch length and bunch charge values for different signal widths.

Summary

In this chapter, the performance of the electron gun was examined using 3D CST Particle Studio. Initially, the static electron gun was simulated using the Particle Tracking solver and the values were directly compared with the results obtained with TRAK. Results were broadly in agreement with slightly lower values for the current for our 3D simulations. Following the verification of the results in 2D and 3D, the RF electron gun was examined using the CST Particle Studio PIC simulations. Two different voltages V_{rf} and V_{dc} were used for this set of simulations and the effect of each on the bunch dynamics was analysed. The values of the bunch length for 34 pC bunch charge corresponded to 102 ps which is in agreement with 2D MAGIC results. Furthermore, different types of grid design were modelled and their effect on the gun's performance was examined. Lastly, the effect of the idealised case of a square excitation signal via the the use of harmonic signals on the 1.5GHz fundamental frequency RF grid voltage showed that a fuller higher current 0.87A electron beam pulse was obtained as compared to 0.6A when no additional harmonic signals were used.

Chapter 7

7 Conclusions

This chapter summarises the main conclusions of this thesis and the future work based on the current findings.

7.1 Summary

Medical LINACs and high average power FELs require short duration and high peak current electron bunches. These requirements place strict constraints on the electron gun. The investigation that was undertaken for this thesis was the design and the modelling of a thermionic gridded electron gun. The development of this electron gun was an important basis for the design of more efficient thermionic electron guns able to achieve short, high current electron bunches for particle accelerator applications.

The design of the electron gun was carried out in three steps which involved a theoretical model, simulation of both the static and the RF electron gun in 2D and validation of the results with 2D MAGIC and 3D CST Particle Studio simulations. The computational results for using MAGIC 2D and 3D CST Particle studio have been benchmarked against each other for similar parameter sets.

Initially in chapter 3, the development of a theoretical model for the gridded thermionic electron gun based on the initial electron beam parameters of the LINAC was carried out. From this theoretical model the waveform of the control voltage and the emitted current was obtained along with other important parameters like bunch charge, bunch length. One of the main aims from this model was to establish the minimum bunch length for the required value of the 33pC bunch charge (LINAC requirement) which was found to be 68ps for 1.5GHz modulation. Higher values of modulating frequency (3GHz) was investigated to examine the effect on the bunch length. Operating at this higher frequency of 3GHz showed that the minimum bunch length had a lower value of 23ps.

Theoretical model	Bunch charge (pC)	Bunch length (FWHM) (ps)
1.5GHz	33	68
3GHz	16.7	23

Table 7-1. Theoretical prediction of bunch charge and bunch length with respect to frequency of the RF applied to the grid.

Having some estimated values for the above parameters, the design and the simulation of the static electron gun using a Finite Element Method code, TRAK was shown in Chapter 4. Firstly, the electron gun was designed based on Vaughan synthesis and was further optimised for better beam laminarity using the TRAK code where parameters like the cathode radius, the cathode-anode gap distance and the focusing electrode angle were investigated. Furhemore, the emittance which is another crucial parameter for a LINAC was measured to be 1.0 mm·mrad at the exit of the anode. This value corresponded to the transeverse emittance which is given by $\varepsilon_{x,RMS} = \sqrt{\langle x^2 \rangle \langle x'^2 \rangle - \langle xx' \rangle^2}$ while the normalised emittance $\varepsilon_{norm} = \beta\gamma\varepsilon_{x,RMS}$ corresponded to 0.33 mm·mrad. This developed and optimised static electron gun design was used as a basis to introduce an RF signal in our design. This time a FDTD code, MAGIC, was used to simulate the RF electron gun. The effect of the combination of the RF and a bias voltage on the emitted current and the relationship between the bunch length and bunch charge was examined while a comparison of these values with the theoretical values was made. The minimum pulse length of 106 ps could be achieved with a bunch charge of 33.3 pC when the driving RF frequency was 1.5 GHz. Higher values of bunch length were obtained compared to the ones in the theoretical model. Further simulation work showed the main reason for the discrepancy between these values was the electron velocity differences due to different grid voltages as a function of time. This effect resulted in the head of the bunch having larger energy compared to the tail when driven by the RF field contributing to almost most of the widening of the pulse compared to the theoretical values. The value for the normalised emittance at the exit of the anode for the static, DC electron gun was 0.3 mm·mrad which is a much smaller value compared to the PIC simulation result. The reason for

this discrepancy is assigned to the weak acceleration field due to the RF voltage applied between the cathode and grid, as well as the uneven space charge force on the bunch resulting in higher emittance for the RF gun compared to the DC gun. Furthermore, operating at higher frequency (3GHz) didn't show much effect on the bunch length compared to the theoretical model.

PIC Simulations	Bunch charge (pC)	Bunch length (FWHM) (ps)
1.5GHz	33	106
3GHz	16.7	100

Table 7-2. Prediction of PiC imulations of bunch charge anad bunch length with respect to frequency of the RF applied to the grid.

The reason for the PIC simulations having a longer bunch length than predicted by theory was due to the energy difference of the electrons passing through the grid leading to different travel time of the electrons which was not taken into account in theory alone. This was the major contribution to the lengthening of the electron beam pulse and to a lesser extent the space charge effect at the head and tail of the electrons in the bunch.

7.2 Comparison of 2D MAGIC and 3D PIC simulations of the RF gated e-gun

The average transverse emittance predicted by MAGIC 2D was about 17 mm·mrad calculated by statistically counting the electrons at the exit of the anode which resulted in an average normalised emittance for the RF gun was about 5.6 mm·mrad which is much higher than the static electron gun. To build further confidence, the performance of the electron gun was examined using 3D CST Particle Studio. The RF electron gun was examined using the PIC code for two different voltages Vrf and Vdc in this set of

simulations with the effect of each on the bunch dynamics analysed. The values of the bunch length for 34 pC bunch charge corresponded to 102 ps was obtained from 3D CST PS which is in agreement with 2D MAGIC results. Moreover, different designs of grids, the spider web grid and the pepperpot grid were modelled and their effect on the performance of the electron gun studied. Both sets of simulations showed that there is not much difference in the parameters in terms of current and bunch charge when using the two different grids indicating that either option could be used for the modulation of the RF electron gun.

7.3 Conclusion

The minimum pulse length of 106 ps could be achieved with a bunch charge of 33.3 pC when the driving RF frequency was 1.5 GHz. The average transverse emittance was about 17 mm·mrad calculated by statistically counting the electrons at the exit of the anode. The major part of the bunch had a normalised emittance of less than 5.6 mm·mrad.

Increasing the driven RF frequency helps to reduce the pulse length of the emitted current. However, the improvement to the collected current was not significant. The velocity spread due to the different grid voltages as the function of the time is the main reason for the widening of the pulse from the emitted current to the collected current at the entrance of the acceleration cavity. It is not dependent on the driving RF frequency and is mainly determined by the grid distance and thickness of the grid structure.

Lastly, the effect of higher harmonics and in this case the idealised case of a square imported signal showed that the smallest bunch length possible corresponded to 87 ps

which is smaller than the 106ps bunch length obtained with the 1.5GHz excitation signal without the addition of harmoinics. This could be potentially a way of achieving smaller bunch length while keeping the bunch charge the same although further simulation work is needed to examine the effect of the phase of the excitation signal on the bunch length/charge.

Considering all the benefits of a thermionic cathode such as large current densities of 1-50 A/cm^2, long lifetimes (100,000 hours for 1A/cm^2 current density), cost-effective (£30,000) for entire gridded thermionic cathode electron gun and ability to deliver a high power electron beam along with the results of this extensive research we concluded that this thermionc gun is a good candidate for medical LINACs and Infrared FELs.

7.4 Future work

The results presented, demonstrate a promising electron gun for particle accelerator applications for achieving short, high current pulses. The level of confidence in the simulation models used in this thesis is high as three simulation programs, TRAK, MAGIC and 3D CST Particle Studio, were used for acquisition and comparison of the results. The first step of this work involved the optimisation of the electron gun obtained using the Vaughan synthesis where one parameter at a time was changed observing its effect on the beam dynamics. One consideration for the future work is the variation of more than one parameter at a time. Once this work is carried out, the next proposed work would the fabrication of the electron gun for comparing and ideally validating the simulations with the experimental work.

The first step for the experimental work would involve construction and assembly of the electron gun according to our optimised geometry for minimum bunch length and minimum normalised and transverse emittance at 1.5GHz. The experimental set could also investigate the use of higher harmonics of the RF frequency so the RF drive for the cathode-grid circuit needs to be produced by a multifrequency amplifier to accommodate the frequency used for the fundamental frequency of 1.5GHz and any higher harmonics. Furthermore, to examine apart from the higher harmonics the effect of the phase (another parameter which could be examined as future work of simulations), a phase shifter could be used to allow control of the relative phase between the fundamental and higher harmonic signals. Once this set up is complete, the RF gridded thermionic cathode electron gun can be in operation with both the cathode to anode voltage and the grid voltage adjusted to obtain optimum performance in terms of buch charge, pulse length and emmittance. The electron bunches generated from the gun can be collected by a fast Faraday cup. To take into account any bunch spreading due to space charge spreading and velocity spreading the Faraday cup needs to be placed as close as possible to the electron gun's output. The current collected by the Faraday cup can through calibrated attenuators and be recorded by a digital oscilloscope where the amplitude and length of the pulses can be examined when different experimental variables like the Vgrid and higher harmonic RF drive.

Another critical parameter for the bunches produced by the electron gun is their emittance. In this case, one of the ways to measure the beam emittance is by employing a slit-base measurement [61, 119, 120]. This measurement involves a horizontal tantalum slit which is scanned across the beam and the electrons passing through the slit are intercepted in most cases by a yttrium aluminum garnet (YAG) screen. In turn,

the fluorescent screen is imaged and recorded using a digital CCD camera controlled by an appropriate software.

References

1. Seeman J, Schulte D, jean-pierre D, Ross M, Stapnes S, Grudiev A, et al. Design and Principles of Linear Accelerators and Colliders. 2020. p. 295-336.

2. Boucher S, Kutsaev S, Murokh A. The Future Trends in Electron Linacs for Industrial and Medical Applications. APS Journal. 2020.

3. Kutsaev S, Agustsson R, Arodzero A, Boucher S, Murokh A, Smirnov A. Sub-MeV ultra-compact linac for radioactive isotope sources replacement, non-destructive testing, security and medical applications. Nuclear Instruments and Methods in Physics Research Section B Beam Interactions with Materials and Atoms. 2019;459.

4. Kutsaev S, Agustsson R, Arodzero A, Boucher S, Smirnov A. Electron Accelerators for Novel Cargo Inspection Methods. Physics Procedia. 2017;90:115-25.

5. Treutwein M, Härtl P, Gröger C, Katsilieri Z, Dobler B. Linac Twins in Radiotherapy. 2015. p. 171-86.

6. Karzmark CJ, Pering NC. Electron linear accelerators for radiation therapy: history, principles and contemporary developments. Physics in Medicine and Biology. 1973;18(3):321-54.

7. Lagendijk J, Raaymakers B, Vulpen M. The Magnetic Resonance Imaging-Linac System. Seminars in radiation oncology. 2014;24:207-9.

8. Starovoitova VN, Tchelidze L, Wells DP. Production of medical radioisotopes with linear accelerators. Applied Radiation and Isotopes. 2014;85:39-44.

9. Zhuikov BL. Production of medical radionuclides in Russia: Status and future—a review. Applied Radiation and Isotopes. 2014;84:48-56.

10. Anggraita P. Linacs for Medical Isotope Production. Atom Indonesia. 2011;37.

11. Kanaji T, Yasuda K, Ikuta S, Takeda M. Pulsed X-Ray Radiography with Electron Linear Accelerator (I) Precise Control of Electron Linear Accelerator. Japanese Journal of Applied Physics. 1968;7(2):102-11.

12. PodgorŠAk EB, Rawlinson JA, GlavinoviĆ MI, Johns HE. Design of X-ray Targets for High Energy Linear Accelerators in Radiotherapy. American Journal of Roentgenology. 1974;121(4):873-82.

13. Çeçen Y, Gülümser T, Yazgan Ç, Djapo H, Üstün M, Boztosun I. Photoneutron Flux Measurement via Neutron Activation Analysis in a Radiotherapy Bunker with an 18 MV Linear Accelerator. EPJ Web of Conferences. 2017;153:07006.

14. Yücel H, Çobanbaş İ, Kolbaşı A, Yüksel AÖ, Kaya V. Measurement of Photo-Neutron Dose from an 18-MV Medical Linac Using a Foil Activation Method in View of Radiation Protection of Patients. Nuclear Engineering and Technology. 2016;48(2):525-32.

15. Israngkul-Na-Ayuthaya I, Suriyapee S, Pengvanich P. Evaluation of equivalent dose from neutrons and activation products from a 15-MV X-ray LINAC. J Radiat Res. 2015;56(6):919-26.

16. Zolfaghari M, Masoudi SF, Rahmani F. Optimization of Linac-based neutron source for thermal neutron activation analysis. Journal of Radioanalytical and Nuclear Chemistry. 2018;317(3):1477-83.

17. O'Shea P, Freund H. Free-Electron Lasers: Status and Applications. Science (New York, NY). 2001;292:1853-8.

18. Zen H, Suphakul S, Kii T, Masuda K, Ohgaki H. Present Status and Perspectives of Long Wavelength Free Electron Lasers at Kyoto University. Physics Procedia. 2016;84:47-53.

19. Duris J, Musumeci P, Babzien M, Fedurin M, Kusche K, Li RK, et al. High-quality electron beams from a helical inverse free-electron laser accelerator. Nature Communications. 2014;5(1):4928.

20. Rivera N, Roques-Carmes C, Kaminer I, Soljačić M, editors. Toward Nanophotonic Free-Electron Lasers. Conference on Lasers and Electro-Optics; 2020 2020/05/10; Washington, DC: Optical Society of America.

21. Inoue I, Osaka T, Hara T, Yabashi M. Two-color X-ray free-electron laser consisting of broadband and narrowband beams. Journal of Synchrotron Radiation. 2020;27(6):1720-4.

22. Sharma A, Tripathi VK. A plasma filled gyrotron-pumped free-electron laser. Physics of Plasmas. 1996;3(8):3116-20.

23. Cheng RKY, Abela R, Hennig M. X-ray free electron laser: opportunities for drug discovery. Essays in Biochemistry. 2017;61(5):529-42.

24. Hamm RW. Commercial applications of linacs. United States; 1991. Contract No.: LA--12004-C.

25. Zhu TC, Wang KKH. Linear Accelerators (LINAC). In: Brady LW, Yaeger TE, editors. Encyclopedia of Radiation Oncology. Berlin, Heidelberg: Springer Berlin Heidelberg; 2013. p. 437-50.

26. European XFEL in international comparison [Available from: https://www.xfel.eu/facility/comparison/index_eng.html.

27. Able C, Hampton C, Baydush A, Munley M. Initial investigation using statistical process control for quality control of accelerator beam steering. Radiation oncology (London, England). 2011;6:180.

28. Hanna S. Role of Linear Accelerators in Water Treatment. 2021.

29. Poursaleh A. Design and Simulation of High Power RF Modulated Triode Electron Gun. Life Science Journal. 2013;10:2685-9.

30. Gaudreau D, Casey J, Mulvaney J, Kempkes M, Smith P, Cloude S. Compact, Solid-State Pulse Modulators for High Power Microwave Applications. 2002. p. 485-91.

31. Andreev D, Kuskov A, Schamiloglu E. Review of the relativistic magnetron. Matter and Radiation at Extremes. 2019;4(6):067201.

32. Jones D. Understanding Microwave Treatment of Ores. 2005.

33. Carter R. Radio-frequency power generation. CERN Accelerator School: High Power Hadron Machines, CAS 2011 - Proceedings. 2013.

34. Xia P. The Modern Technology of Radiation Oncology, Volume 3: A Compendium for Medical Physicists and Radiation Oncologists. Medical Physics. 2014;41(12):127301.

35. Zubizarreta EH, Fidarova E, Healy B, Rosenblatt E. Need for Radiotherapy in Low and Middle Income Countries – The Silent Crisis Continues. Clinical Oncology. 2015;27(2):107-14.

36. Sridhar T, Symonds P. Principles of chemotherapy and radiotherapy. Obstetrics, Gynaecology & Reproductive Medicine. 2006;16:61-7.

37. Portaluri M, Fucilli F, Castagna R, Bambace S, Pili G, Tramacere F, et al. Three-dimensional conformal radiotherapy for locally advanced (Stage II and worse) head-and-neck cancer: Dosimetric and clinical evaluation. International journal of radiation oncology, biology, physics. 2006;66:1036-43.

38. Prior P, Sparks I, Wilson J, Bovi J, Currey A, Bradley J, et al. Use of Three Dimensional Conformal Radiation Therapy for Node Positive Breast Cancer Does Not Result in Excess Lung and Heart Irradiation. International Journal of Medical Physics, Clinical Engineering and Radiation Oncology. 2017;6:1.

39. Purdy JA, Michalski JM, Bradley J, Vijayakumar S, Perez CA, Levitt SH. Three-Dimensional Treatment Planning and Conformal Therapy. In: Perez CA, Vijayakumar S, Levitt SH, Purdy JA, editors. Technical Basis of Radiation Therapy: Practical Clinical Applications. Berlin, Heidelberg: Springer Berlin Heidelberg; 2006. p. 179-202.

40. Taylor A, Powell M. Intensity-modulated radiotherapy - What is it? Cancer imaging : the official publication of the International Cancer Imaging Society. 2004;4:68-73.

41. Cheung K. Intensity modulated radiotherapy: Advantages, limitations and future developments. Biomedical imaging and intervention journal. 2006;2:e19.

42. Li G, Mageras S, Dong L, Mohan R. Image-Guided Radiation Therapy IntroductIon. 2012. p. 229-58.

43. Goyal S. Image Guided Radiation Therapy. Journal of Nuclear Medicine & Radiation Therapy. 2014;05.

44. Jaffray DA. Image-guided radiotherapy: from current concept to future perspectives. Nat Rev Clin Oncol. 2012;9(12):688-99.

45. van Herk M. Different Styles of Image-Guided Radiotherapy. Seminars in Radiation Oncology. 2007;17(4):258-67.

46. Ahmed M. Basic Concepts of Laser. 2009.

47. McNeil BWJ, Thompson NR. X-ray free-electron lasers. Nature Photonics. 2010;4(12):814-21.

48. Dohlus M, Dohlus J, Schmüser P. Low-Gain FEL Theory. 2009;258.

49. He A, Yang L, Yu L. High-Gain FEL Theory, Introduction. In: Jaeschke E, Khan S, Schneider JR, Hastings JB, editors. Synchrotron Light Sources and Free-Electron Lasers: Accelerator Physics, Instrumentation and Science Applications. Cham: Springer International Publishing; 2021. p. 1-37.

50. Nguyen DC, Freund HP. Possibility of a high-power, high-gain FEL amplifier. Nuclear Instruments and Methods in Physics Research Section A: Accelerators, Spectrometers, Detectors and Associated Equipment. 2003;507(1):120-4.

51. Pelka J, Tybor KR, Nietubyć R, Wrochna G. Applications of Free Electron Lasers in Biology and Medicine. Acta Physica Polonica A. 2010;1178553.

52. Yun K, Kim S, Kim D, Chung M, Jo W, Hwang H, et al. Coherence and pulse duration characterization of the PAL-XFEL in the hard X-ray regime. Scientific Reports. 2019;9(1):3300.

53. Neutze R, Brändén G, Schertler GFX. Membrane protein structural biology using X-ray free electron lasers. Current Opinion in Structural Biology. 2015;33:115-25.

54. Molitoris J, Lee R, Kalantar D. Warm Dense Matter: An Overview2004.

55. Chapman H, Caleman C, Timneanu N. Diffraction before destruction. Philosophical transactions of the Royal Society of London Series B, Biological sciences. 2014;369.

56. Pellegrini C. Free Electron Lasers: Development And Applications. 1990;33.

57. St. Aubin J, Steciw S, Kirkby C, Fallone BG. An integrated 6 MV linear accelerator model from electron gun to dose in a water tank. Medical Physics. 2010;37(5):2279-88.

58. Torgasin K, Mishima K, Zen H, Yoshida K, Negm H, Omer M, et al. Properties of quarter-wavelength coaxial cavity for triode-type thermionic RF gun. Japanese Journal of Applied Physics. 2017;56:096701.

59. Togawa K, Shintake T, Inagaki T, Onoe K, Tanaka T, Baba H, et al. CeB6 electron gun for low-emittance injector. Physical Review Special Topics-accelerators and Beams - PHYS REV SPEC TOP-AC. 2007;10.

60. Sprangle P, Penano JR, Hafizi B, Gordon D, Gold S, Ting A, et al. High Average Current Electron Guns for High-Power FELs. Physical Review Special Topics Accelerators and Beams. 2009;14:43.

61. Gold S, Ting A, Jabotinski V, Zhou B, Sprangle P. Development of a high average current rf linac thermionic injector. Physical Review Special Topics - Accelerators and Beams. 2013;16.

62. Whelan B, Holloway L, Constantin D, Oborn B, Bazalova-Carter M, Fahrig R, et al. Performance of a clinical gridded electron gun in magnetic fields: Implications for MRI-linac therapy. Medical Physics. 2016;43(11):5903-14.

63. Opanasenko A, Mytrochenko V, Zhaunerchyk V, Goryashko V. Design study of a low-emittance high-repetition rate thermionic rf gun. Physical Review Accelerators and Beams. 2017;20.

64. Asaka T, Ego H, Hanaki H, Hara T, Hasegawa T, Inagaki T, et al. Low-emittance thermionic-gun-based injector for a compact free-electron laser. Physical Review Accelerators and Beams. 2017;20.

65. El-Saftawy A, Elfalaky A, Ragheb M, Zakhary S. Numerical Simulation of Beam Formation and Transport in an Electron Gun for Different Applications. Journal of Nuclear and Particle Physics. 2012;2:126-31.

66. Zhang L, Adam G, Militsyn B, He W, Cross AW. Electron Injector Based on Thermionic RF-Modulated Electron Gun for Particle Accelerator Applications. IEEE Transactions on Electron Devices. 2020;67(1):347-53.

67. Mitchell C, Sprangle P, Penano JR. A Gridded Thermionic Injector Gun for High-Average-Power Free-Electron Lasers. IEEE Transactions on Plasma Science. 2012;40:1977-83.

68. Hosseinzadeh M, Sadighzadeh A. Design and numerical simulation of thermionic electron gun. Chinese Physics C. 2015;40.

69. Bakr M, Ohgaki H. Influence of the Cathode Material Properties in Reducing the Back-Bombardment Effect in Thermionic RF Gun. IEEE Transactions on Electron Devices. 2018;65(11):5053-61.

70. Dowell DH, Davis KJ, Friddell KD, Tyson EL, Lancaster CA, Milliman L, et al. First operation of a photocathode radio frequency gun injector at high duty factor. Applied Physics Letters. 1993;63(15):2035-7.

71. Arnold A, Büttig H, Janssen D, Kamps T, Klemz G, Lehmann W, et al. A high-brightness SRF photoelectron injector for FEL light sources. Nuclear Instruments and Methods in Physics Research Section A: Accelerators, Spectrometers, Detectors and Associated Equipment. 2008;593:57-62.

72. Arnold A, Teichert J. Overview on superconducting photoinjectors. Physical Review Special Topics - Accelerators and Beams. 2011;14(2):024801.

73. Huang R, Mitchell C, Papadopoulos C, Qian H, Venturini M, Qiang J, et al. Off-axis beam dynamics in rf-gun-based electron photoinjectors. Physical Review Accelerators and Beams. 2016;19.

74. Wang XJ, Qiu X, Ben-Zvi II. Experimental observation of high-brightness microbunching in a photocathode rf electron gun. Phys Rev E Stat Phys Plasmas Fluids Relat Interdiscip Topics. 1996;54(4):R3121-r4.

75. Muggli P, Yakimenko V, Babzien M, Kallos E, Kusche K. Generation of Trains of Electron Microbunches with Adjustable Subpicosecond Spacing. Physical review letters. 2008;101:054801.

76. Spindt CA, Brodie I, Humphrey L, Westerberg ER. Physical properties of thin-film field emission cathodes with molybdenum cones. Journal of Applied Physics. 1976;47(12):5248-63.

77. Caruso GM, Houdellier F, Abeilhou P, Arbouet A. Development of an ultrafast electron source based on a cold-field emission gun for ultrafast coherent TEM. Applied Physics Letters. 2017;111:023101.

78. Tand C-M, Ting A, Swyden T. Field-emission arrays - a potentially bright source. Nuclear Instruments & Methods in Physics Research Section A-accelerators Spectrometers Detectors and Associated Equipment - NUCL INSTRUM METH PHYS RES A. 1992;318:353-7.

79. Li X, Li M, Dan L, Liu Y, Tang C. Cold cathode rf guns based study on field emission. Physical Review Special Topics Accelerators and Beams. 2013;16:123401.

80. Bormashov VS, Baturin AS, Nikolskiy KN, Tchesov RG, Sheshin EP. The current stability of field emission cathodes of carbon nanotubes under ion bombardment. Surface and Interface Analysis. 2007;39(2-3):155-8.

81. Redhead PA. The birth of electronics: Thermionic emission and vacuum. Journal of Vacuum Science & Technology A. 1998;16(3):1394-401.

82. Dai X, Kong Y, Li J, Liu B. Extended Finnis–Sinclair potential for bcc and fcc metals and alloys. Journal of Physics: Condensed Matter. 2006;18:4527.

83. Luginsland JW, Lau YY, Umstattd RJ, Watrous JJ. Beyond the Child–Langmuir law: A review of recent results on multidimensional space-charge-limited flow. Physics of Plasmas. 2002;9(5):2371-6.

84. Zhang T. Synchrotron Radiation Studies of Molecular Building Blocks for Functional Materials 2018.

85. Krüger M, Lemell C, Wachter G, Burgdoerfer J, Hommelhoff P. Attosecond physics phenomena at nanometric tips. Journal of Physics B: Atomic, Molecular and Optical Physics. 2018;51.

86. Zuo JM, Spence JCH. Electron Sources. In: Zuo JM, Spence JCH, editors. Advanced Transmission Electron Microscopy: Imaging and Diffraction in Nanoscience. New York, NY: Springer New York; 2017. p. 193-206.

87. Liu Y, Day CM, Little SA, Jin F. Thin film deposition of barium strontium oxide by rf magnetron sputtering. Journal of Vacuum Science & Technology A. 2006;24(6):2187-91.

88. Yin S, Zhang Z, Peng Z, Zheng Q, Wang Y. A New Impregnated Dispenser Cathode. IEEE Transactions on Electron Devices. 2013;60(12):4258-62.

89. Coletti M, Gabriel S. A Chemical Model for Barium Oxide Depletion from Hollow Cathode's Insert. Collection of Technical Papers - 43rd AIAA/ASME/SAE/ASEE Joint Propulsion Conference. 2007;2.

90. Shukla S, Singh A, Barik R, Ravi M. A Review of Electron Emitters for High-Power and High-Frequency Vacuum Electron Devices. IEEE Transactions on Plasma Science. 2020.

91. Misra PK. Chapter 6 - Static and Transport Properties of Solids. In: Misra PK, editor. Physics of Condensed Matter. Boston: Academic Press; 2012. p. 165-97.

92. Bakr M. Comparison of Heating Property of LaB6 and CeB6 by Back Bombardment Effect in Thermionic RF gun. Journal of Korean Physical Society. 2011;59:3273.

93. Sinclair CK, Adderley P, Dunham B, Hansknecht J, Hartmann P, Poelker M, et al. Development of a high average current polarized electron source with long cathode operational lifetime. Physical Review Special Topics-accelerators and Beams - PHYS REV SPEC TOP-AC. 2007;10.

94. Chen P, Yi R, Yu D, editors. Geometry Optimization of DC/RF Photoelectron Gun. Proceedings of the 2005 Particle Accelerator Conference; 2005 16-20 May 2005.

95. Grudiev A, Calatroni S, Wuensch W. New local field quantity describing the high gradient limit of accelerating structures. Physical Review Special Topics - Accelerators and Beams. 2009;12(10):102001.

96. Jameson RA. RF Breakdown Limits. 1986.

97. Sjøbæk K, Adli E, Grudiev A. New Criterion for Shape Optimization of Normal-Conducting Accelerator Cells for High-Gradient Applications. 2015.

98. Vibrans G. Vacuum Voltage Breakdown as a Thermal Instability of the Emitting Protrusion. Journal of Applied Physics. 1964;35:2855-7.

99. Pande M, Singh P, editors. Study of RF breakdown and multipacting in accelerator components. 2014 International Symposium on Discharges and Electrical Insulation in Vacuum (ISDEIV); 2014 28 Sept.-3 Oct. 2014.

100. Harris J, O'Shea P. Gridded Electron Guns and Modulation of Intense Beams. Electron Devices, IEEE Transactions on. 2006;53:2824-9.

101. Ang LK, Zhang P. Ultrashort-Pulse Child-Langmuir Law in the Quantum and Relativistic Regimes. Physical review letters. 2007;98:164802.

102. Bakker RJ, van der Geer CAJ, van der Meer AFG, van Amersfoort PW, Gillespie WA, Saxon G. 1 GHz modulation of a high-current electron gun. Nuclear Instruments and Methods in Physics Research Section A: Accelerators, Spectrometers, Detectors and Associated Equipment. 1991;307(2):543-52.

103. Vaughan JRM. Synthesis of the Pierce gun. IEEE Transactions on Electron Devices. 1981;28(1):37-41.

104. Chowdhury S. A Progress Report on Generation and Transportation of Terahertz Sheet Electron Beam2019.

105. Livreri P, Badalamenti R, Muratore A. Optimum Design and Performance of an Electron Gun for a Ka-Band TWT. IEEE Transactions on Electron Devices. 2019;PP:1-6.

106. Roel W, Haber T, Lapenta G. Helsim: A Particle-in-cell Simulator for Highly Imbalanced Particle Distributions. Procedia Computer Science. 2015;51:2923-7.

107. Terzić B, Bassi G. New density estimation methods for charged particle beams with applications to microbunching instability. Beams. 2009;12.

108. Yee KS. Numerical solution of initial boundary value problems involving maxwell's equations in isotropic media. IEEE Transactions on Antennas and Propagation. 1966;14:302-7.

109. Taflove A, Brodwin ME. Numerical Solution of Steady-State Electromagnetic Scattering Problems Using the Time-Dependent Maxwell's Equations. IEEE Transactions on Microwave Theory and Techniques. 1975;23(8):623-30.

110. Vandenbosch G, Vasylchenko A. A Practical Guide to 3D Electromagnetic Software Tools. 2011.

111. Sullivan DM. Electromagnetic simulation using the FDTD method: John Wiley & Sons; 2013.

112. Edelvik F, Schuhmann R, Weiland T. A general stability analysis of FIT/FDTD applied to lossy dielectrics and lumped elements. International Journal of Numerical Modelling: Electronic Networks, Devices and Fields. 2004;17:407-19.

113. Clemens M, Weiland T. Discrete electromagnetism with the finite integration technique. Progress In Electromagnetics Research. 2001;32:65-87.

114. Schuhmann R, Weiland T. Conservation of Discrete Energy and Related Laws in the Finite Integration Technique. Progress in Electromagnetics Research-pier - PROG ELECTROMAGN RES. 2001;32:301-16.

115. Weiland T. Time domain electromagnetic field computation with finite difference methods. International Journal of Numerical Modelling: Electronic Networks, Devices and Fields. 1996;9(4):295-319.

116. Munteanu I, Weiland T. RF & Microwave Simulation with the Finite Integration Technique – From Component to System Design. 2007. p. 247-60.

117. Weiland T, Timm M, Munteanu I. A practical guide to 3-D simulation. Microwave Magazine, IEEE. 2009;9:62-75.

118. Podebrad O, Clemens M, Weiland T. New flexible subgridding scheme for the finite integration technique. IEEE Transactions on Magnetics. 2003;39(3):1662-5.

119. Togawa K, Shintake T, Baba H, Inagaki T, Onoé K, Tanaka T, et al., editors. Emittance Meausrement on the CeB_6 electron gun for the SPRING-8 Compact SASE Source, 2004.

120. Asaka T, Inagaki T, Magome T, Nishimori N, Otake Y, Taniuchi T, et al. Low-emittance radio-frequency electron gun using a gridded thermionic cathode. Physical Review Accelerators and Beams. 2020;23(6):063401.

121. Radiotherapy Market – Global Industry Analysis, https://www.alliedmarketresearch.com/radiotherapy-market.

122. Free-Electron Laser (FEL) Strategic Review, https://stfc.ukri.org/files/fel-report-2016.

123. Sakaue K, Hayano H, Kashiwagi S, Kuroda R, Masuda A, Suzuki T, et al. Cs–Te photocathode RF electron gun for applied research at the Waseda University. Nuclear Instruments and Methods in Physics Research Section B: Beam Interactions with Materials and Atoms. 2011;269(24):2928-31.

124. Bronsgeest M.S, Physics of Scottky Electron Sources, PhD thesis Technische Universiteit Delft, ISBN:9789085704348 ,2009.

126. Basnet P. Metal Oxide Photocatalytic Nanostructures Fabricated by Dynamic Shadowing Growth, 2015, 10.13140/RG.2.1.2393.8408

127. Fowler RH, Nordheim LW. Electron Emission in Intense Electric Fields. Proceedings of The Royal Society A: Mathematical, Physical and Engineering Sciences.119:173-81.

128. Zuo J.M., Spence J.C.H. (2017) Electron Sources. In: Advanced Transmission Electron Microscopy. Springer, New York, NY. 10.1007/978-1-4939-6607-3_8, 2017

129. Cha J-H, Kim S-W, Lee H-J. A Study on Beam Extraction Characteristics of RF and DC Filament Ion Source for High Current Ion Implanters. Applied Science and Convergence Technology. 2021;30:92-4.

130. Zeng P, Wang G, Wang J, Wang D, Li S. Accurate model of electron beam profiles with emittance effects for pierce guns. Physics of Plasmas. 2016;23(9):093123.

131. Kaushik, Joshi L. RF design of input cavity structure of a low frequency, high average power, conference paper, IOT 2015.

132. Gilmour A.S, Microwave Tubes, Artech House Publishers, ISBN13: 9780890061817, 1986, chapter 6.

133. Gilmour A.S, Microwave Tubes, Artech House Publishers, ISBN13: 9780890061817, 1986, chapter 5.

134. Andrew Burnett, Marco Borghesi, Andrew Comley, Mark Dean, Sofia Diaz-Moreno, David Dye, Jason Greenwood, Andrew Higginbotham, Adam Kirrander, Jon Marangos, Malcolm McMahon, Russell Minns, Marcus Newton, Allen Orville, Thomas Penfold, Anna Regoutz, Ian Robinson, David Rugg, Sven Schroeder, Jasper van Thor, Sam Vinko, Simon Wall, Justin Wark, Julia Weinstein, Amelle Zair and Xiaodong Zhang, “UK XFEL Science Case”, STFC Sponsor, John Collier, Editor, Jon Marangos, 2020

Electron injector based on thermionic RF modulated electron gun for particle accelerator applications

Liang Zhang, *Senior Member, IEEE*, Georgia Adam, Boris Militsyn, Wenlong He and Adrian W. Cross

Abstract—**In this paper, the design and simulation of an electron injector based on a thermionic RF modulated electron gun for particle accelerator applications is presented. The electron gun is based on a gridded thermionic cathode with the geometry based on a Pierce-type configuration. Both theory and numerical simulation were used to explore the relationship between the bunch length and charge. The reasons for the pulse widening were also analyzed. The beam dynamics simulations showed that a minimum pulse length of 106 ps could be achieved with a bunch charge of 33 pC when the driving RF frequency was 1.5 GHz. The average transverse emittance was about 17 mm·mrad from the particle-in-cell simulations. Operating at a higher RF frequency did not significantly reduce the micro-pulse length.**

***Index Terms*— RF gun, thermionic electron gun, particle accelerators.**

I. Introduction

Electron beam sources in radio-frequency (RF) electron guns which generate high peak current and low emittance electron beams in a particle accelerator are core to the operation of coherent radiation sources such as Free-electron lasers (FELs) [1] and medical linacs [2]. There are three main types of RF electron guns used as injectors, including thermionic cathodes [3], photocathodes [4], and field emission cathodes [5]. In thermionic RF guns, the cathode is heated and electrons are continuously emitted and accelerated during the half RF period. This results in a long electron beam pulse and a wide energy spread at the exit of the linac. The problem of energy spread and pulse duration control is solved by using photocathode RF guns, where a laser pulse is used to extract the electrons from the cathode material. Short laser pulses generate short electron bunches with higher current densities. However, the performance of photocathodes is limited by the availability of the high power laser. Another type of RF gun is based on field emission which uses a needle-shaped cathode placed in a high electric field but it is fragile and prone to damage by vaporization of the cathode tip when generating high current density electron pulses.

The photocathode can generate the ideal electron bunch for the accelerator. It has the advantages of large current density, short pulse and low intrinsic emittance to match every acceleration RF bucket, and high quality producing low emittance electron beams [4, 6-9]. However, there are challenges involved in operating photocathodes such as in-vacuum photocathode replacement systems to improve lifetime, requirements of ultra-high vacuum, as well as use of a high power drive laser which limits its applications to particle accelerators that require the very lowest emittance beams.

As a comparison, the thermionic cathode can produce high average power electron beams and has the advantages of a long lifetime, proven in many vacuum electronic devices which have operating lifetimes of longer than 100,000 hours. The thermionic cathode is also cost-effective and can produce large current densities of 10-100 A/cm^2 with increased lifetime achieved the lower the current density due to a more modest emitter operating temperature [10]. A thermionic RF gun is compact in structure and is relatively simple to operate. It also can be operated at high repetition rates.

Normally a diode or triode type thermionic electron gun is used. In a diode-type cathode, the high voltage is applied between the cathode and the anode to produce a CW electron beam. The electrons that fill the acceleration RF bucket are accelerated. The electrons outside the acceleration RF bucket will either strike the acceleration cavity's wall or back bombard on the cathode surface. It can cause significant thermal issues and shorten the cathode's lifetime as well as producing stray X-ray radiation.

The object of this paper is to investigate the modulation of the electron beam, produced by the thermionic cathode, to significantly improve the efficiency of electron beam acceleration. The diode-type cathode can be gated by switching on/off the high voltage power supply. However, its repetition rate is very low. A triode-type cathode which has an additional electrode between the cathode and anode can achieve a much higher repetition rate since the required drive voltage is much lower. It can be driven by an RF voltage to gate the electron

L. Zhang (liang.zhang@strath.ac.uk), G. Adam (georgia.adam@strath.ac.uk) and A. W. Cross (a.w.cross@strath.ac.uk) are with Department of Physics, SUPA, University of Strathclyde, Glasgow, G4 0NG, Scotland, UK and the Cockcroft Institute, Warrington Bank Quay. UK. B. Militsyn (boris.militsyn @stfc.ac.uk) is with the Cockcroft Institute, Sci-Tech Daresbury, and the ASTeC, STFC Daresbury Laboratory, Sci-Tech Daresbury, Keckwick Lane, Daresbury, Cheshire, WA4 4AD, United Kingdom. W. He (wenlong.he@szu.edu.cn) is with College of Electronic Science and Technology, Shenzhen University, Shenzhen, 518060, China. This work is under the support of Science and Technology Facilities Council (STFC) U.K. research grant, ST/S002081/1. Georgia Adam would like to thank STFC, UK and TMD Technologies Ltd for providing the industrial Accelerators for Security Health and the Environment (ASHE) PhD case studentship.

beam and has attracted a great deal of interest as an electron beam source in RF linacs [11-14] as the electron micro-pulses can be matched with the acceleration RF buckets as well as achieving control of the emitted electron beam.

The charge, length and emittance of the generated electron bunch are important parameters for the thermionic RF modulated gun used in linacs. In this paper, their relation was obtained from a simplified theoretical model and further studied by particle-in-cell simulation through the design of an RF gun for a linac [15]. Section II discusses the configuration of the RF gun as well as the RF cavity. The theoretical model of the RF gun and the relationship between the bunch charge and bunch length is presented in section III. Section IV describes the design process of an RF electron gun. The performance, including the relationship between the bunch charge and bunch length and the reasons for the widening of the bunch length is discussed in section V.

II. Configurations of the RF Gun

The configuration of the electron gun with RF gating is shown in Fig. 1. The emitted electron beam is modulated by the RF voltage, applied between the cathode and the grid. The RF gun in Fig. 1(a) is placed at the entrance of the RF acceleration cells, and the electron beam will be directly accelerated by the electric field in the cells [3, 11, 13, 14]. It has the advantage that the cathode structure is simple. However, since the cathode is also a part of the RF acceleration circuit, it is difficult to be demounted because it may change the cavity parameters, and it is hard to avoid RF heating of the grid. The configuration in Fig. 1(b) contains an additional DC acceleration section. It enables pre-acceleration of the electron beam and focusing of the emitted electrons to achieve a smaller radius and divergence since an optimal focusing electrode can be used [16]. Another advantage is the design of the cathode and the acceleration cells can be decoupled. The RF gun can be demountable to save the cost of replacing the whole linac as well as reducing maintenance. The electron gun in the linac requires long lifetime, low cost and needs to be easily maintained on a limited budget, hence a demountable capability can be very attractive. Therefore, the configuration in Fig. 1(b) is studied in this paper.

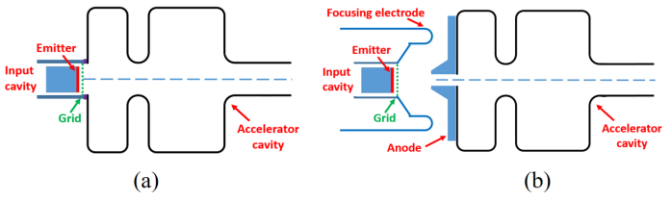

Fig. 1. The configuration of the RF gun, (a) without DC pre-acceleration, (b) with DC pre-acceleration.

The initial electron beam parameters of the proposed linac are listed in Table 1. The study was to design a thermionic cathode RF gated gun to meet the required beam parameters, and also to investigate the properties of the electron bunch, including the bunch charge, bunch length and emittance.

Table 1 the specifications of the linac

Beam energy	6 MeV
Acceleration frequency	3 GHz
Repetition rate	300 Hz
RF pulse length	7.5 us
RF gated frequency (GHz)	1.5 or 3.0
Bunch charge Q (pc)	33.3 @ 1.5 GHz 16.7 @ 3.0 GHz
Bunch length τ (ps)	As short as possible
Peak current (A)	Q/τ
Pre-acceleration voltage (kV)	25
Beam radius (mm)	<2.5

III. A Theoretical Model of the Bunch Length

The RF voltage can be driven through a capacitively-loaded coaxial cavity. Its basic geometry is shown in Fig. 2(a) and its eigenfrequency ω_0 can be estimated with

$$\frac{1}{Z_0}\cot(\beta L) - \omega_0 C = 0 \qquad (1)$$

where Z_0 is the impedance, β is the wavenumber, and the capacitance of the cavity $C = C_1 + C_2 = \frac{\varepsilon\pi a^2}{d} + 4\varepsilon a \ln\frac{b-a}{d}$. The eigenfrequency is more sensitive to the cavity length L, therefore it can be used for fine-tuning after the other dimensions are determined.

A practical structure of the input cavity for the RF electron gun is shown in Fig. 2(b) [17]. The parameters a, b and d are determined by the electron gun geometry. Its eigenfrequency can be tuned by the cavity length. Fig. 2(b) also shows its electric field pattern calculated using the 3D EM simulation software CST Microwave Studio at a resonance frequency of 1.5 GHz. In the simulation, the grid structure is simplified as a perfect electrical conductor (PEC) since the sizes of the grids are much smaller than the wavelength of the operating mode.

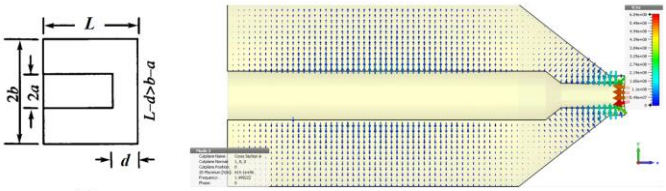

Fig. 2. The schematic of a coaxial input cavity (a) and the electric field pattern from the eigenmode simulation (b).

The thermionic electron gun can operate in the space charge limited or temperature limited regimes. The space charge limited current density follows the Child Langmuir law [18], which is determined by the field strength at the emitter surface, while the current density at the temperature limited regime follows with Richardson's law and it is mainly determined by the temperature at the emitter surface [19]. To be RF gated, the electron gun in the linac should operate at the space charge limited regime to totally switch off the electron beam. Also operating at lower temperatures and smaller current density, an electron gun with a long lifetime and low emittance is possible. The current density in the space charge limited emission regime applied with a static electric field is given by

$$J = \frac{I}{S} = \frac{4\varepsilon_0}{9}\sqrt{\frac{2e}{m}}\frac{U_{grid}^{3/2}}{d^2} \quad (U_{grid} > 0) \qquad (2)$$

where U_{grid} is the total voltage across the cathode and the grid, d is their distance, and S is the area of the cathode. When driven by a RF voltage U_{rf}, the emitted current will also be modulated with the same frequency. However, when the frequency of RF voltage is high, and the pulse length of the electron beam is less than the transit time from the emitter to the grid, the classic Child Langmuir law will no longer be valid. The current density for a short current pulse can be obtained by applying a correction factor to the steady-state value of the classic Child Langmuir law, which is given by [20]

$$J_{short} = 2\frac{1-\sqrt{1-3X_{CL}^2/4}}{X_{CL}^3}J \quad (3)$$

where $X_{CL} = \tau/T_{CL} \leq 1$ is the normalized transit time and $T_{CL} = 3d/\sqrt{2eU_{grid}/m}$ is the transit time from the emitter to the grid. For the thermionic RF gated gun studied in this paper, the transit time is ~ 60 ps, and it is smaller than the pulse duration (~100 ps). The classic Child Langmuir law is still valid.

Eq. 2 indicates that the current emits from the cathode at half of the RF cycle when $U_{grid} > 0$. To control the emission time, a negative bias voltage U_{bias} can be applied to stop the emission of the electrons, and the total grid voltage becomes

$$U_{grid} = U_{rf}\cos(2\pi ft - \theta) + U_{bias} \quad (4)$$

Fig. 3 shows the typical waveforms of the control voltage and the emitted current. In the linac, the required electron beam current is relatively small and the beam energy is low. A large beam aperture can be used and results in a small current density. In this case, a linear approximation of the emitted current in Eq. 5 can be used. G_{emit} is the emission coefficient which is in the range of 10 – 30 mA/V for practical cathodes. U_{cutoff} describes the cutoff voltage which can be obtained from previously published results [21].

$$I = G_{emit}(U_{grid} - U_{cutoff}) \quad (5)$$

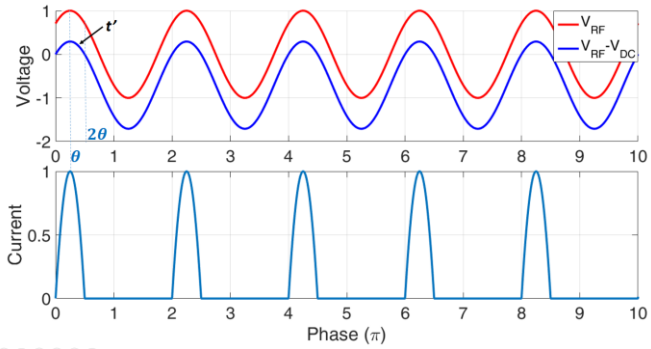

Fig. 3 The driving voltage and the emitted current

The bunch charge, bunch length and emittance are important parameters of the RF gun in the linac. The bunch charge can be integrated from the emitted current and is

$$Q = \int I(t)dt = \frac{U_{rf}}{f}\frac{2G_{emit}}{2\pi}(\sin\theta - \theta cos\theta) \quad (6)$$

where $cos\theta = (-U_{bias} + U_{cutoff})/U_{rf}$ denotes when the electrons are allowed to be emitted. The bunch length of the emitted current is determined by the phase θ with τ=$\theta/2\pi f$.

The electrons will travel to the grid under the applied electric field. To simplify the calculation, the space charge effect is ignored and the electric field between the emitter and the grid is regarded as a uniform distribution, as shown in Fig. 2. The electron's longitudinal position follows Eq. 7.

$$\ddot{L}(t) = \frac{e}{m}\frac{U_{grid}}{d} \quad (7)$$

The electrons may experience both accelerating and decelerating electric fields. Only the electrons emitted before time t' is able to pass through the grid and escape the cathode-grid region to the anode. Otherwise they will be reflected back to the emitter by the decelerating electric field. The time t' determines the bunch duration from the emitter, which is defined by Eq. 8.

$$L(2\tau) - L(t') = d \quad (8)$$

It is preferred to have t′ close to 2τ to reduce the beam current lost, since the backstreaming electrons will reduce the lifetime of the cathode. In this case, the gap distance d should be as small as possible. However, it has a physical constraint of about 0.16 mm. The gap length also sets a limit to the voltage between the cathode and the grid, which is $U_{rf} + |U_{bias}|$, due to the vacuum breakdown.

The theoretical model provides the emission process of the electron beam, as well as the relationship between the electron bunch length, bunch charge, and the applied RF and bias voltages. The bottom threshold of the emitted bunch length for a given bunch charge can be obtained by solving the Eq. 4-8. Fig. 4 shows the results at 1.5 GHz and 3.0 GHz, respectively. In the calculation, the gap distance of 0.16 mm was used. A reasonable emission coefficient G_{emit} of 18 mA/V, and the limit of $U_{rf} + |U_{bias}|$ = 600V was chosen. With a bunch charge of 33.3 pC at 1.5 GHz, the bunch length is about 68 ps when $\theta = 40°$. With a bunch charge of 16.7 pC at 3.0 GHz, the bunch length is about 23 ps when $\theta = 45°$. For this idealised case operating at higher frequency helps to reduce the emitted bunch length.

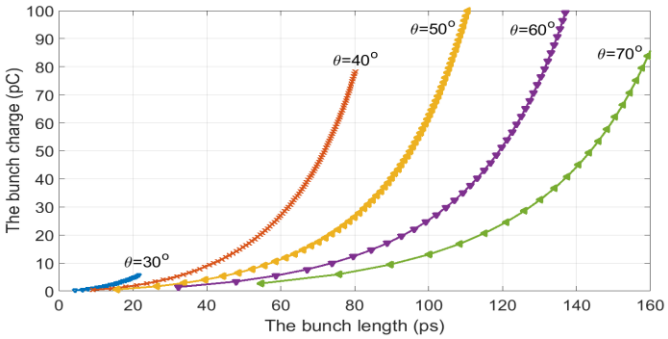

(a)

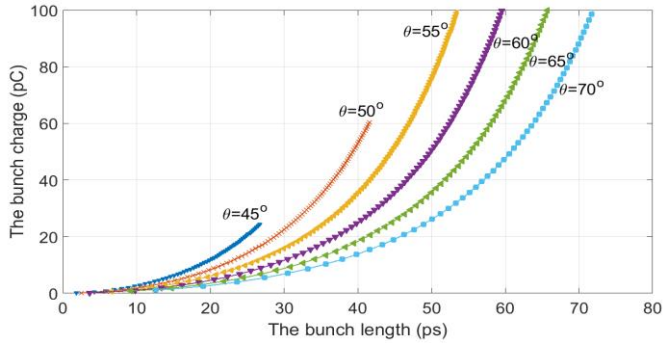

(b)

Fig. 4. The relation between bunch length and bunch charge at different operating frequencies, (a) 1.5 GHz, and (b) 3.0 GHz.

IV. Design of the Electron Gun Geometry

The theoretical analysis does not include the effects such as the space charge, thermal emission distribution and the beam dynamics between the grid and anode. In this section, a practical electron gun is designed. The performance was investigated through numerical particle-in-cell simulations.

The design of the RF gun is based on the Pierce-type configuration which is commonly used in the conventional vacuum electronic devices, such as traveling wave tubes, klystrons and inductive output tubes (IOTs) [22]. The initial geometry was generated based on the Vaughan synthesis [23] with 4 input parameters, including the beam voltage, beam current, emitter radius as well as the beam waist, as listed in Table 1. The initial geometry was then used as the starting point for further optimization to get more accurate simulation results and to further improve the electron beam quality, including good laminarity and a small emittance. Ideally, the finite-difference-time-domain method and particle-in-cell (FDTD-PIC) simulation which is able to simulate the beam dynamics when driven by RF field is required. However, it is time-consuming as a fine mesh has to be used to represent the thin grid structure. In the optimization, it was more practical to use 2D DC-voltage gun design code EGUN to simulate the electron beam trajectory since only 5% of the simulation time was required. The optimal geometry was then applied with the grid structure to investigate further beam dynamics with the RF driving field using the FDTD-PIC code MAGIC.

The Pierce-type gun is normally with a curved emitter surface to achieve a large beam compression ratio, however, it is not a critical parameter of the required RF gun since a large beam radius is acceptable. The emitter surface was therefore simplified by using a readily available, cost-effective, commercial gridded cathode. The model chosen was the NJK2221A gridded thermionic cathode from Japan Radio Co. Ltd. It has a flat emission surface with a radius of 4.0 mm, and a grid distance of 0.16 mm. The flat emitter surface also helped to save the simulation time since a less dense mesh grid could be used to represent a flat surface as compared to a curved cathode surface.

The beam trajectories of the optimized geometry simulated by EGUN are shown in Fig. 5(a). The acceleration voltage between the cathode and anode was 25 kV and the emitted current was 1.0 A. The radius of the beam waist was ~1.5 mm. The beam trajectories ware exported for post-processing the emittance. The root mean square (RMS) normalized transverse beam emittance defined by $\varepsilon_{\mathrm{rms}} = \sqrt{\langle x^2\rangle\langle x'^2\rangle - \langle xx'\rangle^2}$ at the exit of the anode was 1.0 mm·mrad, where x and x' were the position and angle of the electrons in x coordinate [24]. Its geometry was then simulated with MAGIC. The complete configuration including the input cavity described in section II together with the grid structure is shown in Fig. 5(b). When the gun is only driven by the DC acceleration voltage without the RF voltage, the simulation results are the same as EGUN. When driven by an RF voltage and a bias voltage, the electron bunch was generated. Fig. 6 shows the spatial distribution of electrons at different time frames, corresponding to the process of bunch emission from the emitter, bunch acceleration by the electric field and at the exit of the anode.

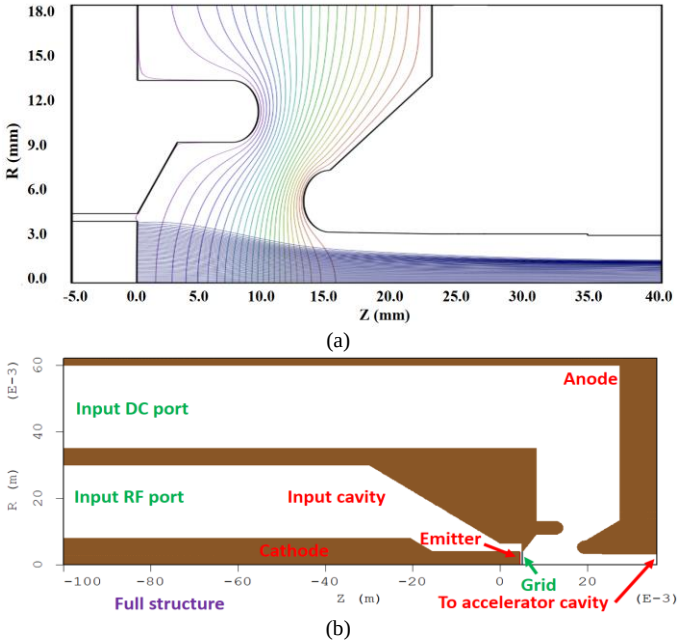

Fig. 5 The optimized geometry of the gun from EGUN (a) and the model of the RF gun including the input coupler used in simulations with MAGIC (b).

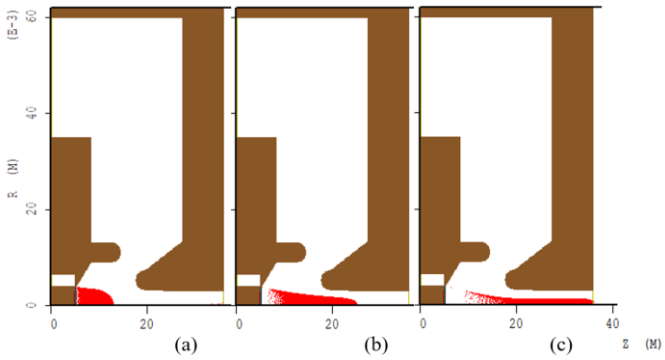

Fig. 6 The spatial distribution of electrons at different simulation time frames, (a) bunch emitted from the emitter, (b) bunch acceleration by the electric field, (c) bunch at the exit of the anode.

V. Performance of the RF Gun

The performance of the RF gun was studied by applying different combinations of the RF and bias voltages. The simulated results of the peak emitted current as a function of the applied voltage are shown in Fig. 7. At different DC bias voltages, the curves are close to each other at the same total voltages $U_{grid} = U_{rf} + U_{bias}$. The results show good linearity of the emitted current over a wide range of the grid voltages, which validates the approximation of Eq. 4. The value of G_{emit} from the linear fit was about 18 mA/V.

Fig. 8 shows the emitted current from the cathode and the collected current at the entrance of the acceleration cavity at $U_{rf} = 170\,\mathrm{V}$ and $U_{bias} = -115\,\mathrm{V}$. The waveform of the emitted current matched well with the theoretical prediction. The amplitude of the collected current pulse waveform of the emitted current was about 40% of the emitted current. The charge in the individual collected and emitted current pulse was

calculated by integrating the current and they were found to be 72 pC and 43 pC, respectively. The ratio between them was about 60%, which indicated that 40% of the electrons emitted from the cathode backstreamed to the emitter surface due to the deceleration voltage. The PIC simulation shows a much larger value than the theoretical prediction.

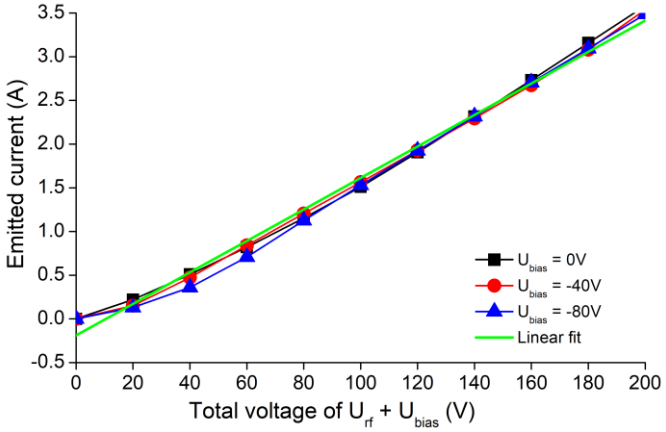

Fig. 7 The relationship between the grid voltage and the emitted current.

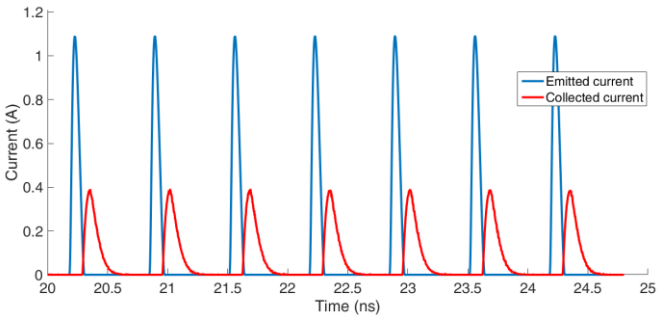

Fig. 8 The emitted current from the cathode and the collected current at the entrance of the accelerator cavity.

The Full-width-half-maximum (FWHM) lengths of the emitted and collected bunches were 72 ps and 107 ps respectively from the simulation. It is much larger than the theoretical prediction. The theoretical model did not include the effect of space charge at the emitter, thermal emission distribution and the beam dynamics between the grid and anode. Further simulations were carried out to identify and quantify these factors which resulted in the widening of the bunch. they include:

(1) Velocity differences due to the different grid voltages as a function of the time. The head of the bunch had larger energy and the tail had less energy when driven by the RF field. Considering electrons accelerated by grid voltages 30 V and 10 V, the time difference was 81 ps with a traveling distance of 0.36 mm (the grid distance plus the grid thickness) in the PIC simulation which takes into account the space charge at the emitter. It is the major reason for the widening of the pulse.

(2) Different path lengths of the electrons. The electrons emitted from different positions traveled with different paths. The electrons emitted from larger emitter radius travel longer distances. The difference in the traveling time from the EGUN simulation was 28 ps.

(3) The space charge force accelerates the head of the bunch and decelerates the tail of the bunch. EGUN simulations show there was about 16 ps additional contribution to the pulse length due to space charge effects. The space charge force would have less impact when operating at a smaller beam current.

The sliced transverse emittance was also calculated by statistically counting the electrons at the exit of the anode. Fig. 9 shows the correlated emittance and the current of the electron bunch as the function of the simulation time. The emittance was lower at the head of the bunch and it increased as a function of the bunch charge. The major part of the bunch had an emittance of less than 17 mm·mrad. The tail of the bunch has larger emittance however the current contained in this part of the bunch was small. The noise of the emittance at the end of the bunch was due to the unstable statistical variation due to the small number of electrons. The PIC simulation showed a much bigger emittance compared to the static electric field case. The relatively weak acceleration field due to the RF voltage applied between the cathode and grid, as well as the uneven space charge force on the bunch were the main reasons for the high emittance of the RF gated gun.

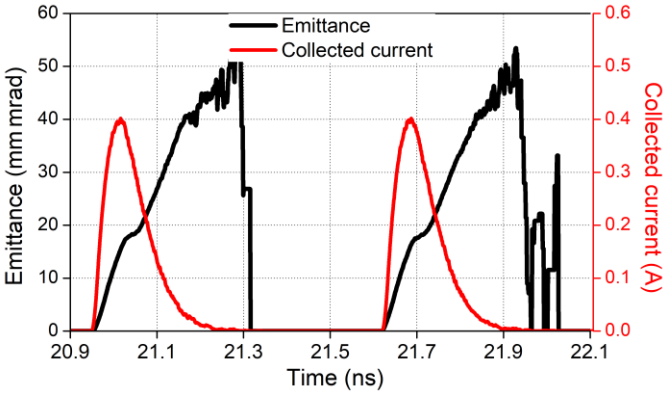

Fig. 9 The emittance of the electron at the exit of the anode.

By varying the RF and bias voltage, the bunch length and bunch charge of the collected current change accordingly. Fig. 10(a) shows the simulation results at different combinations of U_{rf} and U_{bias} at a driven frequency of 1.5 GHz. When fixing U_{bias} while increasing U_{rf} both larger bunch charge and longer bunch length were observed. However, the growing of the bunch charge as a function of bunch length follows a linear trend, which was different from the theoretical prediction shown in Fig. 4. The theoretical model showed that smaller θ (equivalently larger U_{bias} value) helps to reduce the bunch length. The PIC simulations also show the same trend. However, its impact on the bunch length was very small. By increasing the bias voltage from -80 V to -170 V, the difference in the bunch length was about 5 ps only at the same bunch charge. The minimum bunch length of 106 ps could be achieved with a bunch charge of 33.3 pC.

The average transverse emittances at different RF and bias voltages were also studied. When fixing U_{bias} while increasing U_{rf}, a higher grid voltage can be achieved and it helped to reduce the transverse emittance. A minimum transverse emittance of 12 mm·mrad could be achieved. At different bias voltages, the trend of transverse emittance was similar. Since the DC acceleration region was also a main source of the

emittance, it is possible to improve the emittance by further optimizing the geometry of the cathode and anode.

Fig. 4 shows that the length of the emitted pulse can be reduced by operating at the higher RF frequency. The PIC simulation proved the trend, however, it was found that more electrons were backstreamed to the emitter when operating at a higher frequency. The bunch length and bunch charge at different grid voltages with RF frequency of 3.0 GHz are shown in Fig. 10(b). The minimum bunch length of 100 ps could be achieved with a bunch charge of 16.7 pC, which means the bunch length at the entrance of the linac was reduced slightly at a higher frequency. Since the first two reasons for the pulse widening were mainly determined by the electron gun structure. In this case no significant advantage was to be gained by operating at higher RF frequency as this does not reduce the pulse width or shortens the bunch length. When operating at a higher frequency, the emitted current had to have larger compensation due to the higher ratio of the backstreaming electrons. The space charge force, therefore, became larger and resulted in longer pulse widening. It also results in larger emittance.

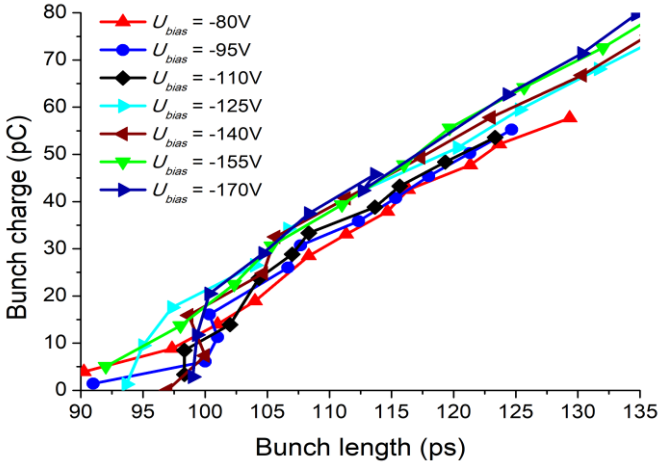

(a)

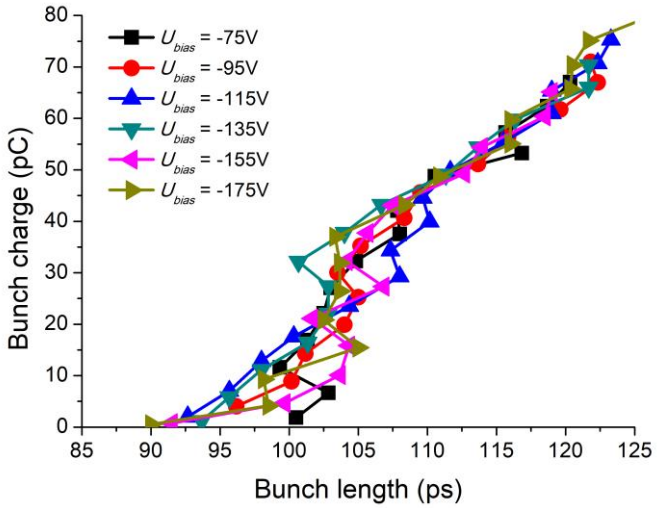

(b)

Fig. 10 The relationship between the bunch length and bunch charge at different grid voltages with RF frequency of (a) 1.5 GHz and (b) 3.0 GHz.

VI. Conclusion

In this paper, a thermionic RF gun for particle accelerator applications was investigated. The electron gun was based on a commercially available gridded cathode and the geometry was optimized based on the Pierce-type configuration. A theoretical model was used to predict the relationship between the bunch length and charge. However, it is limited by ignoring the effect of space charge at the emitter and the beam dynamics between the grid and anode. The performance of the electron gun was further studied by PIC simulations. The reasons for the pulse widening have been analyzed.

The minimum pulse length of 106 ps could be achieved with a bunch charge of 33.3 pC when the driving RF frequency was 1.5 GHz. The average transverse emittance was about 17 mm·mrad. Increasing the driven RF frequency helps to reduce the pulse length of the emitted current. However, the improvement to the collected current was not significant. The velocity spread due to the different grid voltages as the function of the time is the main reason for the widening of the pulse from the emitted current to the collected current at the entrance of the acceleration cavity. It is not dependent on the driving RF frequency and is mainly determined by the grid distance and thickness of the grid structure.

Compared with the photocathode injection gun, the emittance of the proposed RF gun is much larger, which limits its applications in linacs that can operate with electron pulses of a certain brightness. However, by combining the merits of compact, demountable, and long lifetime, applications can be found in medical and industry linacs where the ultimate brightness is not required.

References

[1] Z. Huang and K.-J. Kim, "Review of x-ray free-electron laser theory," *Physical Review Special Topics - Accelerators and Beams*, vol. 10, no. 3, p. 034801, March 2007. DOI: 10.1103/PhysRevSTAB.10.034801

[2] J. St. Aubin, S. Steciw, C. Kirkby, and B. G. Fallone, "An integrated 6 MV linear accelerator model from electron gun to dose in a water tank," *Med. Phys.*, vol. 37, no. 5, pp. 2279-2288, 2010. DOI: 10.1118/1.3397455

[3] C. Mitchell, P. Sprangle, and J. Peñano, "A Gridded Thermionic Injector Gun for High-Average-Power Free-Electron Lasers," *IEEE Trans. Plasma Sci.*, vol. 40, no. 8, pp. 1977-1983, 2012. DOI: 10.1109/TPS.2012.2201962

[4] D. H. Dowell, K. J. Davis, K. D. Friddell, E. L. Tyson, C. A. Lancaster, L. Milliman, R. E. Rodenburg, T. Aas, M. Bemes, S. Z. Bethel, P. E. Johnson, K. Murphy, C. Whelen, G. E. Busch, and D. K. Remelius, "First operation of a photocathode radio frequency gun injector at high duty factor," *Appl. Phys. Lett.*, vol. 63, no. 15, pp. 2035-2037, 1993/10/11 1993. DOI: 10.1063/1.110583

[5] C.-M. Tang, A. C. Ting, and T. Swyden, "Field-emission arrays — a potentially bright source," *Nucl. Instrum. Methods. Phys. Res. A*, vol. 318, no. 1, pp. 353-357, 1992/07/01/ 1992. DOI: https://doi.org/10.1016/0168-9002(92)91080-S

[6] X. J. Wang, X. Qiu, and I. Ben-Zvi, "Experimental observation of high-brightness microbunching in a photocathode rf electron gun," *Physical Review E*, vol. 54, no. 4, pp. R3121-R3124, 10/01/ 1996. DOI: 10.1103/PhysRevE.54.R3121

[7] I. V. Bazarov and C. K. Sinclair, "Multivariate optimization of a high brightness dc gun photoinjector," *Physical Review Special Topics - Accelerators and Beams*, vol. 8, no. 3, p. 034202, 03/24/ 2005. DOI: 10.1103/PhysRevSTAB.8.034202

[8] P. Muggli, V. Yakimenko, M. Babzien, E. Kallos, and K. P. Kusche, "Generation of Trains of Electron Microbunches with Adjustable

Subpicosecond Spacing," *Phys. Rev. Lett.*, vol. 101, no. 5, p. 054801, 07/29/ 2008. DOI: 10.1103/PhysRevLett.101.054801

[9] B. Dunham, J. Barley, A. Bartnik, I. Bazarov, L. Cultrera, J. Dobbins, G. Hoffstaetter, B. Johnson, R. Kaplan, S. Karkare, V. Kostroun, Y. Li, M. Liepe, X. Liu, F. Loehl, J. Maxson, P. Quigley, J. Reilly, D. Rice, D. Sabol, E. Smith, K. Smolenski, M. Tigner, V. Vesherevich, D. Widger, and Z. Zhao, "Record high-average current from a high-brightness photoinjector," *Appl. Phys. Lett.*, vol. 102, no. 3, p. 034105, 2013/01/21 2013. DOI: 10.1063/1.4789395

[10] K. Togawa, T. Shintake, T. Inagaki, K. Onoe, T. Tanaka, H. Baba, and H. Matsumoto, "CeB6 electron gun for low-emittance injector," *Physical Review Special Topics - Accelerators and Beams*, vol. 10, no. 2, p. 020703, 02/02/ 2007. DOI: 10.1103/PhysRevSTAB.10.020703

[11] A. Opanasenko, V. Mytrochenko, V. Zhaunerchyk, and V. A. Goryashko, "Design study of a low-emittance high-repetition rate thermionic rf gun," *Physical Review Accelerators and Beams*, vol. 20, no. 5, p. 053401, 05/31/ 2017. DOI: 10.1103/PhysRevAccelBeams.20.053401

[12] S. Suemine, K. Kawase, N. Sugimoto, S. Kashiwagi, K. Furukawa, R. Kato, A. Irizawa, M. Fujimoto, H. Ohsumi, M. Yaguchi, S. Funakoshi, R. Tsutsumi, K. Kubo, A. Tokuchi, and G. Isoyama, "Grid pulser for an electron gun with a thermionic cathode for the high-power operation of a terahertz free-electron laser," *Nucl. Instrum. Methods. Phys. Res. A*, vol. 773, pp. 97-103, 2015/02/11/ 2015. DOI: https://doi.org/10.1016/j.nima.2014.10.071

[13] S. H. Gold, A. Ting, V. Jabotinski, B. Zhou, and P. Sprangle, "Development of a high average current rf linac thermionic injector," *Physical Review Special Topics - Accelerators and Beams*, vol. 16, no. 8, p. 083401, 08/01/ 2013. DOI: 10.1103/PhysRevSTAB.16.083401

[14] P. Sprangle, J. Peñano, B. Hafizi, D. Gordon, S. Gold, A. Ting, and C. Mitchell, "High average current electron guns for high-power free electron lasers," *Physical Review Special Topics - Accelerators and Beams*, vol. 14, no. 2, p. 020702, 02/14/ 2011. DOI: 10.1103/PhysRevSTAB.14.020702

[15] E. H. Zubizarreta, E. Fidarova, B. Healy, and E. Rosenblatt, "Need for Radiotherapy in Low and Middle Income Countries – The Silent Crisis Continues," *Clinical Oncology*, vol. 27, no. 2, pp. 107-114, 2015/02/01/ 2015. DOI: https://doi.org/10.1016/j.clon.2014.10.006

[16] B. Whelan, L. Holloway, D. Constantin, B. Oborn, M. Bazalova-Carter, R. Fahrig, and P. Keall, "Performance of a clinical gridded electron gun in magnetic fields: Implications for MRI-linac therapy," (in eng), *Med. Phys.*, vol. 43, no. 11, pp. 5903-5903, 2016. DOI: 10.1118/1.4963216

[17] K. Torgasin, K. Mishima, H. Zen, K. Yoshida, H. Negm, M. Omer, T. Kii, K. Nagasaki, K. Masuda, and H. Ohgaki, "Properties of quarter-wavelength coaxial cavity for triode-type thermionic RF gun," *Jpn. J. Appl. Phys.*, vol. 56, no. 9, p. 096701, 2017/08/04 2017. DOI: 10.7567/jjap.56.096701

[18] M. Reiser, *Theory and design of charged particle beams*. 1995.

[19] R. Vaughan, "A synthesis of the Longo and Eng cathode emission models," *IEEE Trans. Electron Devices*, vol. 33, no. 11, pp. 1925-1927, 1986. DOI: 10.1109/T-ED.1986.22844

[20] L. K. Ang and P. Zhang, "Ultrashort-Pulse Child-Langmuir Law in the Quantum and Relativistic Regimes," *Phys. Rev. Lett.*, vol. 98, no. 16, p. 164802, 04/19/ 2007. DOI: 10.1103/PhysRevLett.98.164802

[21] R. J. Bakker, C. A. J. van der Geer, A. F. G. van der Meer, P. W. van Amersfoort, W. A. Gillespie, and G. Saxon, "1 GHz modulation of a high-current electron gun," *Nucl. Instrum. Methods. Phys. Res. A*, vol. 307, no. 2, pp. 543-552, 1991/10/01/ 1991. DOI: https://doi.org/10.1016/0168-9002(91)90229-J

[22] A. S. Gilmour, *Klystrons, traveling wave tubes, magnetrons, crossed-field amplifiers, and gyrotrons*. Artech house, 2011.

[23] J. R. M. Vaughan, "Synthesis of the Pierce gun," *IEEE Trans. Electron Devices*, vol. 28, no. 1, pp. 37-41, 1981. DOI: 10.1109/T-ED.1981.20279

[24] K. Floettmann, "Some basic features of the beam emittance," *Physical Review Special Topics - Accelerators and Beams*, vol. 6, no. 3, p. 034202, 03/06/ 2003. DOI: 10.1103/PhysRevSTAB.6.034202